CHALMERS
UNIVERSITY OF TECHNOLOGY

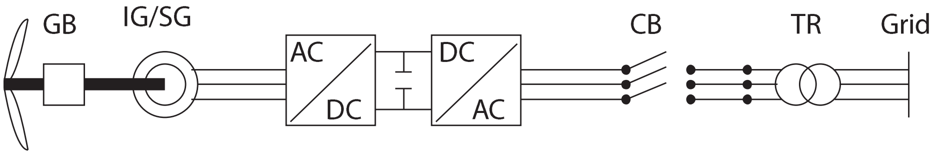


# Utilising Type 4 wind turbines for black start and off-grid operations

*Design of a power synchronisation controller*

Master's thesis in Electric Power Engineering

ARVID BJÖREMARK
ALBIN BJÖRKMAN

DEPARTMENT OF ELECTRICAL ENGINEERING
DIVISION OF ELECTRIC POWER ENGINEERING
CHALMERS UNIVERSITY OF TECHNOLOGY
Gothenburg, Sweden 2020
www.chalmers.se

MASTER'S THESIS 2020

# Utilising Type 4 wind turbines for black start and off-grid operations

Design of a power synchronisation controller

Arvid Björemark
Albin Björkman

Department of Electrical Engineering
*Division of Electric Power Engineering*
CHALMERS UNIVERSITY OF TECHNOLOGY
Gothenburg, Sweden 2020

Utilising Type 4 wind turbines for black start and off-grid operations
Design of a power synchronisation controller



Supervisor: Lucas Thomée, DNV-GL
Examiner: Massimo Bongiorno, Department of Electrical Engineering

Master's Thesis 2020
Department of Electrical Engineering
Division of Electric Power Engineering
Chalmers University of Technology
SE-412 96 Gothenburg
Telephone +46 31 772 1000

Cover: A Type 4 wind turbine visualising the back to back converter.

Typeset in LaTeX
Printed by Chalmers Reproservice
Gothenburg, Sweden 2020

Utilising Type 4 wind turbines for black start and off-grid operations
Design of a power synchronisation controller
ARVID BJÖREMARK, ALBIN BJÖRKMAN
Department of Electrical Engineering
Chalmers University of Technology

# Abstract

With an increasing number of renewable energy sources that are being implemented into the grid, the grid has become more complex than in the past. With this change in topology, new challenges arise regarding maintaining power quality and system stability. A future with higher penetration of converter connected energy sources could potentially lead to a decrease in system stability due to the decrease of grid forming units that naturally offer inertia. This requires new control methods for the converter connected sources to be implemented to allow for grid forming capabilities and still manage to regulate grid parameters to prevent the grid to be prone for faults, or in the worst case a system collapse.

This thesis has investigated grid forming control structures, for voltage source converters in Type 4 wind turbines, to allow for black start and off-grid operations. In this thesis, the wind turbine has been simplified so that the machine side converter is represented by a constant power source into the DC-link and a grid side converter that will control the voltage and frequency output to the grid. A power synchronisation controller has been implemented both in Simulink to test the controller's behaviour during different operation scenarios such as various grid-strengths, different resistive ratios in the grid, addition of droop controller and addition of virtual inertia, as well as in DIgSILENT PowerFactory to test if the controller could be modified to enable black start and off-grid operations.

The results show that the controller can be viable for implementation. The controller has successfully been modified to enable black start in both soft (ramping of voltage) and hard energising approach. It is concluded that soft energisation is a viable method that reduces inrush currents and voltage transients, which in some grid-setups could reduce the energy needed during black starts. The controller has also been modified to change the power from the machine side converter to allow for load-changes in the grid during off-grid operations.

It is recommended to either design the converter with headroom for the overshoots that occurs during steps in power or to implement a current limiter. However, such a limiter might interfere with the synchronisation process. Furthermore, a different controller approach for the DC-link is recommended to further study the behaviour of the energy exchange in the DC-link capacitor. This would also allow for a future study of how much energy that is needed for successful implementation of virtual inertia, which would limit large frequency deviations.
**Keywords**: Wind power, Black start, Off-grid operation, Renewables, Grid forming, Power synchronisation, Virtual inertia, DIgSILENT PowerFactory, Simulink.

# Acknowledgements

We would like to offer our gratitude towards Lucas Thomée who has been both a source of guidance and support. Professor Massimo Bongiorno for his interest and dedication in the subject. PhD student Anant Narula for his assistance and guidance and most of all taking time off from his work to offer us help in a time were the project needed it. Lastly, we would like to offer our gratitude towards DNV-GL for offering workspace and additional help with simulations as well as all the employees for their support.

Arvid Björemark and Albin Björkman, Gothenburg, June 2020

# Contents

# List of Figures

# List of Tables

# 1

# List of Abbreviations

BESS: Battery Energy Storage System

DFIG: Doubly-Fed Induction Generator

DG: Distributed Generation

EMF: Electromotive Force

ES: Energy Storage

GSC: Grid Side Converter

HV: High-Voltage

HVDC: High-Voltage Direct Current

LFDD: Low Frequency Demand Disconnection

LV: Low-Voltage

MSC: Machine Side Converter

PCC: Point of Common Coupling

PLL: Phase-Locked Loop

PMSG: Permanent-Magnet Synchronous Generator

PS: Power Synchronisation

PSC: Power Synchronisation Controller

RES: Renewable Energy Sources

RoCoF: Rate of Change of Frequency

SCADA: Supervisory Control And Data Acquisition

SG: Synchronous Generator

SCC: Short Circuit Capacity

SCR: Short Circuit Ratio

TSO: Transmission System Operator

THD: Total Harmonic Distortion

UPS: Uninterruptible Power Supply

VRR: Variable Rotor Resistance

VSC: Voltage Source Converter

VSM: Virtual Synchronous Machine

WPP: Wind Power Plant

WRIG: Wound Rotor Induction Generator

WT: Wind Turbine

# 2

# Introduction

## 2.1 Background

In order to reduce carbon-emissions Sweden has set a target of 100 % renewable energy production by 2040 [1]. To reach the target renewable energy sources (RES), produced by solar and wind power, is increasing and conventional power plants, such as nuclear power in Sweden, are being decommissioned [2],[3]. This change in structure has raised the complexity of the system due to small-scaled energy-generation dependent on stochastic sources such as wind and sun, instead of large plannable generation units. This increases the requirement of having a smarter grid that can handle the continuously changing network of loads and generation [4].

As a result of replacing conventional generation with RES, that uses fast converters, the system strength is of greater importance. If the grid is weak with a high voltage sensitivity, complications may occur due to the quick response of reactive power injection into the grid from the converters, leading to un-damped voltage oscillations. Therefore, the combination of the grid strength and speed of the converter will have an impact on dynamic response and grid stability. If the converters are not properly integrated into the grid, it could lead to system collapse, hence black start is needed to form the grid [5].

To date, in Sweden hydropower plants and thermal power plants have been supplemented with suitable equipment to enable black start and off-grid operation [6]. Renewable resources like wind turbines (WTs) are connected only when there is a stable and strong grid available [7]. Partly due to that the WTs operate in a grid following way, i.e it requires an existing grid to operate but also the stochastic behaviour of wind that leads to fluctuations in output power of the WTs, may lead to new blackouts if the grid is not strong enough [7]. With regards to the climate goals and increased wind power production, black start and off-grid operation capability should be provided with other resources, such as utilising wind power turbines [8],[9].

As a result of this, a new type of control-structure that is grid forming, i.e possess the ability to create the frequency and voltage, is needed for other grid-connected units to have reference and obtain stable operations. To solve this problem, several control methods have been developed to mimic the mechanical behaviours of synchronous generators and by so making the transition from mechanical created inertia to synthetic inertia or controllers that synchronises the power output after the demand.

## 2.2 Aim

The aim of this thesis is to investigate the possibility of providing grid forming capabilities with a Type 4 wind turbine by implementing and testing a grid forming control-structure. This includes energisation of a simplified grid and having the wind turbine solely provide stable operation for changing loads in an off-grid scenario. The aim is to successfully test the converter in simulations and offer a comprehensive literature review of available academic solutions.

## 2.3 Power system challenges with high penetration of converter connected energy sources

The European Network of Transmission System Operators for Electricity, ENTSO-E has a Ten-Year Network Development Plan where different scenarios of future electrical generation in Europe has been considered. In the 2018 version of the report, it is predicted that by the year of 2030 total annual energy demand in Europe covered by RES will be 48% to 58% and by 2040 the amount will be between 65 to 81% [10]. In the 2016 version of the report, ENTSO-E predicted that the installed wind capacity in Europe by 2030 will be between double and triple the amount of the installed wind capabilities in 2014 [11].

As the consumption changes with time and the needs for more environmentally friendly production increases, there is an uprising trend regarding the production of energy using renewable sources as seen from the European commission's statistics in [12]. In a technical report published by ENTSO-E in 2020 potential problems regarding high penetration of RES has been analysed from a system operator point of view [13]. ENTSO-E has targeted some areas of concern with the low system strength characterised by high penetration of RES. The areas of concern are as follows;

### 2.3.1 Creating system voltage and requirements for it to stay stable

Creating system voltage requires grid forming capabilities meaning that the converter acts as a voltage source. The requirements for it to be successful is that it should be able to create and control voltage magnitude, phase angle and frequency without being connected to an existing AC-grid. Converters can offer quick reactive power injection or absorption, although, in a weak grid that has problems with high voltage sensitivity, there could be a risk for undamped voltage oscillations [14]. The impact could be a loss in stability that makes the grid more prone for unwanted operation such as tripping of generators, low power quality or even complete blackouts

[15]. In [13], a suggestion for new requirements of how the converters should handle these grid-parameters is mentioned. It states that the converter or voltage source should be "capable of operating as a voltage source behind a reactance over a frequency band of 5 Hz to 10 kHz before, during and after a fault". Another important characteristic is the converters ability to limit voltage change when transients occur in the system [13].

### 2.3.2 Contribute to fault level

The short circuit capacity (SCC) in a power system is an important indicator of whether or not the system as a whole can maintain the system voltage. For example, when a bus is shorted the surrounding buses, if the grid is strong, will not be affected as much in regards to voltage as the busses in a weak grid would. For converters that rely on injecting active and reactive power, it is important to have stable voltage levels since they depend on it. This means that the fault would not propagate to other terminals, thus having a lower risk for tripping loads or other equipment in the grid that eventually could lead to a cascading effect. Avoiding having the grid move into for voltage collapse that can lead to undesired operation and decreased power quality for the consumers [16].

Another problem, if the grid is weak, the SCC at a specific bus is lower leading to having a too low magnitude of fault current that may not be sufficient to trigger the protection equipment. What is wanted by the converter at this event, is to inject a current that can contribute to the fault current level so the protective equipment is triggered. The amount of current should be limited to the converters over-current capabilities, especially during faults that have low fault impedance [13]. In [17] it is mentioned that depending on fault location, its type as well as the time interval of fundamental period, the injected current changes according to these circumstances.

### 2.3.3 Sink for harmonics and unbalance

Two more topics of concern are how well the system will handle harmonics and unbalance. Synchronous machines have inductive harmonic impedances, due to the windings physically present in the machine, that will damp harmonic currents. Converters/inverters could be controlled in such a way that it mimics these behaviours of the synchronous machine without adding additional physical filters. They could also be controlled into an inductive-resistive behaviour which would result in increased damping compared to synchronous machines [13]. The reason being that this will also act to damp DC-properties, which synchronous machines does not offer since higher physical resistance leads to higher losses. However, there are a number of challenges contributed to control the converter based units in such a way. The converter has to be designed with headroom for the harmonic currents, studies involving harmonic content and how to distribute the current headroom needs to be conducted. How the contribution to harmonic damping is shared between units is yet to be decided but [13] suggests a proportional sharing according to the power output. Similarly, the decreasing number of synchronous generators results in a reduction of negative sequence impedance which leads to higher unbalance due to an increased negative sequence current [13].

### 2.3.4 Contribution to system inertia

With the change of increasing converter-based generation that is decoupled from the grid, thus decreasing the amount of inertia in the grid due to lack of heavy rotating equipment, exposing the grid's ability to recover from spikes in both frequency and voltage although the response from converters is quick [18],[19]. The traditional way of smoothing frequency and voltage spikes with a high rate of change of frequency (RoCoF), has been through the naturally occurring stored kinetic energy in synchronous machines that offers inertia.

One solution to let converter-based generation contribute to the system inertia is by adding possibilities of virtual inertia inside the control-structure of the converter. Challenges arise with this type of contribution not necessarily acting in the same underdamped way as synchronous machines, possibilities exist to have the system damped to a critical level and even be overdamped. The different approaches result in different benefits, however, these needs more investigation [13].

### 2.3.5 System survival to allow effective operation of low-frequency demand disconnection (LFDD)

Low-frequency demand disconnection (LFDD) or also called load shedding is the process of disconnecting demands to prevent a system collapse due to low frequency. This is considered a last resort and only used when the normal countermeasures fail to provide a frequency response that restores the grid frequency [20].

There is a concern that with higher penetration of RES the system strength will decrease leading to fluctuations in frequency becoming both faster and larger leading to the effectiveness of such measures being lowered [20]. ENTSO-E has specifically identified LFDD to be problematic during rare system splits where a part of the electrical network is separated and forms an electrical island. Since, the stability and strength in the formed electrical islands is dependent on the connected generation and loads and may be insufficient, leading to system collapse [13].

### 2.3.6 Preventing adverse control interactions

By connecting converters to the grid, it creates new resonant points, the magnitude of these resonances will vary in time depending on two things: the active behaviour of the converter and the passive components in the converter that is being connected to the grid. Based on the natural frequencies and the damping provided in the network consisting of loads, generators and the converters themselves that vary in close connection to the operating conditions, the network resonances and active behaviour of the converter changes [13].

Converters can amplify resonances depending on the harmonic impedance characteristics [13]. To prevent amplification of resonances at harmonic levels it is important that the converter does not destabilise the resonance, i.e having an amplifying behaviour for the resonance at the harmonic level, since this would affect the stability of the grid.

## 2.4 Task

There are several challenges that needs to be investigated and solved before a conclusion for this project can be made.

Firstly, it is important to obtain an understanding of how the grid is affected by the introduction of WTs. How will the inertia be impacted and how will the ability to handle voltage oscillations and frequency variations be affected when using WTs

The next question is regarding the maturity of control-structures for WTs to this date and the differences between grid following and grid forming converters for stable operations. A review of different converter-control techniques suggested from the academic world will be performed. Techniques and technologies that can be useful when implemented in the power system will be presented.

Thirdly, the possibilities of having WTs installed in the grid while ensuring normal operation as well as offering black start capabilities is the next part of the work. Its suitability will primarily be tested through modelling and simulations done in Digsilent Powerfactory while investigating the resulting effects on a simplified grid. Additional testing such as operations during different grid-strengths and how different parameters affect the converter controllers stability will be conducted in Simulink.

The last task is a study focused on the sustainability and ethical aspects of the project. It will conclude what type of societal and environmental effects WTs can have when implemented into the grid. Further, the use of WTs will be compared to existing conventional generation methods.

## 2.5 Scope

The following scope has been set to the project:

– This project focuses on the technical problems associated with utilising wind turbines for black start and off-grid operation. Regulations (if any) that prohibits off-grid operations or using wind power turbines for auxiliary services which will not be considered.

– The converter is modelled as a controllable ideal AC-source, all transients, harmonics and losses from the switching are neglected.

– Only wind power will be investigated, other RES will not be considered. However, similar control structures might be applicable for other RES, such as solar.

– Full converter wind turbines (Type 4) have been selected for investigation during the simulations. The simulated network will be limited to a fixed size and complexity.

– Sufficient wind is assumed to be available at all times. Leading to the assumption of a constant power output from the machine side converter. In reality, this is not the case, which makes it harder to predict if the resources needed to perform a black start or operate in off-grid situations at a certain time is enough for a successful operation.

– For black start it is assumed that the problem is to energise the grid, no investigation is done regarding the startup of the WT. All ancillary services as the pitching of the blades and turning of the nacelle are assumed to be done by a UPS or diesel generator. This assumes that the wind turbine is always providing the right amount of input power needed at any time to the converter.

– For black start it is assumed that sufficient energy, either from wind or additional energy storage, is available to maintain the nominal voltage at the DC-link.

– Fault investigations will not be conducted to see fault-ride-through capabilities of the converter.

# 3

# Theory

In the following Chapter, the theory used throughout this thesis is introduced and explained.

## 3.1 Types of wind turbines

Wind power technology uses energy from the wind to convert it into electric energy. Currently four different types of WTs exist on the market [21]:

- Type 1: induction generator
- Type 2: wound rotor induction generator
- Type 3: doubly-fed induction generator
- Type 4: induction or synchronous generator with full converter interface

Type 1 (seen in Figure 3.1) is the most basic type of WT and is constituted by an induction generator (IG) directly connected to the grid by a step-up transformer (TR). It is commonly equipped with mechanically switched capacitor banks (C) to ensure compensation of reactive power. Both the generator and capacitor banks are disconnected from the grid by the main circuit breaker (CB) if a fault occurs. Type 1 WTs operate with fixed rotor speed, i.e the wind speed does not affect the rotational speed of the generator. Instead, the rotor speed follows the synchronous speed that is based on grid frequency [21].

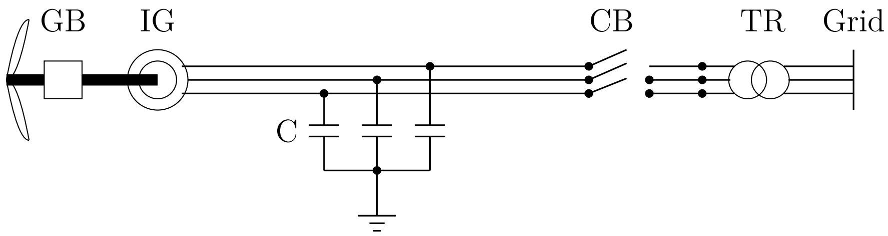


**Figure 3.1:** Model of Type 1 wind turbine, GB is the gear box, IG is the induction generator, C is the mechanically switched capacitor bank, TR is the step-up transformer and CB is the circuit breaker.

Type 2 WTs (seen in Figure 3.2) are similar to the Type 1 since they are also directly grid-connected. However, instead of using an IG, a wound rotor induction generator (WRIG) is used, where the rotor winding is connected to slip rings that can act as a variable rotor resistance (VRR), that is regulated by the use of power electronics. This allows the slip of the generator to be controlled making it possible to adjust the rotational speed up to 10% over the synchronous speed [21].

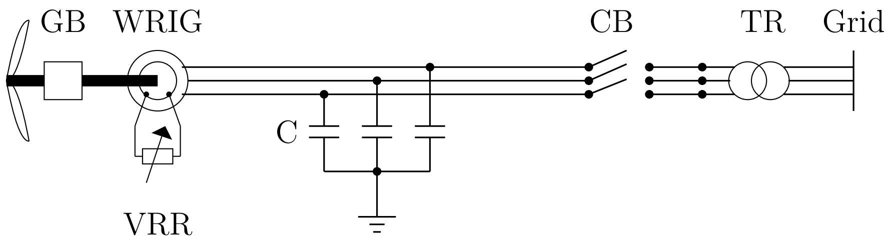


**Figure 3.2:** Model of Type 2, GB is the gearbox, WRIG is the wound rotor induction generator, VRR is the variable rotor resistance, C is the mechanically switched capacitor bank, TR is the step-up transformer and CB is the circuit breaker.

Type 3 WTs (seen in Figure 3.3) uses doubly-fed induction generators (DFIGs) with the stator windings connected directly to the grid, while the rotor windings are connected to the grid through a back-to-back voltage source converter (VSC), that consists of a machine side converter (MSC) and grid side converter (GSC). The MSC regulates active and reactive power by changing the rotor position and the GSC ensures a stable voltage over the DC-link. The DC-link is used for temporary energy storage for switching events, typically being small in size it is not used to absorb excess energy from the machine side or inject energy to the grid side to restore voltage levels. The amount of power that is typically passing through the converter is roughly 40% of total power output [21]. Type 3 WTs can encounter problems during low voltage ride through operations. If a voltage dip occurs at the point of common coupling (PCC), the current magnitude will increase in the stator leading to large transients in the rotor (converter) [22]. This will require an over-dimensioned converter to avoid tripping.

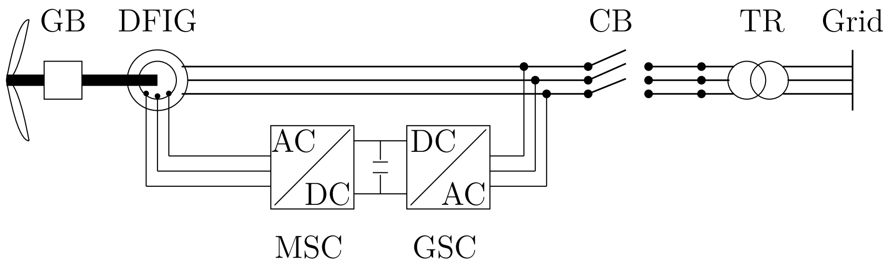


**Figure 3.3:** Model of Type 3, GB is the gearbox, DFIG is the doubly-fed induction generator, MSC is the machine side converter, GSC is the grid side converter, C is the mechanically switched capacitor bank, TR is the step-up transformer and CB is the circuit breaker.

The last and most complex WT, the Type 4 (seen in Figure 3.4), is constituted by a generator (either IG or synchronous generator (SG)) that is connected to the grid via a full-converter. By being fully decoupled from the grid, it offers better low-voltage ride through capabilities compared to Type 3. However, the losses will be bigger with Type 4, since all the current passes through the converter, hence needing higher ratings leading to higher switching and conduction losses. Similar to Type 3, the MSC adjusts the rotational speed and the GSC tries to reduce reactive power consumption while transmitting active power to the grid. As of now, the SG can be implemented by either using wound-rotor or by a permanent-magnet setup. Thanks to the permanent-magnet synchronous generators (PMSG) ability of self-excitation which results in a high power factor and efficiency, the latter is more commonly used.

Another advantage is that the gearbox can be removed with a PMSG, i.e change from a gearbox driven to a direct-driven WT. This increases the reliability of operation since the gearbox is one of the components that require regular maintenance in a WT. The main drawback of a full-converter is that all current flows through it, which can be a problem regarding protection if exposed to transients [21].

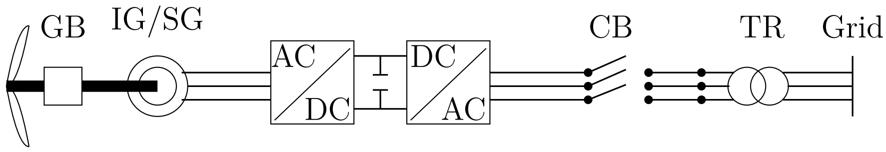


**Figure 3.4:** Model of Type 4, GB is the gearbox, IG/SG is the induction generator/synchronous generator, C is the mechanically switched capacitor bank, TR is the step-up transformer and CB is the circuit breaker.

## 3.2 Strength of grid

System strength is a term which typically describes the stability of the grid. System strength is usually defined by the short circuit ratio (SCR) or SCC. SCR is the ratio of how much power the system can provide during faults compared to the rating of the connected element and SCC is the magnitude of the power it can provide during faults. A high fault current ratio compared to load current or rather high SCR is typically corresponding to a high voltage level and small Thevenin impedance of the grid. If the Thevenin impedance of the grid is small then the change of current in the grid has to be larger for the voltage at the generator terminal to change. This results in better voltage stability for strong systems. For wind-power, a very strong system typically has a SCR of 10 and a very weak system a SCR of 1 [5],[23].

A strong grid means that if the current varies, the voltage at the PCC will maintain the voltage at roughly the same magnitude. Meanwhile, a weak grid with high Thevenin impedance will make the voltage of the PCC vary much more if the current starts to increase or decrease [5].

## 3.3 Black start, off-grid and islanding operation

### 3.3.1 Black start

In order for proper operation of a grid, supply and demand need to be in balance in such a way that the network parameters as frequency and voltage operate at a stable level. However, it is not unusual to move into unwanted operation where there is a risk for load shedding or even blackouts. If the latter occurs, the grid needs to do a restart and certain generators must act in grid forming mode to shape frequency and voltage according to the grid codes. This operation is called a black start and is something transmission system operators (TSOs) need to perform directly after a blackout [24] or grid energisation in general.

Black start from a power system perspective is a process of restoring the electrical network after a total or partial blackout [8]. Black starts can be engaged through either a top-down or a bottom-up approach (or a combination of both). Using resources within the blackout area is referred to as bottom-up strategy, whereas using resources outside the blackout area to energise the dead grid is considered as top-down [25].

#### 3.3.1.1 Soft and Hard energisation

The traditional black start approach, also known as hard energisation, is a process of restoring the grid power by first energising the black starting unit terminal voltage to 1 $p.u$ then connecting to the grid to energise transformers and lines; this will create inrush currents in the transformers and transient over-voltages [26]. This phenomenon can result in an oscillating behaviour that can damage the grid equipment or trip the black start unit, leading to a failed black start [27]. In order to limit the inrush currents, new black start procedures have been suggested, one of which is the soft energisation approach [27],[28].

Soft energisation tries to limit over transients and inrush currents by gradually energising all involved grid components, such as cable and plant transformers, by ramping the voltage level from the black starting unit from 0 to 1 $p.u$ while connected to the grid components. This requires the black start unit to be able to control its terminal voltage in gradual steps from 0 to 1 $p.u.$ This approach has been proven through simulations to be a viable option also for voltage source converters [28].

Some major benefits of using soft energisation approach are that the system restoration is typically successful during the first attempt, the risk of damaging network components is reduced (since the transient over-voltages and inrush current are minimised) and that this approach requires less available generation capability [27]. A drawback, however, is that the energisation process will take longer time. Another drawback is that depending on the grid size it might not be possible to implement if the top-down energisation approach is to be used.

#### 3.3.1.2 Black start capability for wind turbines

Previously proposed solutions of engaging black start with WTs consists of an external diesel generator to both mimic an existing grid and powering the WTs auxiliary services [29]. Solutions of using the energised WT to offer auxiliary support during start-up of other WTs in the wind power plant (WPP) that does not have the support of a diesel generator has also been proposed [30].

Theoretically, it is possible to perform black starts with WPPs without external diesel generators mimicking an existing grid, instead, a smaller diesel generator or an uninterruptible power supply (UPS) could be used to only power the WPPs sensors and controllers. However, since the operation of WTs relies heavily on environmental conditions, there is a factor of unpredictability that needs to be taken into consideration [6]. To perform successful black starts with these factors in mind the WTs would require to have a grid forming control that can adjust according to the current situations, so that a stable and strong voltage source that can be used for energisation is obtained. The most suitable wind turbine for this purpose would be Type 4 since it is a full-converter model, that easily can be disconnected from the grid [21],[31]. Which can be a valuable capability if the energisation process is unsuccessful and it is necessary to cancel the energisation process.

A proposed solution for the black start process is presented in [32], stating it can be done in the following way for a WPP: Self-start of WT is done by using an internal backup power supply, this energises the auxiliary services such as pitching and yaw-mechanics. Once this is fully configured the self-sustained generation can be provided by letting the blades start to rotate, if wind is present, during this time the WT-converter operates in grid forming mode to power the auxiliary services & controls. Parallel operations and synchronisation between WTs starts when each turbine can sustain themselves. At this point, a WPP is formed with some units operating in grid forming mode, while other WTs operate in grid following mode to ensure a stable island operation and support voltage stiff characteristics of the WPP. To energise the array cables and the plant transformer, energy from the wind is extracted.

A potential step in the startup-strategy is to couple together several WPPs operating in off-grid mode to obtain a voltage stiff source that makes it possible to connect the plant to the grid by using e.g. a high-voltage direct current(HVDC)-link and voltage source converter (VSC). The last step is to ensure having a stable off-grid operation that can maintain its frequency and voltage when disconnection/connection of WTs (transients) or large load-pickups occurs. An illustrative block diagram of the proposed solution can be seen in Figure 3.5.

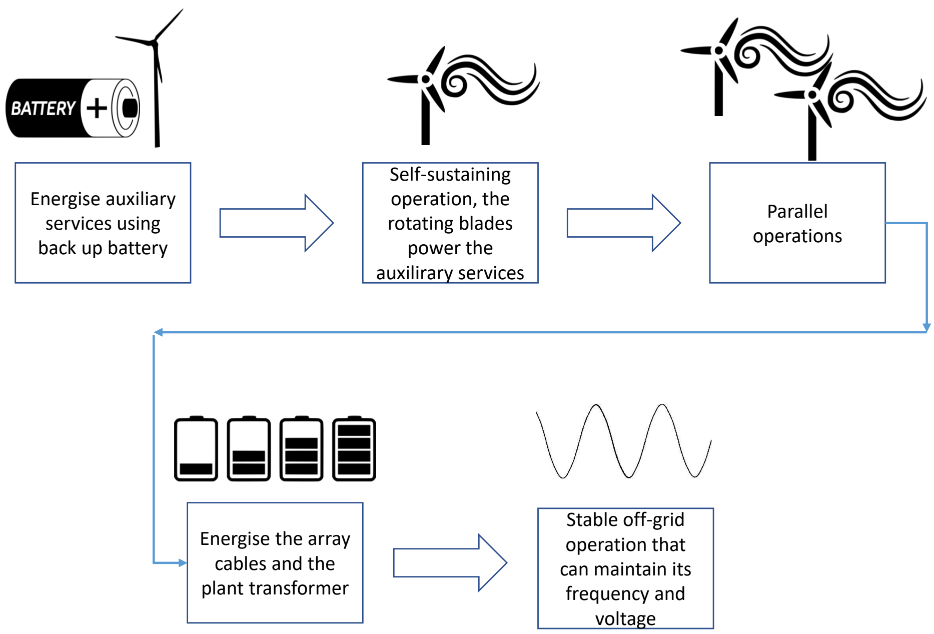


**Figure 3.5:** An illustrative figure of the proposed solution.

#### 3.3.1.3 Uninterruptible power supply (UPS)

As mentioned, the conventional way of offering black starts services has been done by using either a diesel generator or an UPS during startup to power the WT's auxiliary services [29]. Similar battery energy storage systems (BESS) have also been used as a supplementary to support frequency control when uneven wind conditions are present. The solution is based on the simple idea of filling in the gaps of power that is lost during variations in wind, that is done by releasing the stored energy from BESS and by so controlling the frequency [33].

If no BESS or diesel generator is used to act as a frequency reserve, other methods can be used to stabilise the frequency if dips occur. One of these methods is described in [34], which uses the stored kinetic energy from the rotor blades to emulate the inertial response of an SG. However, the conclusion has been that it offers a lower effect of inertial response compared to a SG, thus having a longer regulation time. It is pointed out that the control coupling is one of the reasons why this inertial response differs.

### 3.3.2 Islanding and off-grid operations

Nowadays, the distribution system does not only consist of the conventional power generation at transmission-level that is distributed down to consumers located at distribution-level. There also exist distributed generation (DG) in the form of RES that is located closer to the loads that offer small-scaled generation in the local network. Figure 3.6 illustrates the different grid topologies for conventional and distributed generation.

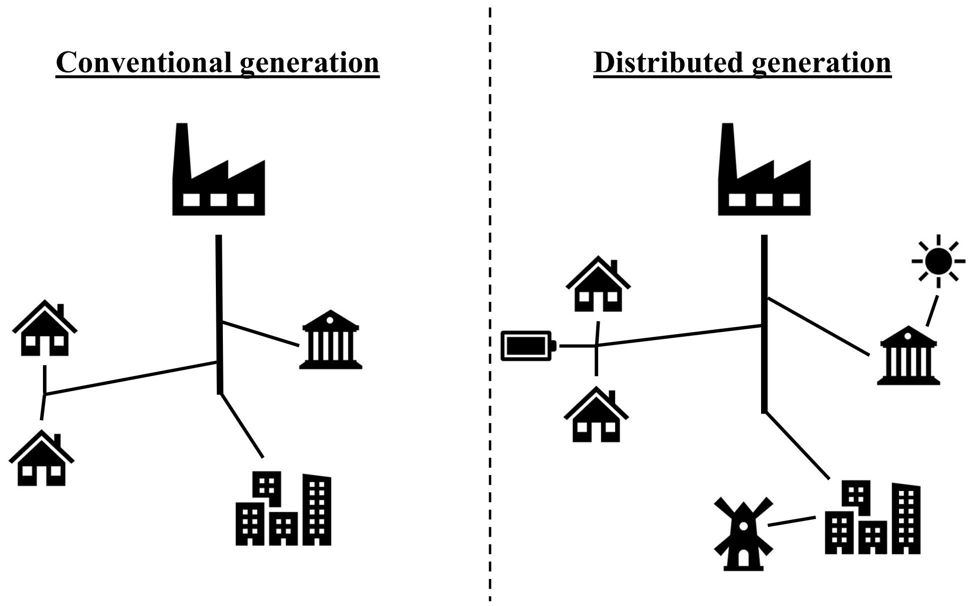


**Figure 3.6:** Topology differences between conventional and distributed generation. Visualising radial transmission system sued in the conventional method (left) and the meshed grid with small-scaled generation located close to the load demand (right).

If a fault were to happen in the local network that disconnects it from the main grid while still operating on its own, this event would be called islanding [35], and off-grid operation would be when a grid operates on its own without being connected to the grid. In the case of islanding, the distribution system needs to detect if the local network is disconnected from the main grid and if so possibly shut down the distributed generation if off-grid operation is prohibited by law in a specific country. In Figure 3.7 an illustration of how islanding operation can look like when an upstream fault disconnects the local grid from the main grid is shown.

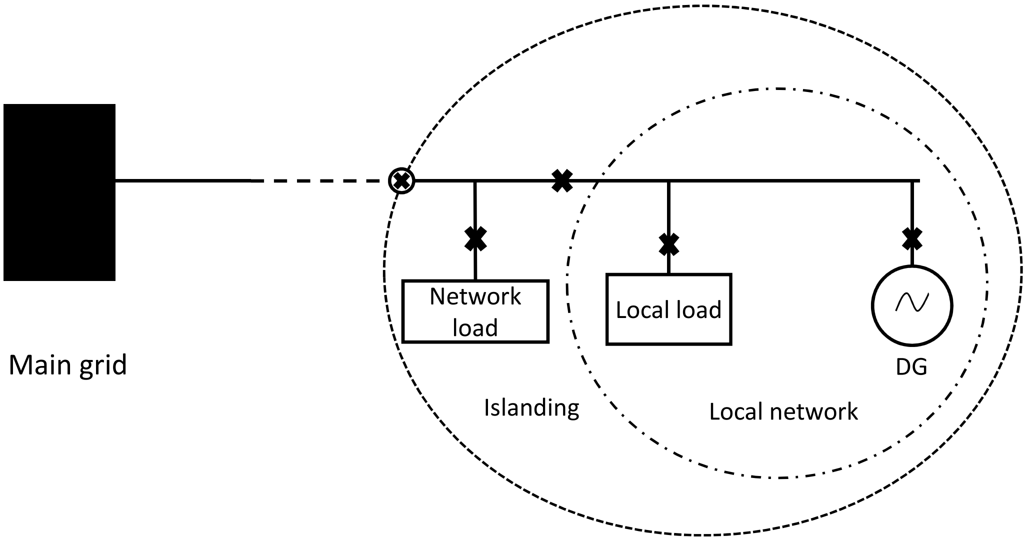


**Figure 3.7:** Islanding operation when a upstream fault has occurred , showing the disconnection of microgrid from main grid. DG is the distributed generation in form of small-scaled modular generation that can consist of renewable energy sources.

The off-grid operation can be the next step in the process of restoring the grid. During this operation, a restricted area after a black start operates individually from the grid and supplies its auxiliary services. When a stable operation has been reached, additional loads and generators are connected, if needed, before synchronisation to the main grid can be executed [24]. During off-grid operations, it is important that regulations and grid-codes are followed by the generating unit. For example, in Sweden, there are grid codes stating how much the frequency is allowed to change during different time intervals. In [36], it is mentioned that generating units should be able to stay connected to the grid, despite deviations in frequency. The different frequency ranges and maximum time thresholds a unit should be able to handle while withholding connection to the grid is presented in Table 3.1.

**Table 3.1:** The frequency ranges that a generating unit should be able to handle without disconnecting from the grid, and the total time it shall operate within each range.

| Frequency [Hz] | Time [in minutes] |
|---|---|
| 47.5-48.5 | 30 |
| 48.5-49.0 | 30 |
| 49.0-51.0 | Unlimited |
| 51.0-51.5 | 30 |

#### 3.3.2.1 Detection techniques for islanding

Detection of islanding can be done in several ways, in [35] a review of detection methods are presented. Stating that there are remote techniques in the form of supervisory control and data acquisition (SCADA), that can be used to detect unintentional islanding by monitoring grid parameters such as voltage and frequency. If such parameters can be monitored in a certain part of the grid, despite being disconnected, then it is in unintentional islanding. But there are also local islanding detection techniques that either work in a passive way, i.e monitors grid parameters and see if there are any big deviations in voltage, frequency, phase angle or total harmonic distortion (THD) compared to regular operation. As well as active techniques that applies small disturbances to the grid while observing the response to determine if it is operating in islanding mode. A common way of doing this is to send reactive power from the DG to the grid and check if there are any deviations in frequency [37]. There are also hybrid versions that combine passive and active detection techniques by letting the active techniques being activated only when islanding is being detected by the passive techniques [35].

Furthermore, in [35] and [38], it is mentioned that there are other methods for identification of islanding based on signal processing, which is meant to be quicker and have higher accuracy. By using signal processing methods such as Fourier transform, wavelet transform and s-transform it is possible to find deviations in the measured signal, that later can be used as input for artificial intelligence classifiers. The idea is to gain higher accuracy and make better decisions based on the disturbance type, which would result in faster detection times and more suitable actions.

#### 3.3.2.2 Moving from off-grid operation to grid-connected operation

During off-grid operation, the control for the RES that uses converter monitors the power flow, generation and consumption, and adjusts the power output from RES to maintain power supply to the most critical loads. Energy storages (ES), if installed, and DGs are kept within allowable ranges during this stage. If the power balance is not kept, load shedding or adjustments of DG output power to keep balance inside the islanded grid can be done. RES are aimed to be set to maximum operation levels and ESs are charged or discharged depending on the situation [39].

When stable operations have been established and the main grid senses the busbar voltage on the LV side to be the same magnitude as in the terminals of the islanded network as well as the frequency and phase order is the same, the switch to main grid closes. If this is done correctly, the transfer from off-grid operation mode to grid-connected will be smooth. The restoration of dispatched DGs and loads will once again be connected and ESs will be charged to prepare for possible future off-grid operations. The energy management system will continue to monitor and control the power flow, to maintain power balance and act if needed [39].

## 3.4 The swing equation and relation to inertia

The swing equation is used to describe the mechanical and electrical side of a SG, it states the dynamics during acceleration or de-acceleration of the rotor in the generator. The power exchange between the machine rotor and the grid is called the inertial response. The swing equation is based on the motion of the machine rotor as

$$J\frac{d^2\theta}{dt^2} = T_m - T_e = T_a, \tag{3.1}$$

where J is the total moment of inertia, $\theta$ is the angular position of the rotor, $T_m$ is the mechanical torque, $T_e$ the electrical torque and $T_a$ is the resulting accelerating torque obtained when the losses are neglected. When $T_a$ is equal to zero it means that the $T_m$ and $T_e$ are equal and by so also stating that the machine is in steady-state, i.e the rotor will rotate at the synchronous speed $\omega_s$.

The angular rotor position is measured in the $\alpha\beta$-frame, but can be represented with respect to the $dq$-frame by reformulating it as,

$$\theta = \omega_s t + \delta, \tag{3.2}$$

where $\delta$ is the measured angular position in $rad$ with the synchronously rotating frame. From this, we can derive the equation 3.2 to

$$I_s = \frac{v_1 cos\delta - v_2 + jv_1 sin\delta}{jX} \tag{3.3}$$

which can be rewritten as,

$$\omega_r = \frac{d\theta}{dt}, \tag{3.4}$$

so that the rotor angular speed, $\omega_r$, can be obtained. From this, it is possible to say that the angular speed of the rotor is equal to the synchronous speed only when the derivative of $\delta$ is zero. By this statement, d$\delta$/dt can be seen as the error in the speed

$$\omega_r - \omega_s = \frac{d\delta}{dt}. \tag{3.5}$$

By taking the derivative of (3.4), the equation of motion of the machine rotor 3.1 can be written as

$$J\frac{d^2\delta}{dt^2} = T_m - T_e = T_a \tag{3.6}$$

and then multiply equation 3.6 with $\omega_r$ on both sides the following equation is obtained;

$$J\omega_r\frac{d^2\delta}{dt^2} = P_m - P_e = P_a, \tag{3.7}$$

where $P_m$, $P_e$ and $P_a$ are the mechanical, electrical and accelerating power in MW. Following, the inertia constant can be defined as

$$H = \frac{Stored\ kinetic\ energy}{Generator\ rating} = \frac{J\omega_s^2}{2S_{rated}}, \tag{3.8}$$

by substituting (3.8) into (3.6) following equation is obtained;

$$2H\frac{S_{rated}}{\omega_s^2}\omega_r\frac{d^2\delta}{dt^2} = P_m - P_e = P_a \tag{3.9}$$

and by assuming steady state conditions, $\omega_r$ can be replaced by $\omega_s$ since the machine angular speed is the same as the synchronous speed. The final swing equation is now defined as

$$\frac{2H}{\omega_s^2}\frac{d^2\delta}{dt^2} = P_m - P_e = P_a. \tag{3.10}$$

In (3.10) the rotor dynamics of a SG is now described and the angle $\delta$ (also called the load angle) represents the angle of the internal emf of the SG that decides the amount of power being transferred.

For RES like wind, the inertia provided to support the loss of power is much lower or rather non-existent compared to what is offered in conventional generation like hydro, due to the use of high-power converters that disconnect the output from the rotating mass. Although there are newer installations of WTs that can provide inertia by using the stored energy in the rotating blades, the contribution is too low to offer enough support to the grid. The current solution is to offer synthetic inertia by implementing converter control based on the swing equation, i.e emulate the rotating mass that is inherent in SGs and by so keeping the operations stable.

In [40], virtual inertia was applied to the Great Britain system model, with increasing penetration of wind it was seen that the RoCoF was slowing down, while the minimum value of frequency measured during transients (frequency Nadir) decreased. One of the proposed solutions to the frequency Nadir issue was to implement pitch angle control in combination with synthetic inertia to withdraw more power from the WT when the frequency was to be restored.

## 3.5 Synchronous machines and their abilities of power-synchronisation

The reason why a power-synchronisation control for the VSC can be used is explained by the following example. Imagine having two SM connected ($SM_G$ and $SM_M$) to each other while being decoupled by the reactance, $X$, that consists of the reactance from both SMs and the line that is being used to connect the two SMs, other resistances and damping effect are neglected. Assume that $SM_G$ is set to operate as a generator and $SM_M$ is set to operate as a motor, the simple schematic of the model can be seen in Figure 3.8.

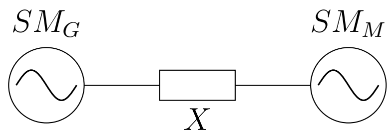


**Figure 3.8:** A simplified model of two synchronous machines (SMs). Whereas $SM_g$ operates as a generator and $SM_M$ operates as a motor.

Both SMs are operating at steady state initially and their inner electromotive forces (EMFs) are represented by the line-to-line equivalent phasors, $E_G$ and $E_M$. An assumption is made that the EMFs are constant at all times even if there are transients in the system. To describe the transmitted power between the two SMs, the following equation is used

$$P = \frac{E_G E_M sin\Phi}{X} \tag{3.11}$$

$\Phi$ is the electrical angle between the two phasors. To describe the relation between mechanical ($T_m$) and electromagnetic torque ($T_e$) and the resulting total inertia ($J$) for one SM, the following equation can be used

$$J\frac{d\omega_r}{dt} = T_m - T_e \tag{3.12}$$

where $\omega_r$ is the rotor speed. Now, the $T_m$ of $SM_G$ is increased for a short duration and then decreased to its steady-state value. Due to the increase of $T_m$, one can see from (3.12) that the mechanical angle will increase and since the rotor angle is strongly connected to the inner emf, there will be an increase of the emf phasor $E_1$. This will create a difference in emf between the two SMs, which means that the electric power transmitted from $SM_G$ to $SM_M$ will increase as a result which is explained by (3.12). In return, the $T_e$ of $SM_M$ will increase, while assuming $T_m$ is constant the rotor increases its speed. Meanwhile, the phasor $E_M$ also increases and with this, the difference in EMFs between the two SMs are reduced. The system will regain its initial values once a transient occurs and move back into steady-state operation [41].

From this example, one can understand that there is a response if one SM changes its angular position the other one connected will react in a similar way to maintain the synchronism. In a bigger system where more SMs are being interconnected, a similar response will happen, due to the nature of SMs wanting to stay in synchronism.

## 3.6 Transformation of three-phase signals

### 3.6.1 Clarke and inverse Clarke transformation

A balanced three-phase system $S_{abc}$ can be transformed into a vector in the $\alpha\beta$-frame, which is a complex reference frame, by applying the Clarke transformation [42]. The transformation is defined as

$$\vec{S}(t) = s_\alpha + js_\beta = K\left[s_a(t)e^{j0} + s_b(t)e^{j\frac{2}{3}\pi} + s_c(t)e^{j\frac{4}{3}\pi})\right], \tag{3.13}$$

where $K$ is the space vector scaling constant and can be chosen either as 2/3 for amplitude invariant scaling or $\sqrt{2/3}$ for power invariant scaling. Both approaches have their advantages but the latter is especially useful if power is to be calculated since the active power in $\alpha\beta$-frame can be calculated as

$$P = i_\alpha \cdot v_\alpha + i_\beta \cdot v_\beta. \tag{3.14}$$

Equation (3.13) is most commonly expressed as a matrix equation as,

$$\begin{bmatrix} s_\alpha \\ s_\beta \end{bmatrix} = K \begin{bmatrix} 1 & -\frac{1}{2} & -\frac{1}{2} \\ 0 & \frac{\sqrt{3}}{2} & -\frac{\sqrt{3}}{2} \end{bmatrix} \begin{bmatrix} s_a \\ s_b \\ s_c \end{bmatrix} \tag{3.15}$$

where K can be chosen as previously described. The system is thereby reduced into two components instead of three and if the system is balanced (no zero sequence) the original 3 components can be found without any loss of information using the inverse Clarke transformation described as

$$\begin{bmatrix} s_a \\ s_b \\ s_c \end{bmatrix} = K \begin{bmatrix} 1 & 0 \\ -\frac{1}{2} & \frac{\sqrt{3}}{2} \\ -\frac{1}{2} & -\frac{\sqrt{3}}{2} \end{bmatrix} \begin{bmatrix} s_\alpha \\ s_\beta \end{bmatrix}. \tag{3.16}$$

The comparison between the three-phase reference frame and the $\alpha\beta$-frame is shown in Figure 3.9. The comparison between the transformed signals and the original signals are shown in Figure 3.10.

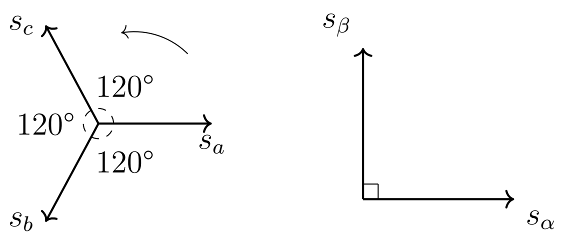


**Figure 3.9:** The reference frames for three-phase and $\alpha\beta$-frame respectively.

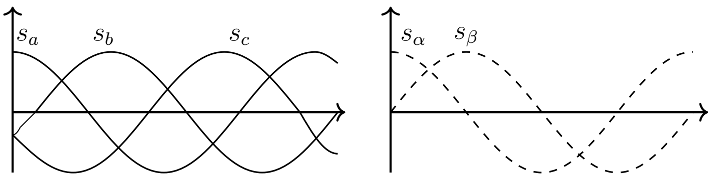


**Figure 3.10:** The generic wave forms for three-phase and $\alpha\beta$-signals respectively.

### 3.6.2 Park and inverse Park transformation

While the $\alpha\beta$-frame reduces a balanced three phase system to a two phase system the frame is stationary and the system is still considered as AC system, the *dq*-frame is a rotating frame that rotates with the speed of the angular frequency of the system. This leads to that within the *dq*-frame the quantities can be considered as DC. The transformation between $\alpha\beta$-frame to *dq*-frame can be done using the Park-transformation described as,

$$s_{dq}(t) = s_{\alpha\beta}(t) \cdot e^{-j\theta(t)} \tag{3.17}$$

which in component form can be written as,

$$\begin{bmatrix} s_d(t) \\ s_q(t) \end{bmatrix} = \begin{bmatrix} cos(\theta) & sin(\theta) \\ -sin(\theta) & cos(\theta) \end{bmatrix} \begin{bmatrix} s_\alpha(t) \\ s_\beta(t) \end{bmatrix}. \tag{3.18}$$

Similarly the inverse transformation is described as,

$$s_{\alpha\beta}(t) = s_{dq}(t) \cdot e^{j\theta(t)}, \tag{3.19}$$

or by the matrix form as,

$$\begin{bmatrix} s_\alpha(t) \\ s_\beta(t) \end{bmatrix} = \begin{bmatrix} cos(\theta) & sin(\theta) \\ -sin(\theta) & cos(\theta) \end{bmatrix} \begin{bmatrix} s_d(t) \\ s_q(t) \end{bmatrix} \tag{3.20}$$

The comparison between the $\alpha\beta$-frame and the *dq*-frame is shown in Figure 3.11 and the comparison between the transformed signals are shown in Figure 3.12

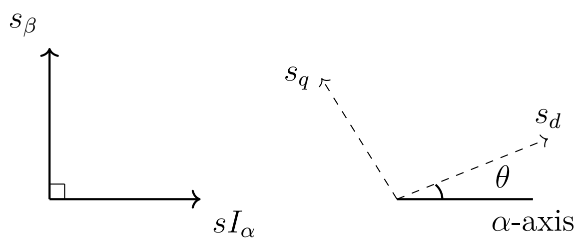


**Figure 3.11:** The reference frames for $\alpha\beta$ and $dq$-frame respectively.

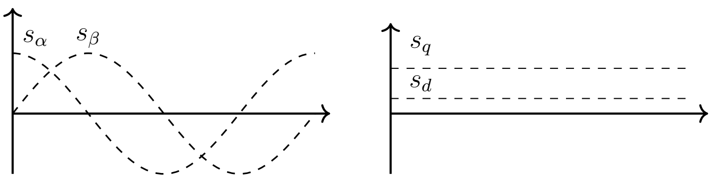


**Figure 3.12:** The generic wave forms for $\alpha\beta$ and $dq$-signals respectively.

If the power invariant transformation was used in the Clarke transformation the active power can be described as

$$P = I_d \cdot V_d + I_q \cdot V_q \tag{3.21}$$

and the reactive power as

$$Q = I_d \cdot V_q - I_q \cdot V_d. \tag{3.22}$$

The transformation to $dq$-frame is a powerful tool since it allows the system to be controlled in DC quantities which is easier than AC quantities. This also enables the possibility of using an integral controller to remove errors and allows for easier transient analysis.

### 3.6.3 Phase estimation

For the transformations to work, knowledge about the grid-angle in the PCC ($\theta$) is required. One way of estimating the angle is by the use of a phase estimation algorithm as described in [43] and visualised in Figure 3.13. This approach uses the $q$-component of the voltage passed through a PI controller to obtain an angular frequency difference compared to the nominal angular frequency. The angular frequency of the voltage is obtained by addition of the nominal angular frequency. If integrated the angle in radians is obtained.

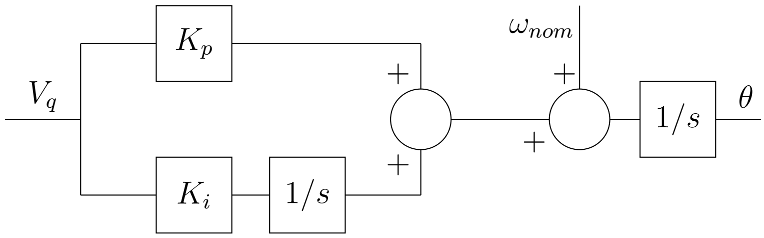


**Figure 3.13:** Phase estimation device setup. $V_q$ is the $q$-component of the voltage in the $dq$-frame, $Kp$ and $Ki$ is the proportional and integral gain, $\omega_{nom}$ is the nominal angular frequency and $\theta$ is the measured angle.

where $V_q$ is the $q$-component of the voltage in the $dq$-frame, $Kp$ and $Ki$ is the proportional and integral gain. In [44] $Kp$ and $Ki$ have been proposed as,

$$K_p = \frac{\omega_{band}}{V_{rated}} \tag{3.23}$$

and

$$K_i = \frac{\omega_{band}^2}{V_{rated}} \tag{3.24}$$

where $V_{rated}$ is the rated voltage and $\omega_{band}$ is the loop bandwidth of the phase estimator. In [44] it is stated that the loop bandwidth cannot be above 37.68 rad/s without affecting the output signal. This solution of measuring the angle will drive the $q$-component of the voltage to zero leading to the $dq$-frame of the voltage to be synchronised with the grid at the $d$-axis.

# 4

# Control systems for wind turbines

As the transition from centralised to decentralised and small-scale converter based generation is an evolving topic, certain problems may come up as an effect, mainly those mentioned in Section 2.3. To handle this shift in generation and the more complex flow of power in the grid, there is a need for smart and intuitive solutions for the control of power converters. In this chapter, some control methods are presented as well as explaining the differences of grid following and grid forming converters.

## 4.1 Grid following control compared to grid forming control

Typically renewable sources are connected to the grid using grid following control. This type of control structure operates by measuring the angle of the grid voltage at the PCC and produce a current that provides the correct reactive and active power to sustain a stable operation, i.e it is seen as a current source [45],[46]. The measuring and synchronisation are usually done by a phase-locked loop (PLL), that locks the output signal to its input so it matches the input signal's frequency and phase [47].

SGs are grid forming devices, due to the frequency being tightly connected to the rotational speed of the rotor and can, therefore, be used to provide a frequency reference to the grid following control. This type of control does not need an existing grid since it can regulate the frequency without using a PLL. However, in a converter, as opposed to a SG, the output is decoupled from the input, leading to a need to model the control in a grid forming way [46]. Converters using grid forming control structures are seen as voltage sources [48].

In Figure 4.1 the topology difference is shown between grid following and grid forming converters control structure. In the grid following case the angle at the PCC is estimated, using a PLL, together with the active and reactive power, these are compared to the reference powers and by using the angle at the PCC the correct current output is calculated in a current controller. In grid forming the active and reactive power are still measured at the PCC but rather than measuring the angle at the PCC the angle is calculated based on the difference between the reference active power and the measured active power. The voltage magnitude can be calculated from the reactive power controller and by using the calculated angle the converter reference output voltage can be obtained.

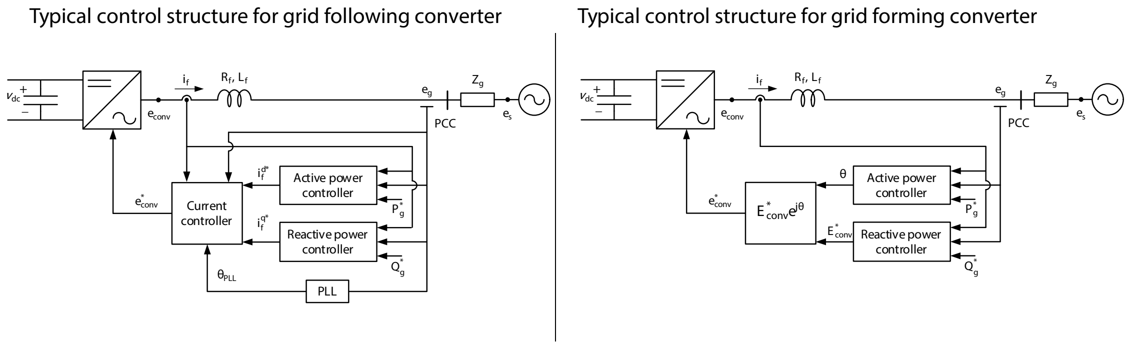


**Figure 4.1:** The typical control structures for grid following (left) and grid forming (right) converters, showing the difference in control-structure. In grid following the converter angle is synchronised to PCC angle using a PLL where as in grid forming it is calculated using a active power controller. Source: Adapted from [49].

As mentioned the transition to grid forming converters offers possibilities for new operations. However, grid following control methods have been proven to work for several years leading to it being better for some areas of operations. In Table 4.1 some capabilities of the two control methods are stated.

**Table 4.1:** Some functionalities of grid following and grid forming control systems for converters as stated in [49].

| Operation | Grid following | Grid forming |
|---|---|---|
| Dynamic performance | High | Medium |
| Fault ride-through | Yes | To be improved |
| Fault current contribution | To be improved | To be improved |
| Control interaction | Medium/high | Medium/low |
| Unbalanced operations | Yes | To be improved |
| Harmonic performance | Yes | Yes |
| Virtual inertia | To be improved | Yes |
| Weak grid operation | To be improved | Yes |
| Black start | No | Yes |

To offer virtual inertia, active power has to be exchanged between the converter and the grid. For this to be successful, it is important that the control system can offer enough energy for the desired inertia. The amount of energy needed is dependent on the characterisation of the inertial response but typically an energy storage system is required to offer sufficient energy [13].

## 4.2 Virtual synchronous machine (VSM)

This control method is based upon mimicking the SG by offering virtual inertia. This is done by implementing the swing equation and by so model the converter to act similarly as the SG. Since the converter does not have the same mechanical dynamics as a generator it can act much faster when needed [50]. However, to enable seamless implementation of converter based controls into the grid the converter is made to operate slow to obtain similar characteristics as the SG. The RES that uses VSM control will then be more ready to be incorporated into the grid since it mimics the behaviours SGs and therefore, does not create any uncertainties on how the grid will be affected to the same degree. To offer enough inertia response there is probably a necessity to install energy storage that has sufficient capacity to replicate the kinetic energy stored in the rotating mass of a SG, such as a battery system [50].

The VSM measures the voltage and current at the PCC to calculate active and reactive power. The active power is used to calculate the angular frequency reference, $\omega_{ref}$, and the reactive power is used to calculate the voltage reference, $V_{ref}$. By comparing $\omega_{ref}$ with the angular frequency of the grid, $\omega_g$, and passing the error through a PI-controller and a low-pass filter, the rotor angle, $\theta_r$, is obtained. The low-pass filter is added to offer virtual inertia, making the VSM have a response close to a SG. $V_{ref}$ together with $\theta_r$ makes it possible to calculate the sinusoidal voltage that is outputted from the converter, i.e the VSM can be seen as a voltage source [51].

In [52], the concept of VSM was further analysed to investigate the possibilities of improving the frequency stability. Conclusions were made mentioning that the concept of VSM could be helpful to decrease the frequency deviation, the RoCoF, and improve the dynamic response of the system, thanks to the implemented virtual inertia. However, the drawbacks are the need for a constant DC-link voltage, setting requirements of having extra energy storage at all times, and also that the control strategy does not fully make use of the fast dynamic response that is possible to have with inverters.

Lastly, by using the VSM concept to control the converters the phenomena of self-synchronisation that are present between SGs (explained in Chapter 3.5) can be used for automatic synchronisation of the voltage source inverter. Therefore there is no need for converter-coupled units to have a separate synchronisation algorithm that previously has been a requirement when connecting units to the grid.

## 4.3 Synchronverters

Synchronverters are another type of control, similar to VSM, that aims to mimic the behaviours of a SG. This makes it easy to operate as a grid-connected unit in the existing grid while offering the capabilities of renewable energy and distributed generation [53]. The synchronverter is based upon an electric part and a power part, descriptions of these two parts are found in [53].

The favourable aspect of the synchronverter is that it inherits all characteristics from the SG due to the inverter being based upon the complex swing equation, the only difference is that the inverter exchanges power with the DC bus while an SG does it by exchanging mechanical power with the prime mover. Because it is implemented virtually, each parameter such as inertia, friction coefficient, mutual and field inductances can be changed freely even though some values are not possible to have in a SG, but there is also an added flexibility of changing its parameters even during operation [54].

In combination with the energy storage a voltage controller is needed to maintain the DC-bus voltage to be constant, this can be done in two ways; By adjusting the synchronverter's reference power or change the power flow that is within the energy storage [53], [54]. If no energy storage and voltage controller is implemented, there will be complications of maintaining stable operation due to no physical way of either injecting or absorbing power into the grid to maintain frequency and voltage.

Another characteristic that is inherited from the SG is the control part that is divided into; The real power and the reactive power control. To control the real power a frequency droop control loop is used and to control the reactive power a voltage droop control is used. The integration of the controllers; Real power, reactive power, frequency and voltage can all be put together to create a compact controller that is easily controlled by four parameters [53].

Even though it is an inverter, over-and-under excitation can occur just like in the SG and it will act in the same way. This makes the integration of these inverters less problematic since the grid does not see any difference between the virtual version of a SG and a real one. There is even a possibility to run the converter as a motor, which could be a good option to high-voltage DC transmission lines. The idea is to have a synchronverter act as a motor on one end of the line while there is another synchronverter on the other end sending power, creating a power flow along the line [54].

Before connecting the synchronverter to the grid, information about the grid is needed for the synchronisation process. That is why a synchronisation unit is installed to gather this information. Another reason to have one is so that after the connection of the synchronverter has taken place, the right amount of real and reactive power is delivered from the converter on to the grid [53].

The drawbacks of using a synchronverter were concluded in [54], it was mentioned that the lack of large inertia that is present in a SG might affect the frequency stability, but this can be somewhat fixed by using short-term energy storage, usually in the form of battery that offers energy needed for inertia, that is implemented in conjunction with the synchronverter [54]. The energy storage is often located in a sealed container that is placed in close connection to the WT [55],[56].

## 4.4 Power synchronisation control (PSC)

Power synchronisation control (PSC) is another grid forming control approach. It uses the voltage angle and phase magnitude to control the active and reactive power while removing the need for a PLL. The concept is realised from the swing equation, what differs is that the swing equation for a SG depends on the change of angle that involves dynamics from the rotor and governor which is not present in a converter. In [41], the concept of PSC was introduced, and in [23] a robust solution of the PSC with design recommendations for the gains of the control loop and the DC-link controller were proposed. Compared to the VSM and synchronverter approach that also offers virtual inertia along with the grid forming capabilities the PSC is best suited for very weak grids and does not offer any virtual inertia at its general setup, removing the need for an energy storage in addition to the DC-link [23].

The PSC works by comparing the measured power output of the converter (which is assumed to be lossless) with the reference power (both in $p.u$), the error is then passed through a proportional control block, with gain $K_p$. To obtain $\theta$ in radians the input to the integration block has to be with the unit of rad/s, leading to the need to multiply the proportional constant with the nominal angular frequency. In [23], the proposed value of $K_p$ was $0.2 \cdot \omega_1$. If only this part of the PSC is utilised a poorly damped operation would occur which can lead to instability.

The solution is to implement the damping loop. The measured current, $i^s$ in the PCC is transformed from $\alpha\beta$-frame to $dq$-frame and then passed through a high pass filter. The filter bandwidth $\omega_b$ should be selected smaller than the nominal angular frequency, the proposed selection is $0.1\omega_1$-$0.2\omega_1$. $R_a$ is the active resistance that is proportional to the speed of the controller according to the following equation

$$\omega_{c,min} \approx \frac{R_a}{L_{max}}, \tag{4.1}$$

that is taken from [23]. $\omega_{c,min}$ is the minimum bandwidth, $L_{max}$ is the maximum expected grid inductance (set to 1 $p.u$ if SCR is $\geq 1$). The proposed selection of $R_a$ is 0.2 $p.u$ and $K_p$ should be equal to $R_a$ [23]. By subtracting the converter-voltage magnitude, $V$, with the high pass-filtered term, the new voltage reference to the pulse-width modulator can be obtained after being transformed to $\alpha\beta$-frame when multiplied with $e^{j\theta}$. The PSC control also has a current controller block that is transparent during normal operations but during transients limits the current. This is particularly needed during fault ride through [23].

In Figure 4.2 the PSC is presented without the cascaded outer control loop for the DC-link. $P_{ref}$ is the reference power in $p.u$, $P$ is the measured power in the point of common coupling (PCC), $\omega_1$ is the nominal angular frequency and the subscript $^s$ on the voltage and current represent that these are in the stationary-frame ($\alpha\beta$-frame). The wanted operation of the PSC is to select $v^s$ which is the converter voltage as $Ve^{j\theta}$ where V is the converter voltage magnitude expressed in the $dq$-frame.

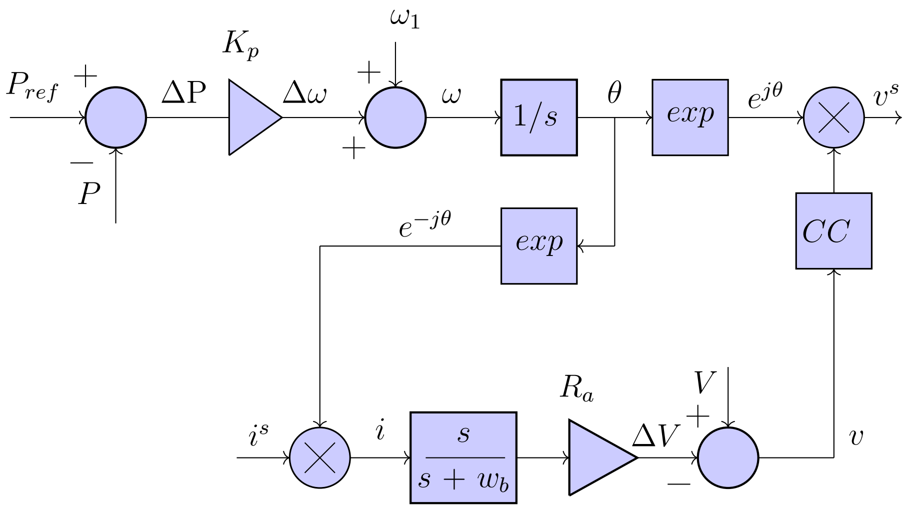


**Figure 4.2:** The control scheme for the power synchronisation control setup. $P_{ref}$ is the reference power for the controller, $P$ is the measured power at the PCC, $\omega_1$ is the nominal angular frequency, $K_p$ is the proportional gain of the controller, $R_a$ is the active resistance, $\omega_b$ is the bandwidth of the high-pass filter, $V$ is the output from the voltage controller, represented in $dq$-quantity, CC is a current controller and $v^s$ is the converter output voltage represented in $\alpha\beta$-frame.

The proposed solution for the implementation of DC-link control as presented in [23] can be seen in Figure 4.3.

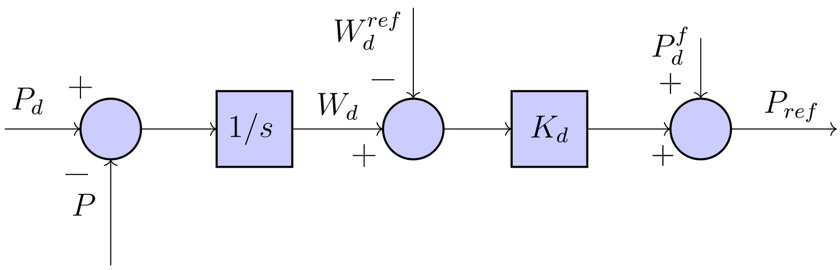


**Figure 4.3:** The DC-link control-scheme proposed in [23]. $P_d$ is the power from the MSC into the DC link, $P$ is the measured power at the PCC, $W_d$ is the energy in the DC-link capacitor, $W_d^{ref}$ is the reference DC-link energy, $K_d$ is the proportional gain, $P_d^f$ is $P_d$ possibly filtered and $P_{ref}$ is the reference power input for the PS-loop.

Since the converter losses are neglected the energy in the DC-link, $W_d$, can express the DC-link dynamics by,

$$\frac{dW_d}{dt} = P_d - P \tag{4.2}$$

where $P_d$ is the DC-source power from the machine side converter and $P$ is the measured power in the PCC. From (4.2) it is clear that the energy in the DC-link can be obtained by integration of the difference between $P_d$ and $P$. $W_d^{ref}$ is the reference energy stored in the DC-link capacitor and can be calculated as,

$$W_d^{ref} = \frac{c_{DC}}{2} \cdot v_{DC}^2 \tag{4.3}$$

where in [23] $v_{DC}$ is 2 $p.u$ and $c_{DC}$ is 2.1 mF. $F_d(s)$ is the transfer function of the DC-link controller and uses a weak integral function. When using the feed forward $P_d^f$ ($P_d$ possibly filtered), $F_d(s)$ can be approximated as a proportional controller with gain $K_d$. The recommendations specified in [23] defines the gain as $K_d = 0.18 \cdot \omega_{nom}$.

In [23], it is proposed that virtual inertia could be added to the PSC by replacing the proportional gain $K_p$ by a low-pass filter. However, it is stated that it is better to control inertia at the MSC rather than the GSC. The reason is that in order for a frequency control to work (change $P$), $P_d$ has to be changed, therefore it is better to control the inertia at the MSC. Furthermore, rapid change in $P_d$ with an inertial response of $P$ would lead to instability due to the design of the DC-link.

# 5

# Verification and testing of controller approach

In this chapter, the procedure of the verification of the converter controller, the additional testing of the controller that was conducted and the simulation-model is presented in-depth. The verification and additional tests were conducted in order to obtain the knowledge needed to conduct system studies of black start and off-grid operations.

## 5.1 Simulation model

The WT-model has been modelled with a simplified machine side properties to be a constant power source with a DC-link capacitor. This approach is sufficient since the machine side properties do not have a big effect on grid transients [57]. Furthermore the converter is modelled as a controllable AC-source and all transients, harmonics and losses from the switching are neglected. The converter model is seen in Figure 5.1

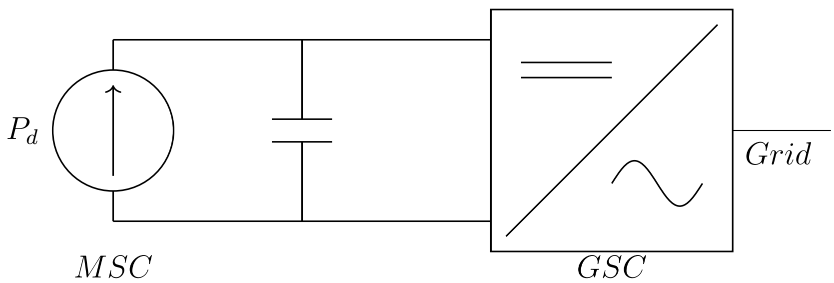


**Figure 5.1:** Converter model showing the MSC, DC-link and GSC with the assumption made of simplifying the MSC as a constant power source.

The three control-strategies mentioned in Chapter 4 are very similar in its principal behaviours. However, since the intended implementation of this controller were meant for a Type 4 WT grid-side converter, a control-strategy that could handle the energy in the DC-link capacitor was needed. Furthermore, since the controller will be tested in an off-grid setup, i.e a weak grid setup, the controller needs to be able to handle such operations. With this in mind, the PSC was chosen as the controller for investigation. The current controller was not implemented since the interest of the study was to analyse the transient behaviour of the PSC. The current controller would limit this and has been removed for better understanding of the capabilities of the PSC. Furthermore, the current controller is transparent during normal operations and therefore should not be critical to implement. The complete converter controller model in detail can be seen in Figure 5.2.

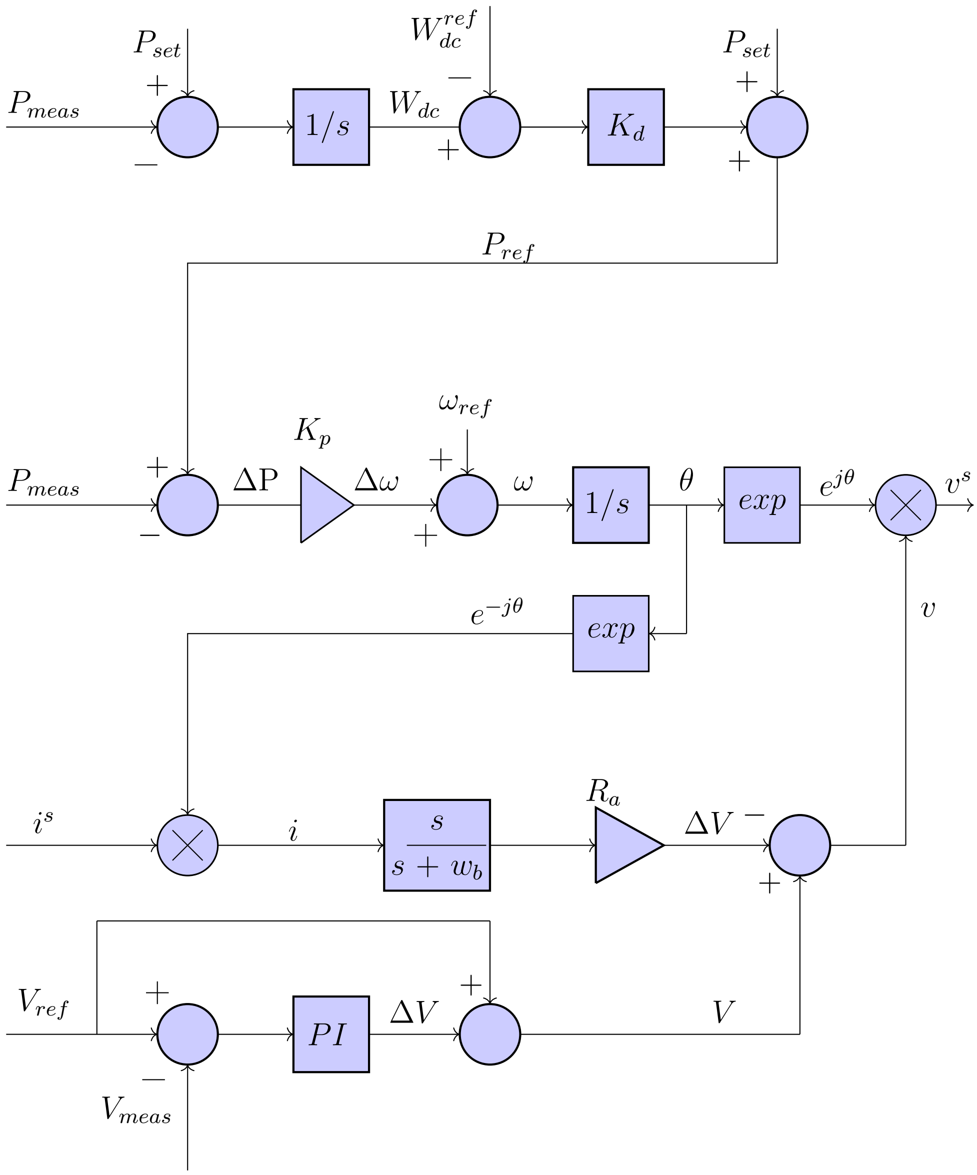


**Figure 5.2:** The complete converter controller model. $P_{set}$ is the power into the DC-link, $P_{meas}$ is the measured active power at the PCC, $\omega_{ref}$ is the nominal angular frequency, $V_{ref}$ is the voltage magnitude reference and $V_{meas}$ is the measured voltage magnitude at the PCC. All the other parameters is explained in section 4.4.

The converter controller was implemented in both Simulink for verification and additional testing and DIgSILENT PowerFactory for verification and system studies. It has been tested and its functionality verified based on [23] in four steps as can be seen in Appendix A. The base values used during the verification were the same as in [23] which can be seen in Table 5.1.

**Table 5.1:** Fixed values used in the simulation model as stated in [23].

| Parameter | Value | Unit |
|---|---|---|
| $S_{base}$ | 0.0127 | $[MVA]$ |
| $V_{base}$ | $\sqrt{\frac{2}{3}}\,0.4$ | $[kV]$ |
| $\omega_{base}$ | $2\pi 50$ | $[rad/s]$ |
| $V_{DC}$ | 0.650 | $[kV]$ |
| $C_{DC}$ | 2.1 | $[mF]$ |

The 1-phase representation of the test-grid is seen in Figure 5.3.

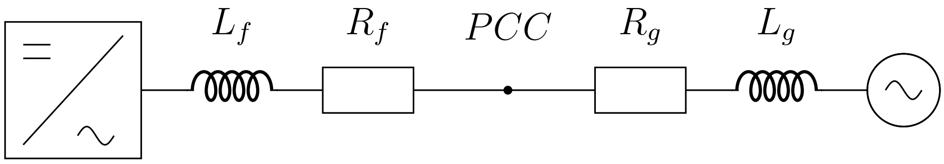


**Figure 5.3:** The 1-phase representation of the grid setup used during testing. $L_f/R_f$ is the filter impedances, PCC is the point of common coupling i.e the wind-turbine terminal and $L_g/R_g$ is the Thevenin equivalent grid impedances.

The step-response of the active power, voltage magnitude at the PCC and reactive power obtained in Simulink for the complete implementation of the PSC, as seen in Figure 5.2, is presented in the Chapter 9.1. The parameter-values used can be seen in Table 5.2.

**Table 5.2:** Parameter values used $K_p$, $R_a$, $K_d$, $K_p^{PI}$ and $K_i^{PI}$ in the Simulink controller-model for the full scale implementation .

| Parameter | Value used in Simulink |
|---|---|
| $K_p/R_a$ | 0.15 |
| $K_d$ | 0.18 |
| $K_p^{PI}$ | 0.2 |
| $K_i^{PI}$ | 10 |
| $SCR$ | 3 |

The Simulink model can be seen in Appendix E.2 and the implementation strategy seen below.

### 5.1.1 Modelling in Simulink

The additional tests in Simulink were conducted using the same base values as in the verification and as in [23], which is seen in Table 5.1. The converter controller has been tested in the simplified grid-setup (both in the verification and additional testing part), modelled as a Thevenin equivalent grid. The three phases have been explicitly modelled using controlled voltage sources and series RLC branches, which have been implemented as RL branch types (all found in the Simscape library). The grid impedances, $L_g$ and $R_g$, has been defined as,

$$L_g = \frac{\frac{3}{2} \cdot V_{base}^2}{S_{base} \cdot SCR \cdot \omega_{nom}} \tag{5.1}$$

and

$$R_g = x \cdot \omega_{nom} \cdot L_g, \tag{5.2}$$

where the $x$ is the resistive ratio, SCR is the short circuit ratio and can be varied to simulate different grid-strengths, $V_{base}$, $S_{base}$ and $\omega_{nom}$ can be found in Table 5.1. The resistive ratio has been set to 0.1 in all tests (except when different resistive ratios were tested). The filter impedance seen in Figure 5.3 has been set to $L_f = 0.15\%$ and $R_f = 0.015\%$.

To obtain full knowledge of every step, all transformations have been modelled block by block rather than using the pre-existing solutions in Simulink. The power measurement has been done by measuring the current and voltage (using the ideal measurement tools found in the Simscape package) at the PCC, then transforming these into $dq$-components. Using power invariant transformation the power can be calculated as shown in equation 3.21 and 3.22.

The Simulink model measures the angle in the PCC used for the Park transformations (of the voltage and current), using the approach described in section 3.6.3. The loop bandwidth has been selected as $\omega_{band} = 31.42[rad/s]$ which is below the point where it should affect the output according to [44]. Since this approach will make the measured angle lock the $q$-component of the voltage to zero the active power can be described as the product of the $d$-components of the current and voltage.

## 5.2 Additional testing of the converter controller

The stability and transient response of the converter controller have been further analysed in Simulink through some additional tests. The different tests were conducted using both the full PSC implementation and the simplified PSC controller without DC-link and voltage controller (as seen in Figure 4.2). The reason for some of the additional testing to be conducted in a simplified setup, was because in this setup the most stable controller is present without the added complexity of the DC-link controller. The additional tests that were conducted in this setup were conducted to gain knowledge of how parameters affected the controller and not if the parameters were feasible in a full-size test-setup.

The full PSC implementation was used to test different resistive ratios. The goal was to see how different ratios would affect a full-scale setup but since the voltage was of interest the voltage controller was disconnected. In order to control the voltage error, a droop controller has been tested instead of the previously used PI-controller as tested in Appendix A. The addition of virtual inertia has been tested both in the simplified setup, to test it with constant energy on the DC-side, and with the DC-link controller with the fixed amount of energy present in the DC-link setup. If not otherwise stated the steps in reference power, either in $P_{ref}$ (when using no DC-link controller) or $P_{set}$ (using DC-link controller) was conducted to both simulate a large load-pickup (0-1 $p.u$), simulate small steps (1-1.1 $p.u$ and 1.1-1.2 $p.u$) as well as to simulate a load shedding scenario (1.2-0.75 $p.u$).

### 5.2.1 Variation of gain and grid strength

Firstly the converter controller has been tested with various grid strengths in Simulink, using the simplified setup, to analyse how this will affect the transient behaviour. The grid strengths were changed by the SCR and with values of 2, 3, 5 and 10. During this test $K_p$ and $R_a$ were selected to 0.2 as stated in Chapter 4.4. Following this test different values of $K_p$ and $R_a$ have been tested in the same test-setup with an SCR of 3. $K_p$ and $R_a$ were varied between 0.05, 0.1, 0.15 and 0.2 and the response of the converter controller has been analysed.

### 5.2.2 Resistive ratio

During normal operations of a transmission line, the ratio between the resistive and inductive component can be approximated as 0.1. If a cable is used instead, which is typical for offshore conditions, this ratio is increased to levels close to 1. To simulate and test the converter controller's response to different locations of the WT, different ratios between $R_g$ and $L_g$ has been analysed in Simulink using the DC-link controller but without the voltage controller. However, the way the grid impedances has been defined the SCR will change depending on $R_g$, as can be seen in equation 5.3.

$$SCR = \frac{\frac{3}{2} \cdot V_{base}^2}{S_{base} \cdot \sqrt{(\omega_{nom} L_g)^2 + R_g^2}} \tag{5.3}$$

In order for the different scenarios to be comparable $L_g$ has been changed together with $R_g$ to keep the true SCR to 3 as seen in Table 5.3.

**Table 5.3:** Values of the grid impedances ($L_g$ and $R_g$) as well as corresponding SCR used for the different resistive ratios ($x$). $L_g$-ratio shows how much the inductive component has been modified compared to the original.

| $x$ | $R_g$ $[\Omega]$ | $L_g$ $[H]$ | $L_g$-ratio | SCR |
|---|---|---|---|---|
| 0 | 0 | 0.0134 | $1 \cdot L_g^{old}$ | 3.0000 |
| 0.3 | 1.2066 | 0.0128 | $0.9577 \cdot L_g^{old}$ | 3.0004 |
| 0.7 | 2.4076 | 0.0109 | $0.819 \cdot L_g^{old}$ | 3.0008 |
| 1 | 2.9690 | 0.0095 | $0.707 \cdot L_g^{old}$ | 3.0005 |

The parameter values used for the controller during the test is shown in Table 5.4.

**Table 5.4:** Parameter values used for $K_p$, $R_a$, the ideal control-loop bandwidth $K_d$ and SCR, in the controller model during the resistive ratio test.

| Parameter | Values used in Simulink |
|---|---|
| $K_p/R_a$ | 0.15 |
| $K_d$ | 0.18 |
| $SCR$ | 3 |

During this test the SCR-parameter has been held constant and set to 3, $K_p/R_a$ has been held constant at 0.15 and Kd has been set to 0.18. The converter active power-response for the different ratios was analysed for steps in $P_{set}$ from 0 to 1 $p.u$, 1 to 1.1 $p.u$, 1.1 to 1.2 $p.u$ and 1.2 to 0.75 $p.u$. The voltage magnitude at the PCC expressed in $dq$-form, as well as the voltage angle difference between the nominal angle and the angle measured at the PCC, has been analysed using the same setup but for a single step in $P_{set}$ from 0 to 1 $p.u$ to more easily show the steady-state deviation. The nominal angle has been obtained by integration of the nominal angular frequency ($\omega_{base}$).

### 5.2.3 Droop-controller

In actual installations, hard voltage-controllers as implemented in the verification are rarely used, therefore a gain-time droop controller has been tested instead which can be seen in Figure 5.4.

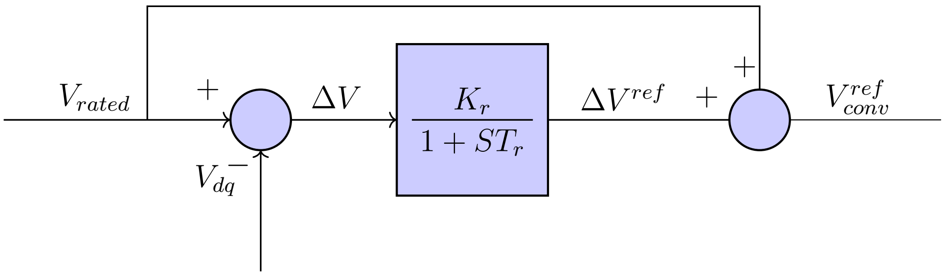


**Figure 5.4:** The time-gain droop based voltage controller used instead of the previously tested PI-controller. $V_{rated}$ is the rated line-line RMS voltage magnitude expressed in $p.u$, $V_{dq}$ is the measured voltage at the PCC represented in $dq$-form expressed in $p.u$, $K_r$ is the gain of the droop controller and is equivalent to $1/slope$, $T_r$ is the time constant and $V_{conv}^{ref}$ is the converter reference voltage magnitude.

The parameters used for the gain-time droop controller has been selected as K = 20 and T = 0.4 as suggested in [58], which corresponds to a slope of 5 %. The PSC parameters have been selected as in the verification of the full PSC, which is seen in Table 5.2. The voltage magnitude at the PCC expressed in $dq$-frame, as well as the reactive power measured at the PCC, has been analysed using the droop-controller. In this test, the steady-state deviation from nominal value was of interest and therefore the reference steps were reduced to one step in $P_{set}$ from 0 to 1 $p.u$.

### 5.2.4 Virtual inertia

Lastly, the PSC has been tested with a virtual inertia setup according to [23] by replacing the proportional gain $K_p$ with a low-pass filter described as,

$$\frac{1}{H \cdot s + D}, \tag{5.4}$$

where H is the inertial constant and D is the damping factor. The addition of virtual inertia has been tested both without the DC-link controller (constant energy), to verify its behaviour, and with it to see if it was a viable addition for implementation. The inertia constant in the low pass filter which adds the virtual inertia has been selected as $H = 2$ in the case of constant energy (which is in the range of typical values for synchronous machines [59]), to see if it could improve the behaviour of the converter in regards to frequency stability. In the full PSC implementation (including DC-link controller) $H = 0.1$ was used to visualise the conflict between the DC-link controller and the virtual inertia block. The damping factor, $D$, has been chosen as 39.48 based on [60] which made the transient magnitude to be close to the case when using $K_p$, i.e having no virtual inertia. In the case of constant energy the steps in $P_{ref}$ were: 0 to 1 $p.u$, 1 to 1.1 $p.u$, 1.1 to 1.2 $p.u$ and 1.2 to 0.75 $p.u$. In the full PSC implementation, the step in $P_{set}$ was chosen as 0 to 1 $p.u$ for easier visualisation of the oscillations that occurred. Both cases have been compared with the case of using the proportional gain (as previously verified).

# 6

# System study approach

The system studies include black start i.e energising transformers and transmission cable and off-grid operation. The simulations were conducted in DIgSILENT PowerFactory since this software is built for system studies, this was deemed as a better choice as a simulation tool. All the fixed values used in the system studies can be seen in Table 6.1.

**Table 6.1:** Fixed values used during the system studies, value of $C_{DC}$ were scaled according to $S_{base}$.

| Parameter | Value | Unit |
|---|---|---|
| $S_{base}$ | 4 | $[MVA]$ |
| $V_{base}$ | $\sqrt{\frac{2}{3}}\,0.4$ | $[kV]$ |
| $\omega_{base}$ | $2\pi 50$ | $[rad/s]$ |
| $V_{DC}$ | 0.650 | $[kV]$ |
| $C_{DC}$ | 661.4 | $[mF]$ |

## 6.1 Black start

To successfully black start a grid (energise transformers and transmission line) sufficient energy needs to be available. An assumption of having sufficient energy to maintain constant DC-link voltage has been made. The DC-link controller that controls the energy (that is assumed to be constant) will be present during black start but has been neglected during modelling since it will not interfere with the results if the energy is constant. Furthermore, energisation of the system is dependent on the converter controller to make the controller output voltage of 1 $p.u$ with a frequency of 50 Hz, i.e there is no need to calculate the voltage angle based on the difference between $P_{ref}$ and $P_{meas}$. Instead, a fixed angular frequency of 314 rad/s is assumed and therefore the converter controller during black start can be simplified as seen in Figure 6.1. The PI parameters of the voltage controller were set to the same values as in the full implementation of the PSC, i.e. $K_p^{PI}$=0.2 and $K_i^{PI}$=10.

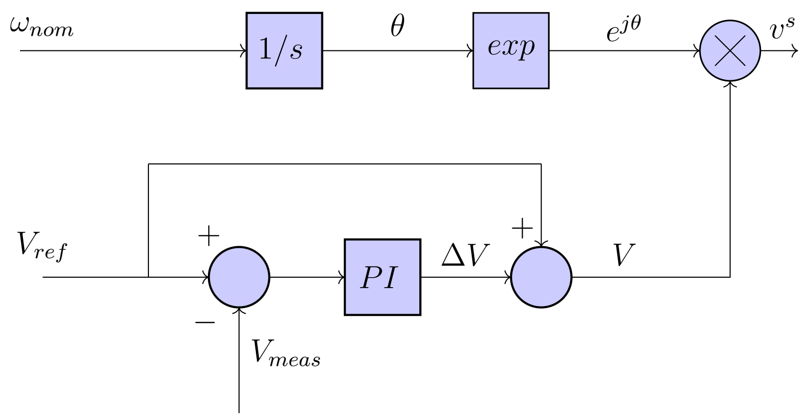


**Figure 6.1:** The proposed black start control, where $\omega_{nom}$ is the nominal angular frequency, $V$ is the output from the voltage controller and $v^s$ is the converter voltage reference represented in the stationary frame.

The test grid that was used during the black start is shown in Figure 6.2. The black start protocol consisted of 20 WTs placed in parallel which each one of them had a step-up transformer ($T_1$) connected to themselves and a single grid transformer ($T_2$) at the end. Between ($T_1$) and ($T_2$) a transmission cable was connected. The reason for having 20 WTs in parallel is to mimic a small-scale wind farm. The used cable was chosen from the predefined library in DIgSILENT PowerFactory and the settings used can be seen in Table 6.2.

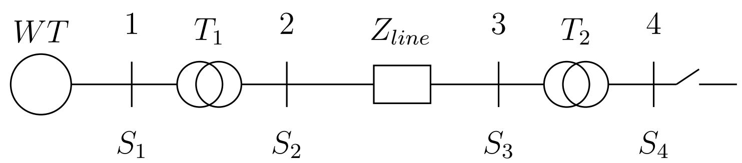


**Figure 6.2:** Test setup for black start and the different switches S1, S2, S3 and S4. The WTs had a rated power of 4 MVA and a power factor of 0.9 each and was placed in parallel to each other. A total of 20 WTs with 20 step-up transformers plus the single grid transformer was used. Terminal voltages can be found in Table 6.3.

**Table 6.2:** The cable settings used during simulation of black start. The name for the predfined cable in DIgSILENT Powerfactory was N2YSEY 3x120rm/16 6/10kV, that is constructed by Polyethene (PE) and uses a conductor construction that is round and has multi wires, i.e round conductor multi wire (RM).

| Core material & type | Length [km] | R [Ω/km] | $X_L$ [Ω/km] | B [uS/km] |
|---|---|---|---|---|
| Cu (3x120 rm) | 10 | 0.153 | 0.098991 | 103.6726 |

Two methods were used for energisation of the grid, soft and hard energisation. The methods were compared to each other with regards to inrush currents and voltages measured at the low voltage side of $T_1$, voltage fluctuations at the terminal connected to the WT as well as current output from the WT. The reason was to find which method that had the best characteristic and offered a procedure for energisation that could minimise transients and inrush currents. The black start model implemented in DIgSILENT PowerFactory is shown in Appendix C. The settings for the terminals and transformers are presented in tables 6.3 and 6.4.

**Table 6.3:** Terminal settings for terminal 1, 2, 3, 4 used for soft and hard energisation.

| Terminal | Nominal voltage [kV] |
|---|---|
| 1 | 0.4 |
| 2 | 10 |
| 3 | 10 |
| 4 | 110 |

**Table 6.4:** Transformer settings used for soft and hard energisation. $P_{Culoss}$ was chosen to be 1% of $S_{rated}$. $I_{Noload}$ and $P_{Noload}$ was chosen from personal experience.

| Transformer | T1 (ratings for a single step-up transformer) | T2 |
|---|---|---|
| $S_{Rated}$[MVA] | 4 | 80 |
| Rated voltage [kV] | 10/0.4 [HV/LV] | 110/10 [HV/LV] |
| $P_{Culoss}$ [kW] | 40 | 800 |
| $I_{Noload}$ [%] | 0.01 | 0.036 |
| $P_{Noload}$ [kW] | 15.75 | 0 |

All simulations were conducted in the EMT-simulation mode since this offers better analysis for transient events. In Table 6.5 each model used to measure a specific parameter are presented.

**Table 6.5:** Predefined models for measurements of current, voltage, frequency and power in DIgSILENT PowerFactory. All measurement tools have been set to "rated to connected element/terminal".

| Parameter | Model | Unit |
|---|---|---|
| I | StaImea | $p.u$ |
| V | StaVmea | $p.u$ |
| F | StaVmea | $p.u$ |
| P | StaPqmea | $p.u$ |

All measurement tools measured in quantities of three-phase and then transformed them into the stationary frame with the common unit of $p.u$.

### 6.1.1 Hard energisation

The hard energisation is done by closing the WT-switch, switch $S_1$ and $S_2$ in Figure 6.2 when the terminal voltage of the WT is 1 *p.u.* Switch $S_3$ is closed at all times and $S_4$ remains open during the entire simulation. To simulate this in DIgSILENT PowerFactory, the closing of switch S1 and S2 occurs at 0.015 s and at the same time, V is stepped from 0 to 1 *p.u* by setting the control block in the voltage controller that limits the rate of increase in the voltage to 100000 $p.u/s$. The complete simulation time was 11 s, so steady-state levels for currents and voltages were reached.

### 6.1.2 Soft energisation

The soft energisation is made by closing the switches $S_1$ and $S_2$ at 0.015 s, while $S_3$ is kept closed and $S_4$ is open in Figure 6.2 during the entire simulation. The voltage is then gradually increased from 0 to 1 *p.u.*

Soft energisation in DIgSILENT PowerFactory has been made possible through the implementation of a gradient limiter in the voltage control block that limits the rate of increase in the voltage to 0.1 $p.u/s$. Just as in the case with the hard energisation, the simulation time was 11 s with the purpose to reach steady-state levels.

## 6.2 Off-grid operation

In off-grid operations, the controller needs to be able to change its reference power according to the load demand which is different from the verification step where the power was adjusted according to the reference. This makes the converter controller as tested in the verification step not sufficient for off-grid purposes. In the controller setup from the verification part the DC-link controller is integrating the difference between $P_{meas}$ and $P_{set}$. If the load is changing, meaning $P_{meas}$ is changing, as in off-grid operations, the output of the DC-link controller, $P_{ref}$, will change rapidly. For this reason, another control-block has been implemented to control the reference power and the DC-link energy as seen in Figure 6.3.

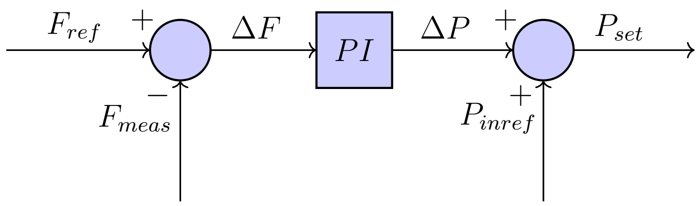


**Figure 6.3:** The added control-block needed in order for stable operation during off-grid operations. $F_{ref}$ is 50 Hz, $F_{meas}$ is the measured frequency at the PCC, The PI controller consists of a proportional and integral gain, $\Delta P$ is the additional power added to $P_{inref}$ (reference power into the DC-link) in order to obtain the new $P_{set}$ (power into the DC-link).

The frequency in the PCC was measured and compared to the reference frequency.

It was then passed through PI-controller with $K_p^{F_{cont}} = 10$ and $K_i^{F_{cont}} = 50$, which was chosen based on testing. The additional power $\Delta P$ was added to $P_{inref}$ (the reference power to the DC-link) in order to change $P_{set}$, i.e it acted as a hugely simplified pitch-controller to change the power-output from the MSC into the DC-link. Other parameters such as $K_p$, $R_a$, $K_d$, $K_p^{PI}$ and $K_i^{PI}$ were set to the values seen in Table 6.6 were all the used parameter-values are shown.

**Table 6.6:** Parameter values used $K_p$, $R_a$, $K_d$, $K_p^{PI}$, $K_i^{PI}$, $K_p^{F_{cont}}$ and $K_i^{F_{cont}}$ in the controller model during off-grid operation.

| Parameter | $K_p/R_a$ | $K_d$ | $K_p^{PI}$ | $K_i^{PI}$ | $K_p^{F_{cont}}$ | $K_i^{F_{cont}}$ |
|---|---|---|---|---|---|---|
| Value | 0.15 | 0.18 | 0.2 | 10 | 10 | 50 |

The off-grid operations test has been conducted in DIgSILENT PowerFactory by implementing the updated converter controller in an off-grid test-setup as seen in Figure 6.4, the terminal settings are listed in Table 6.7.

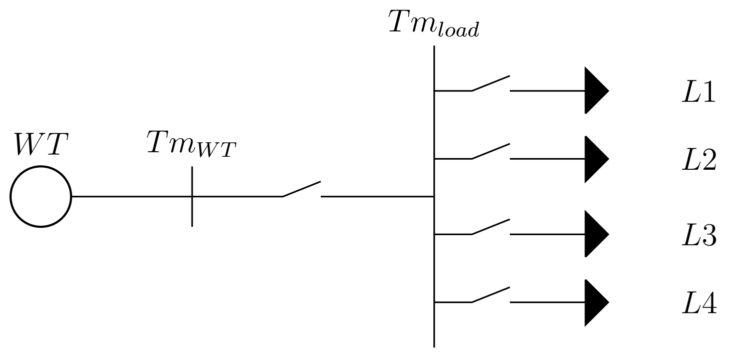


**Figure 6.4:** Test setup for off-grid operation showing the breaker between WT terminal ($Tm_{WT}$) and load terminal ($Tm_{load}$) as well as the loads used in different combinations.The WT had a rated power of 4 MVA and a power factor of 0.9. Load 1 (L1) was set to 0.75 $p.u$, load 2 (L2) was set to 0.25 $p.u$, load 3 (L3) was set to 0.1 $p.u$, load 4 (L4) was set to 0.1 $p.u$.

**Table 6.7:** Terminal settings for terminal $Tm_{WT}$ and $Tm_{load}$ used for off-grid operation.

| Terminal | Nominal voltage [kV] |
|---|---|
| $Tm_{WT}$ | 0.4 |
| $Tm_{load}$ | 0.4 |

The simulation was conducted in the EMT-simulation mode since this offers better analysis for transient events. Due to conducting the simulation as EMT, the loads were general loads modelled as constant impedance loads. The loads were switched on and off in different orders to simulate behaviours of different loading scenarios that could happen during off-grid operations. In Table 6.8, the rated power for each load is presented.

**Table 6.8:** Rated power for each load used during off-grid operation.

| Load | Rated power MW/$p.u$ |
|---|---|
| 1 | 3 / 0.75 |
| 2 | 1 / 0.25 |
| 3 | 0.4 / 0.1 |
| 4 | 0.4 / 0.1 |

The switching events used during the off-grid operation were the following; The switch between WT and load terminals were closed at 0.3 s, at 0.6 s $P_{inref}$ in the pitching controller was steeped from 0 to 1 and load 1 & 2 were switched on to obtain a loading of 1 $p.u.$ At 2.1 s and 3.6 s load 3 & 4 were switched on so the loading would be at 1.1 $p.u$ and 1.2 $p.u$ respectively. At 5.1 s, load 2, 3 & 4 were switched off to simulate a large load drop (from 1.2 $p.u$ to 0.75 $p.u$) that would mimic load shedding. During the simulation $P_{set}$, $P_{ref}$, $P$, the electric frequency, as well as the voltage on the WT terminal, were plotted to see how well the converter could handle events in off-grid operation. For the measurements of current, voltage, frequency and power, the same predefined models used for black start (seen in Table 6.5) were used for off-grid operation. The power, frequency and voltage response at $Tm_{WT}$ (seen in figure 6.4) are plotted to display the characteristics of the converter during off-grid operation.

# 7

# Testing and verification results

In this chapter, the results from the full implementation of the PSC in Simulink is presented as well as the results from the additional test conducted in Simulink.

## 7.1 Full implementation of the controller

The step-response of the active power using the full implementation of the PSC in Simulink, when steps in $P_{set}$ were applied from 0-1 $p.u$, 1-1.1 $p.u$, 1.1-1.2 $p.u$ and 1.2-0.75 $p.u$ can be seen in Figure 7.1. The voltage magnitude and reactive power measured at steady state for the first step in $P_{set}$ from 0-1 $p.u$ can be seen in Figure 7.2 (voltage magnitude) and Figure 7.3 (reactive power).

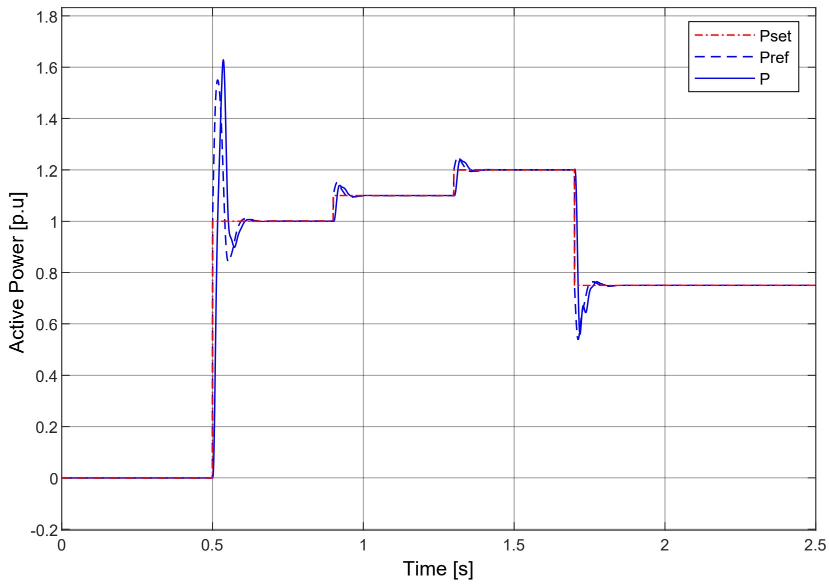


**Figure 7.1:** The step-response of the measured active power ($P$) and $P_{ref}$, when the power into the DC-link ($P_{set}$) was stepped from 0 to 1 $p.u$, from 1 to 1.1 $p.u$, from 1.1 to 1.2 $p.u$ and from 1.2 to 0.75 $p.u$, was obtained using the full PSC for $K_p/R_a$ = 0.15, $K_d$=0.18 and SCR =3

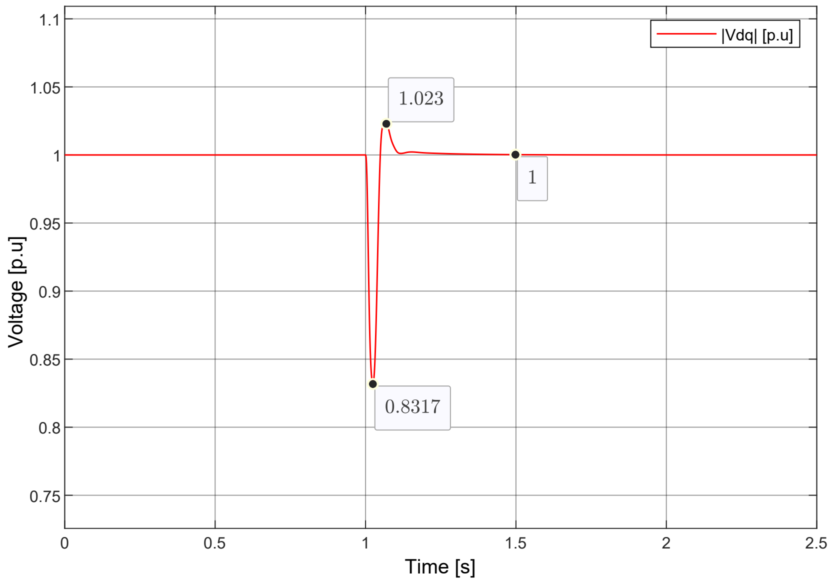


**Figure 7.2:** The voltage magnitude in $dq$-frame measured at the PCC. Obtained using the full PSC, when a step in $P_{set}$ (energy into the DC-link) from 0 to 1 $p.u$ were applied. $K_p/R_a$=0.15 and SCR=3 were used. The data tips shows the voltage magnitudes measured at the PCC during different times.

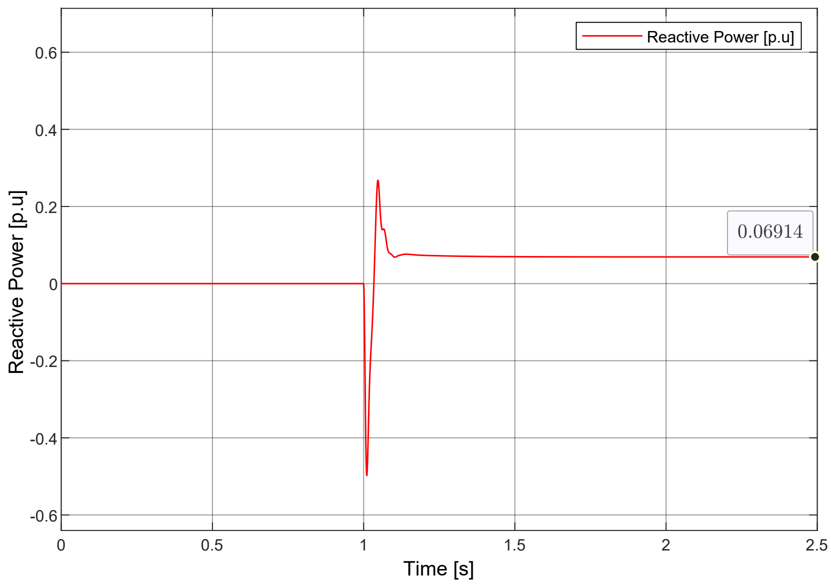


**Figure 7.3:** The reactive power measured at the PCC. Obtained using the full PSC, when a step in $P_{set}$ (energy into the DC-link) from 0 to 1 were applied. $K_p/R_a$=0.15 and SCR=3 were used. The data tips shows the reactive power measured at the PCC during different times.

In Figure 7.1 it is shown that the power step-response has overshoots for all steps. However for the large steps (load pick-up and load shedding) a large overshoot and undershoot occur. Especially problematic is the overshoot that occurs at t=0.5 $s$, since if the converter is only designed to operate up to 1.2 $p.u$ this will trip the converter and thereby trip the generation.

In Figure 7.2 it is seen that the voltage controller is working properly and ensures a steady-state voltage magnitude of 1 *p.u.* However, in Figure 7.3 it is seen that this requires some reactive power, meaning that (since Q is positive in steady-state) the voltage magnitude is increased with the voltage controller.

## 7.2 Additional testing of converter controller

### 7.2.1 Grid strengths

Using the simplified PSC setup (without DC-link controller or voltage controller) with $K_p/R_a$=0.2 the step-responses for different values of SCR were obtained in Simulink. The values used was SCR=2 (Figure 7.4), SCR=3 (Figure 7.5), SCR=5 (Figure 7.6) and SCR=10 (Figure 7.7).

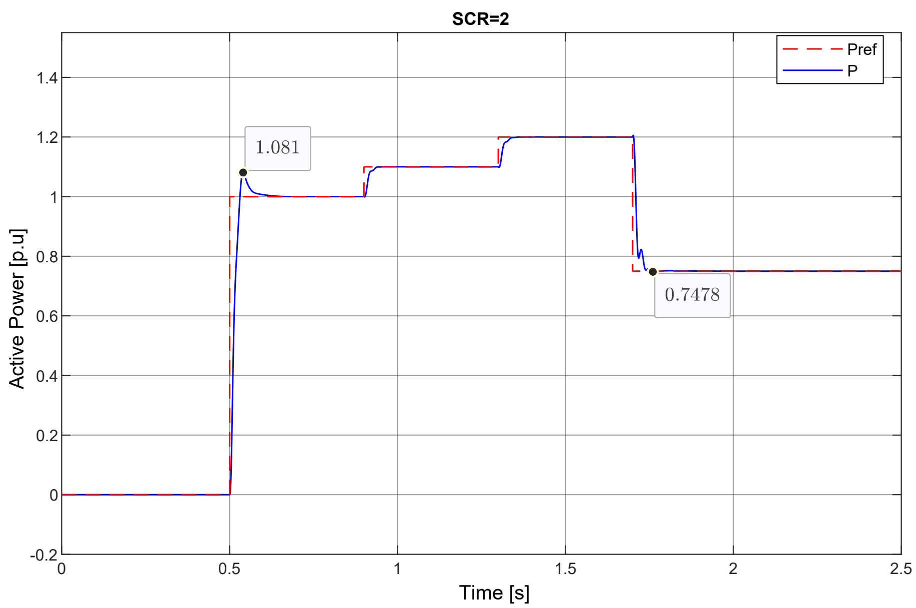


**Figure 7.4:** The active power response for steps in the reference power from 0 to 1 *p.u*, 1 to 1.1 *p.u*, 1.1 to 1.2 *p.u* and 1.2 to 0.75 *p.u* for a SCR=2 using the simplified test-setup with $K_p/R_a$=0.2. The data-tips shows the magnitude of of the active power.

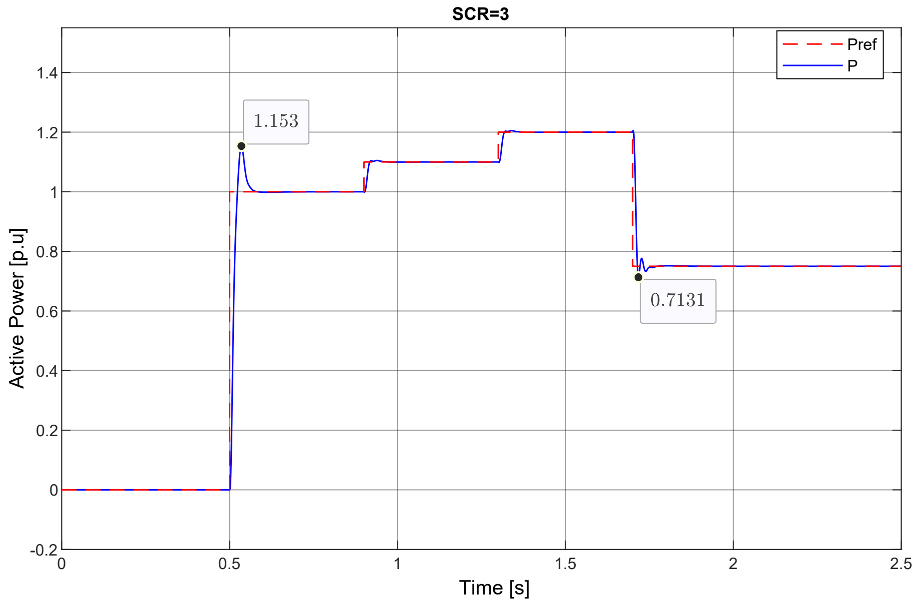


**Figure 7.5:** The active power response for steps in the reference power from 0 to 1 $p.u$, 1 to 1.1 $p.u$, 1.1 to 1.2 $p.u$ and 1.2 to 0.75 $p.u$ for a SCR=3 using the simplified test-setup with $K_p/R_a$=0.2. The data-tips shows the magnitude of of the active power.

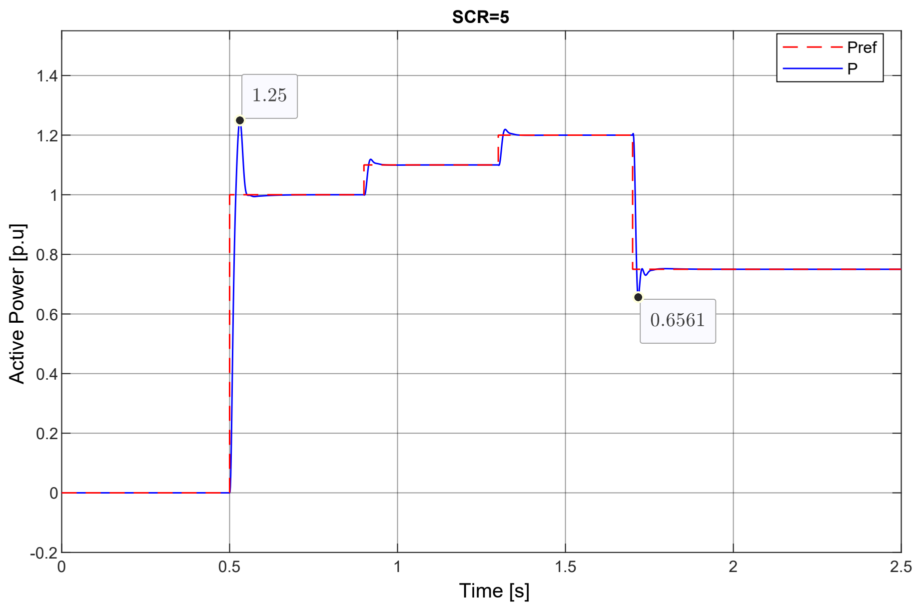


**Figure 7.6:** The active power response for steps in the reference power from 0 to 1 $p.u$, 1 to 1.1 $p.u$, 1.1 to 1.2 $p.u$ and 1.2 to 0.75 $p.u$ for a SCR=5 using the simplified test-setup with $K_p/R_a$=0.2. The data-tips shows the magnitude of of the active power.

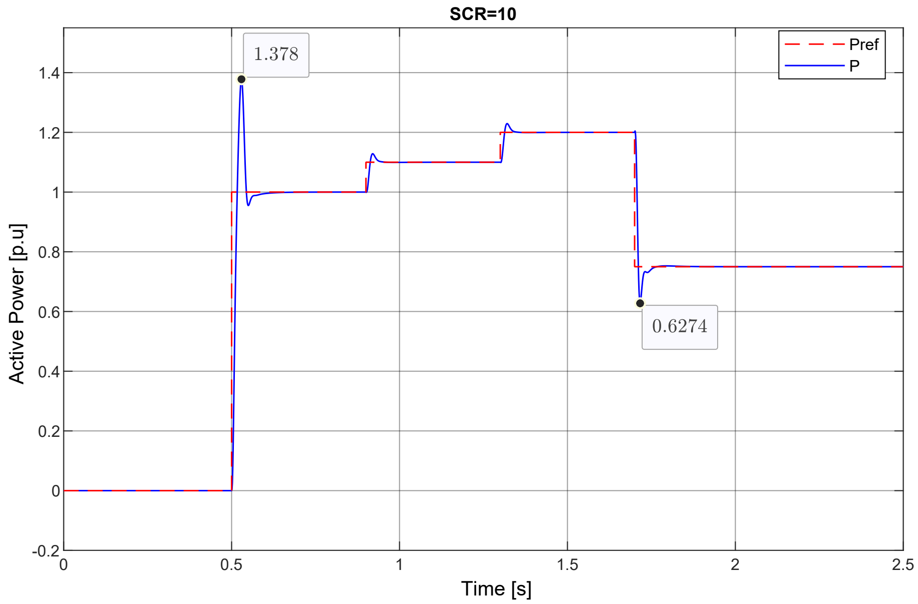


**Figure 7.7:** The active power response for steps in the reference power from 0 to 1 $p.u$, 1 to 1.1 $p.u$, 1.1 to 1.2 $p.u$ and 1.2 to 0.75 $p.u$ for a SCR=10 using the simplified test-setup with $K_p/R_a$=0.2. The data-tips shows the magnitude of of the active power.

In Figure 7.4-7.7 it is shown that a stronger grid leads to higher overshoots for the load pick-up at t=0.5 $s$ and lower undershoot for the load shedding at t=1.7 $s$. Again the overshoot can lead to tripping of the converter if it is not designed to handle such operations. If the converter is only designed to work for 1.2 $p.u$ (highest step) the converter will trip for SCR =5 (Figure 7.6) and SCR=10 (Figure 7.7).

### 7.2.2 Variation of gain

Using the PSC without the DC-link controller and voltage controller, with SCR=3 the step-responses for different values of $K_p$ and $R_a$ were obtained in Simulink. The values used was $K_p/R_a = 0.05$ (Figure 7.8), $K_p/R_a = 0.1$ (Figure 7.9), $K_p/R_a = 0.15$ (Figure 7.10) and $K_p/R_a = 0.2$ (Figure 7.11).

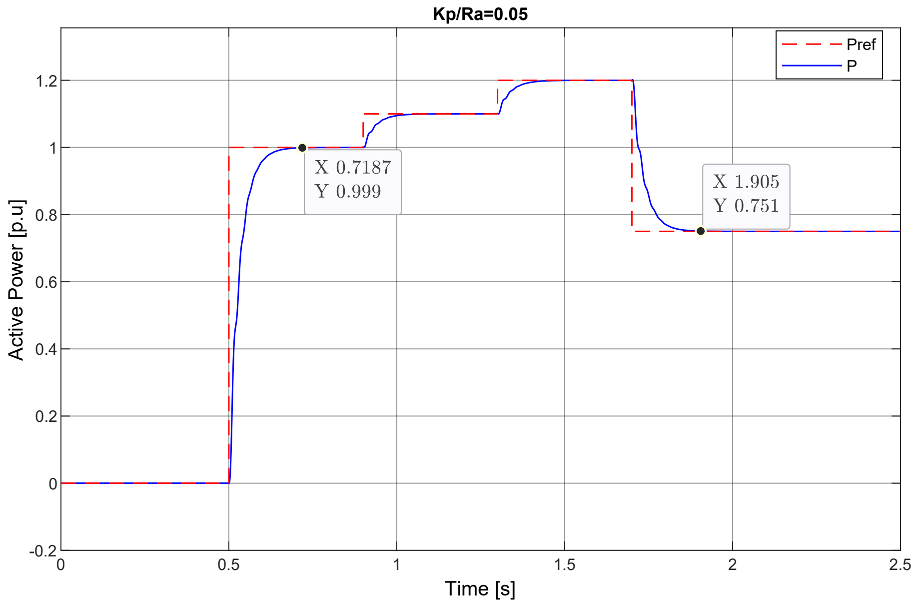


**Figure 7.8:** The active power response for steps in the reference power from 0 to 1 $p.u$, 1 to 1.1 $p.u$, 1.1 to 1.2 $p.u$ and 1.2 to 0.75 $p.u$ for a $K_p/R_a$=0.05 using the simplified test-setup with SCR=3. The data-tips shows the magnitude of of the active power (Y) and the corresponding time (X).

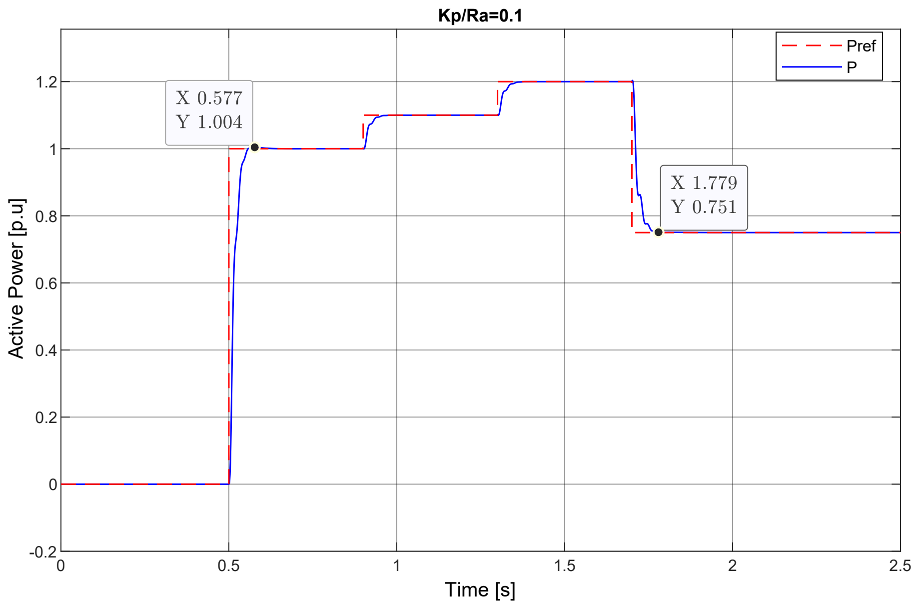


**Figure 7.9:** The active power response for steps in the reference power from 0 to 1 $p.u$, 1 to 1.1 $p.u$, 1.1 to 1.2 $p.u$ and 1.2 to 0.75 $p.u$ for a $K_p/R_a$=0.1 using the simplified test-setup with SCR=3. The data-tips shows the magnitude of of the active power (Y) and the corresponding time (X).

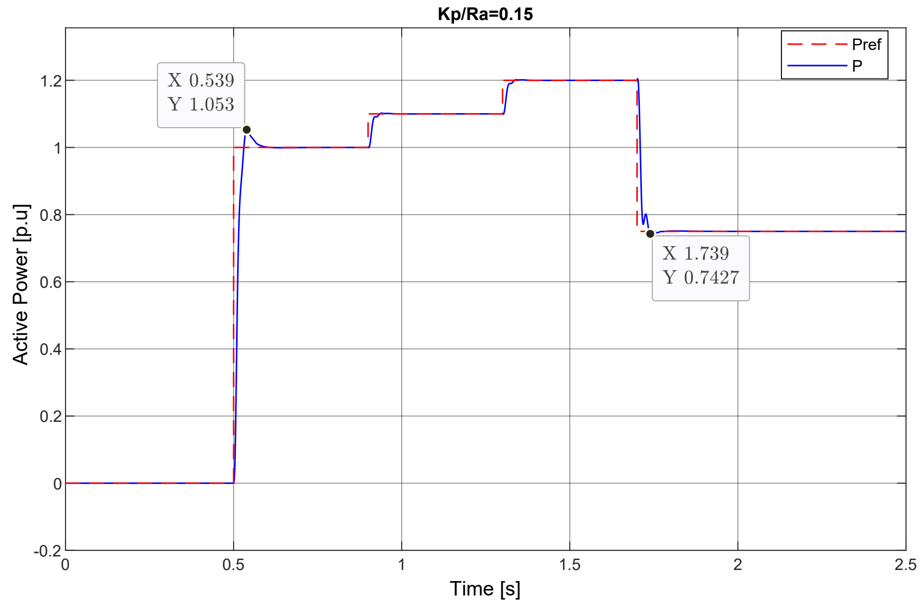


**Figure 7.10:** The active power response for steps in the reference power from 0 to 1 $p.u$, 1 to 1.1 $p.u$, 1.1 to 1.2 $p.u$ and 1.2 to 0.75 $p.u$ for a $K_p/R_a$=0.15 using the simplified test-setup with SCR=3. The data-tips shows the magnitude of of the active power (Y) and the corresponding time (X).

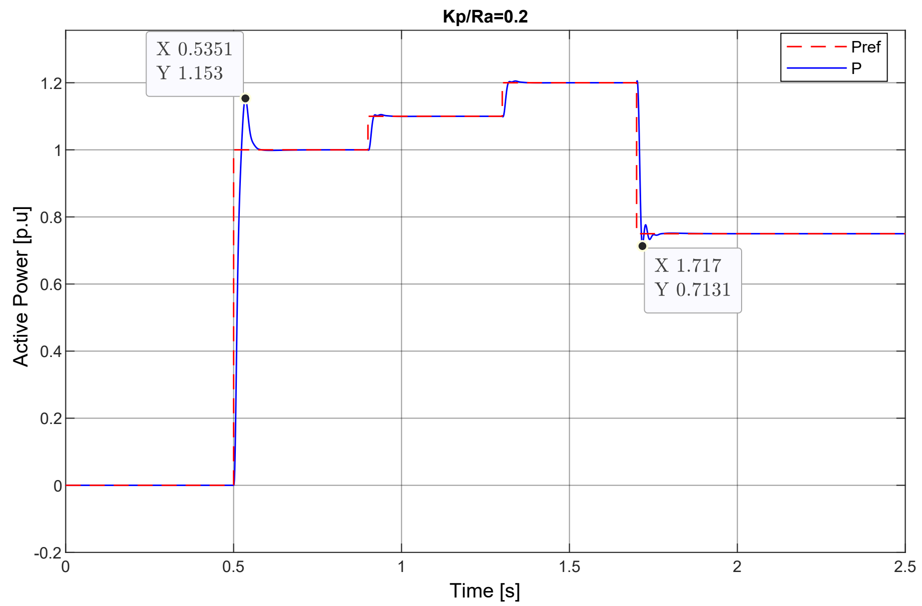


**Figure 7.11:** The active power response for steps in the reference power from 0 to 1 $p.u$, 1 to 1.1 $p.u$, 1.1 to 1.2 $p.u$ and 1.2 to 0.75 $p.u$ for a $K_p/R_a$=0.2 using the simplified test-setup with SCR=3. The data-tips shows the magnitude of of the active power (Y) and the corresponding time (X).

In Figure 7.8-7.11 it is shown that the parameter selection of the gains affects both the speed of the controller and the behaviour of the step-response. Lower parameter selection leads to lower overshoot/undershoot. The results show that the selection of $K_p/R_a$ could help improve the overshoot problem that was obtained in the previous tests (the full implementation and high grid-strength). However, this is at the cost of a slower step-response which might not be compatible with the DC-link controller.

### 7.2.3 Resistive ratio

Using the PSC with DC-link controller but without voltage controller, with $K_p/R_a$ = 0.15 and SCR=3 (with $L_g$ modified to keep SCR =3 for all cases) the step-response using different resistive ratios were obtained when steps in $P_{set}$ (power into the DC-link) were applied. The ratios used was 0 (Figure 7.12), 0.3 (Figure 7.13), 0.7 (Figure 7.14) and 1 (Figure 7.15).

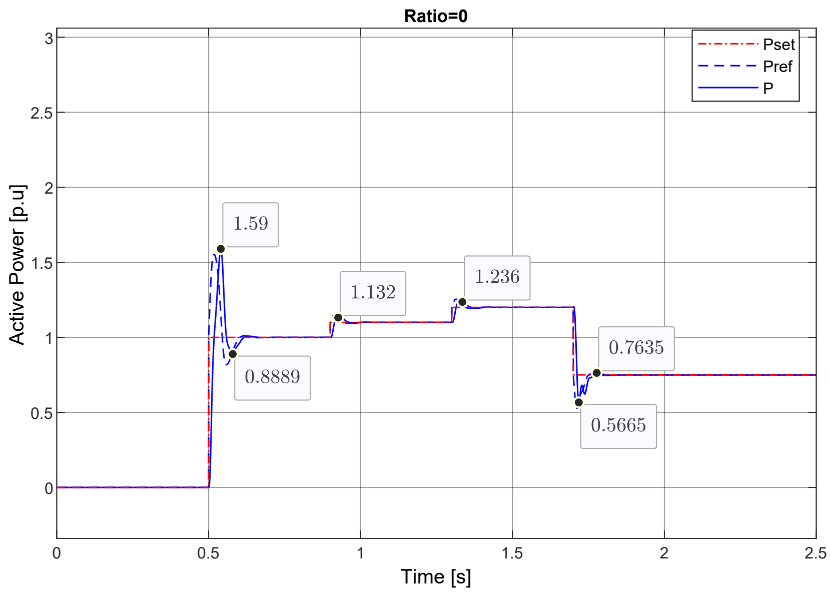


**Figure 7.12:** The active power and the reference power response for steps in $P_{set}$ from 0 to 1 $p.u$, 1 to 1.1 $p.u$, 1.1 to 1.2 $p.u$ and 1.2 to 0.75 $p.u$ for the resistive ratio = 0 using the full PSC setup but without voltage controller ($K_p/R_a$=0.15, $K_d$ = 0.18 and SCR=3). The data-tips shows the magnitude of of the active power.

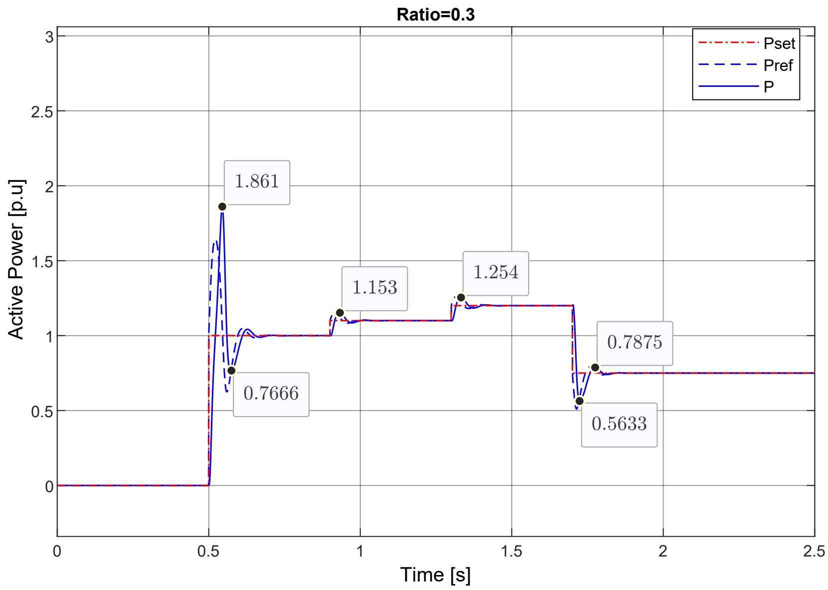


**Figure 7.13:** The active power and the reference power response for steps in $P_{set}$ from 0 to 1 $p.u$, 1 to 1.1 $p.u$, 1.1 to 1.2 $p.u$ and 1.2 to 0.75 $p.u$ for the resistive ratio = 0.3 using the full PSC setup but without voltage controller ($K_p/R_a$=0.15, $K_d$ = 0.18 and SCR=3). The data-tips shows the magnitude of of the active power.

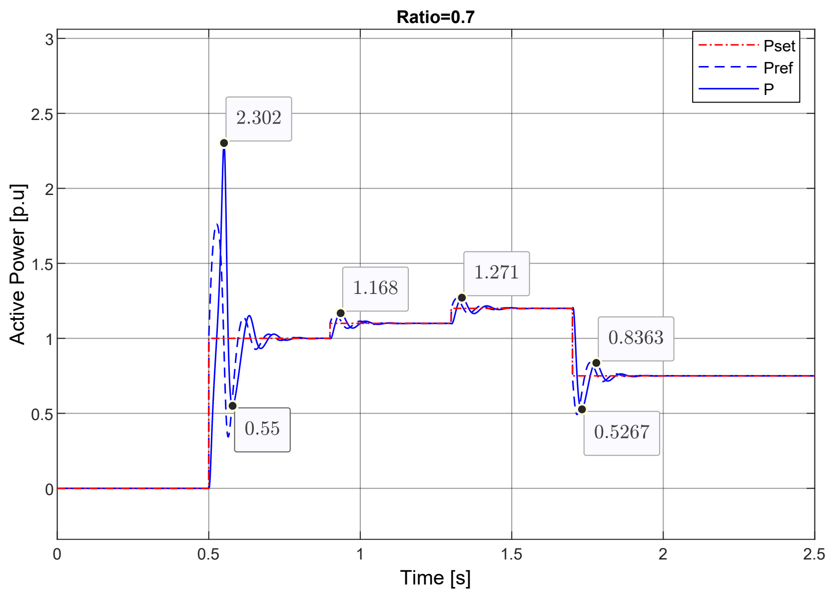


**Figure 7.14:** The active power and the reference power response for steps in $P_{set}$ from 0 to 1 $p.u$, 1 to 1.1 $p.u$, 1.1 to 1.2 $p.u$ and 1.2 to 0.75 $p.u$ for the resistive ratio = 0.7 using the full PSC setup but without voltage controller ($K_p/R_a$=0.15, $K_d$ = 0.18 and SCR=3). The data-tips shows the magnitude of of the active power.

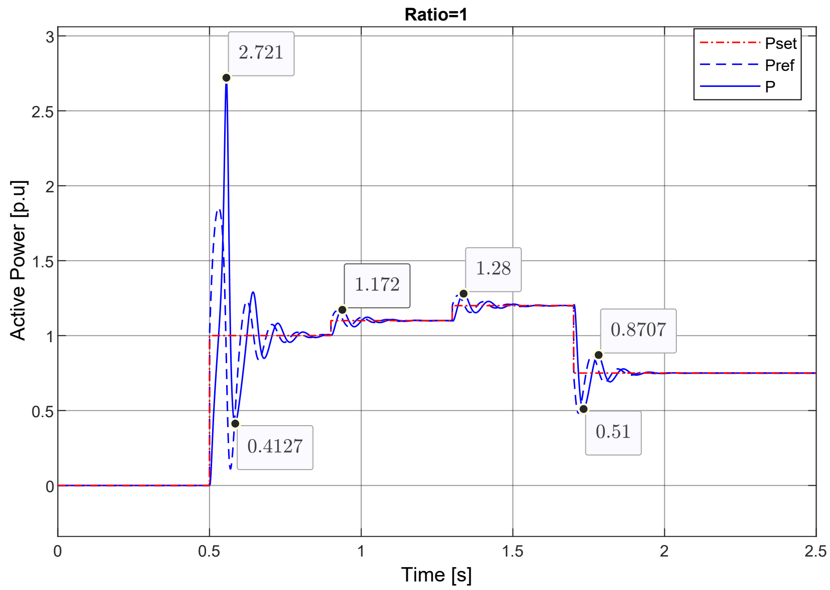


**Figure 7.15:** The active power and the reference power response for steps in $P_{set}$ from 0 to 1 $p.u$, 1 to 1.1 $p.u$, 1.1 to 1.2 $p.u$ and 1.2 to 0.75 $p.u$ for the resistive ratio = 1 using the full PSC setup but without voltage controller ($K_p/R_a$=0.15, $K_d$ = 0.18 and SCR=3). The data-tips shows the magnitude of of the active power.

The voltage magnitude measured at the PCC is affected by the increasing ratio as shown in Figure 7.16.

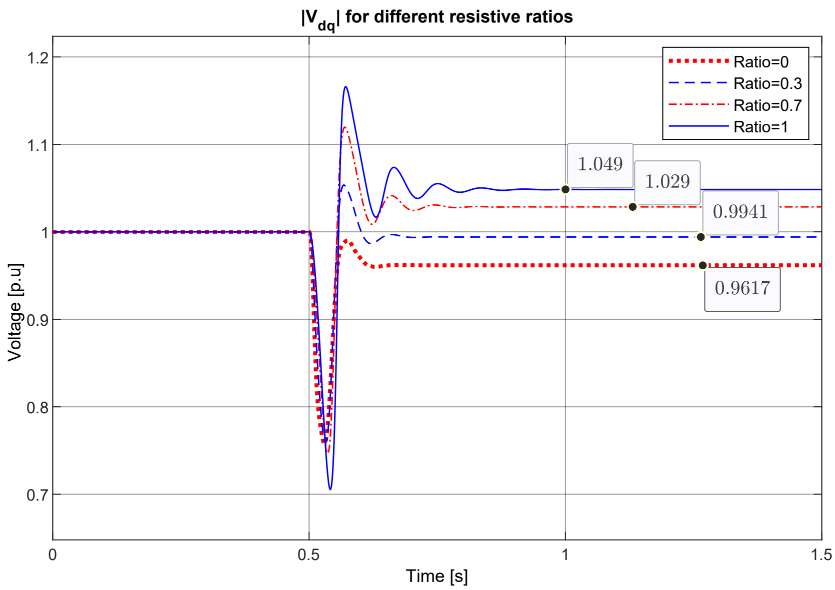


**Figure 7.16:** Magnitude of the $dq$ voltage measured at the PCC for different resistive ratios (0, 0.3, 0.7 and 1), for a step in $P_{set}$ from 0 to 1 $p.u$ at t = 0.5 $s$. The data-tips shows the magnitude at steady-state. Note that even though they are represented in different times they are all showing steady-state values.

The voltage angle at the PCC is affected as well by the increasing ratio (especially during the transient event) as shown in Figure 7.17, where the difference between the nominal angle and the angle measured at the PCC is shown.

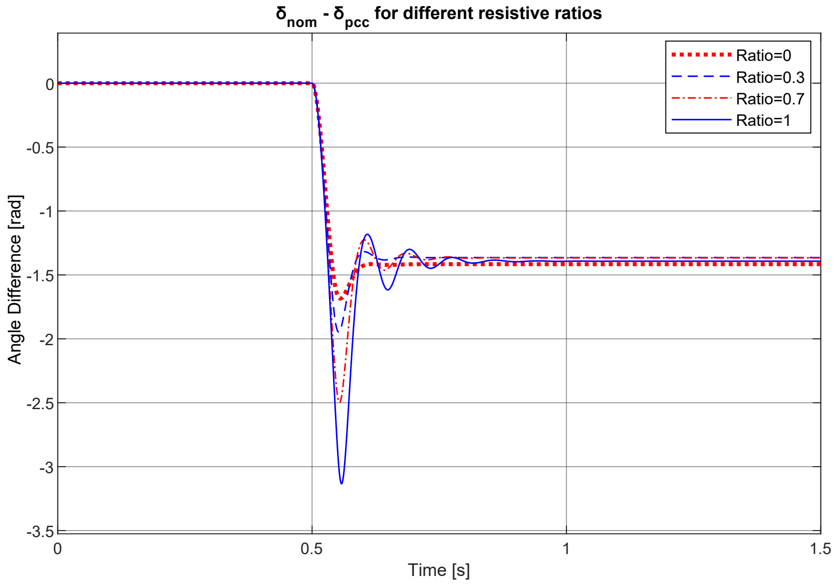


**Figure 7.17:** Voltage angle difference between the nominal angle and the measured angle at the PCC for different resistive ratios (0, 0.3, 0.7 and 1), for a step in $P_{set}$ from 0 to 1 $p.u$ at t = 0.5 $s$.

In Figure 7.12-7.15 it is shown that a higher resistive ratio in the grid leads to higher transients and oscillations. If the converter is designed to only handle 1.2 $p.u$ in power magnitude then it will trip for all ratios during the load pick-up at t=0.5 $s$. For the case of resistive ratio = 0.7, the magnitude of the highest transient is $\sim$ 230% higher than the wanted operation and for the case of resistive ratio = 1, it is $\sim$ 272% higher. These overshoots will most definitely trip the converter.

### 7.2.4 Droop controller

Using a gain-time based droop controller the voltage can be allowed to differ from the nominal value which is seen in Figure 7.18. Consequently, this leads to a smaller reactive current being drawn from the converter as can be seen in Figure 7.19 if compared to the PI-controller (Figure 7.3).

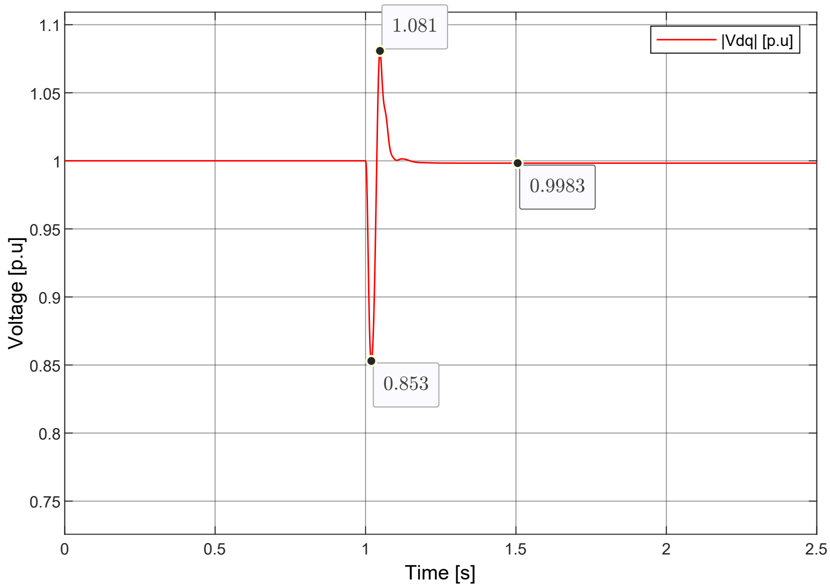


**Figure 7.18:** The voltage magnitude in $dq$-frame measured at the PCC when using a droop-based voltage controller for a step in $P_{set}$ from 0 to 1 $p.u$ at t = 1s. The data-tips shows the magnitude of the voltage at different instances.

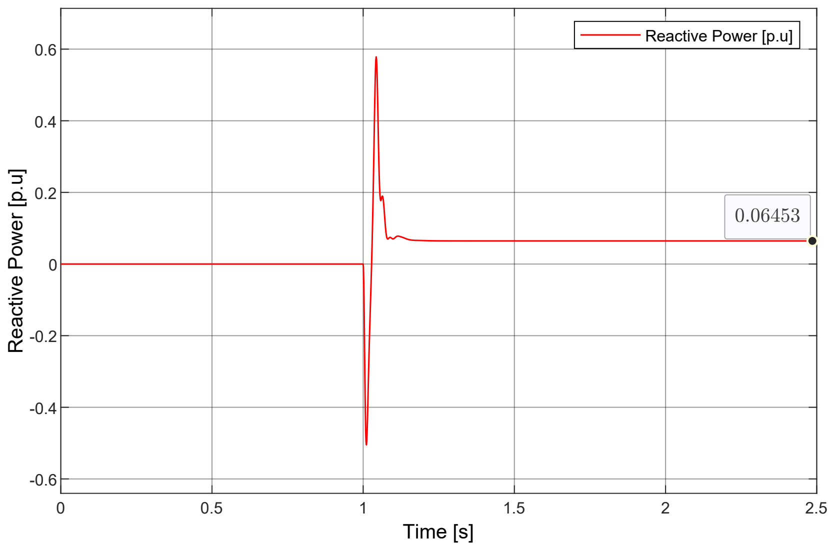


**Figure 7.19:** The reactive power measured at the PCC when using a droop-based voltage controller for a step in $P_{set}$ from 0 to 1 $p.u$ at t = 1s. The data-tip shows the magnitude of the reactive power at steady state.

The droop controller allows for the voltage magnitude to differ slightly from the nominal value (in this case with a slope of 5%). In Figure 7.18 it is seen that the voltage magnitude differs by 0.17% from 1 $p.u.$ This small change in voltage magnitude leads to a decrease in reactive power (as seen in Figure 7.19) by almost 6.7% compared to using the PI-controller in Figure 7.3.

### 7.2.5 Virtual inertia

In Figure 7.20 the active power response both for the previous case of using $K_p$ and the case with the addition of virtual inertia ($H = 2$ and $D = 39.48$), using simplified PSC without DC-link controller, with steps in $P_{ref}$ from 0 to 1 $p.u$, 1 to 1.1 $p.u$, 1.1 to 1.2 $p.u$ and 1.2 to 0.75 $p.u$, $K_P/R_a$= 0.2 and SCR =3, is shown. In Figure 7.21 the corresponding frequency behaviour is shown.

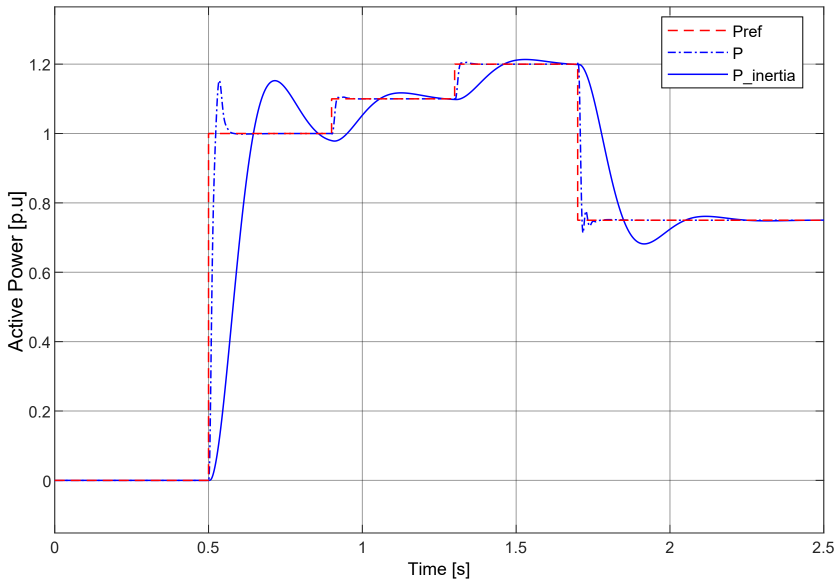


**Figure 7.20:** The active power response tested without DC-link controller (constant energy) using a virtual inertia setup ($P_{inertia}$) and using the previously tested setup ($P$) for steps in the reference power ($P_{ref}$) from 0 to 1 $p.u$, 1 to 1.1 $p.u$, 1.1 to 1.2 $p.u$ and 1.2 to 0.75 $p.u.$

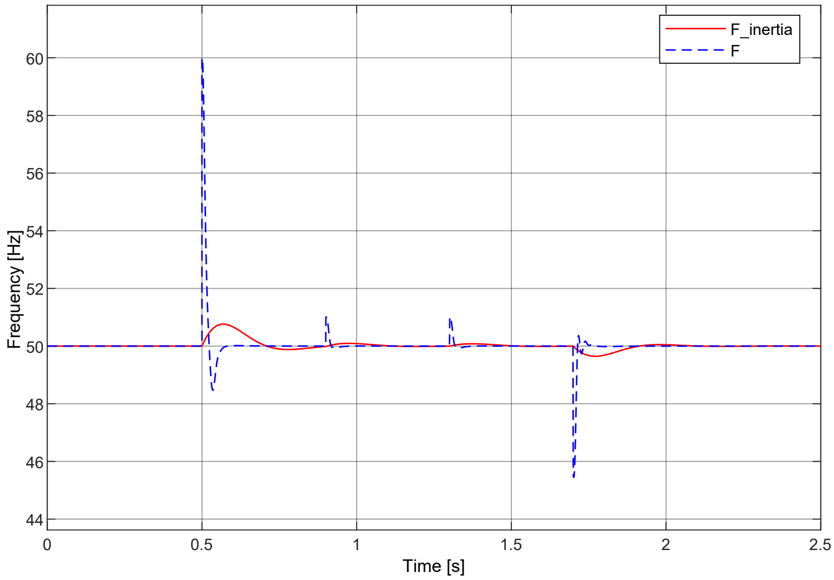


**Figure 7.21:** The frequency response tested without DC-link controller (constant energy) using a virtual inertia setup ($F_{inertia}$) and using the previously tested setup ($F$) for steps in the reference power ($P_{ref}$) from 0 to 1 $p.u$ (at t=0.5 s), 1 to 1.1 $p.u$ (at t=0.9 s), 1.1 to 1.2 $p.u$ (at t=0.1.3 s) and 1.2 to 0.75 $p.u$ (at t=1.7 s).

The results seen in Figure 7.20 and 7.21, presents the behaviour with virtual inertia where no DC-link controller is used compared to the case of no virtual inertia. The big difference to power response when introducing virtual inertia is that the response is much slower, the overshoots in power is noticeable delayed compared to the case without inertia, the overshoots is also present during a longer time period before reaching steady state. However, the frequency response shows a better dynamic performance, the frequency spikes that is present without virtual inertia at 0.5 s and 1.7 s is now smoothed because of the decreased RoCoF that is offered with virtual inertia.

In Figure 7.22 the active power response both for the previous case of using $K_p$ and the case with the addition of virtual inertia ($H$ = 0.1 and $D$ = 39.48), using the PSC with the DC-link controller, with a step in $P_{set}$ from 0 to 1 $p.u$, $K_P/R_a$= 0.15 and SCR =3, is shown. In Figure 7.23 the corresponding frequency behaviour is shown.

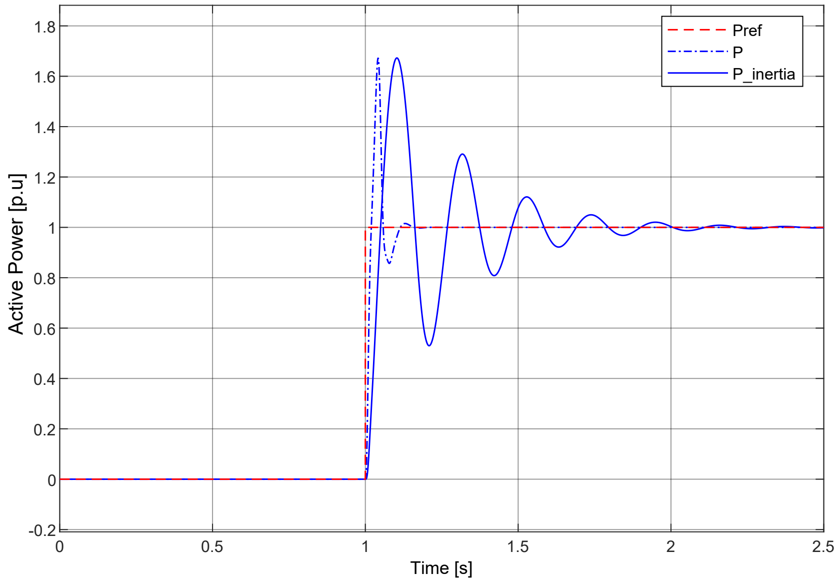


**Figure 7.22:** The active power response tested with DC-link controller using a virtual inertia setup ($P_{inertia}$) and using the previously tested setup ($P$) for a step in the reference power to the DC-link ($P_{set}$) from 0 to 1 $p.u$.

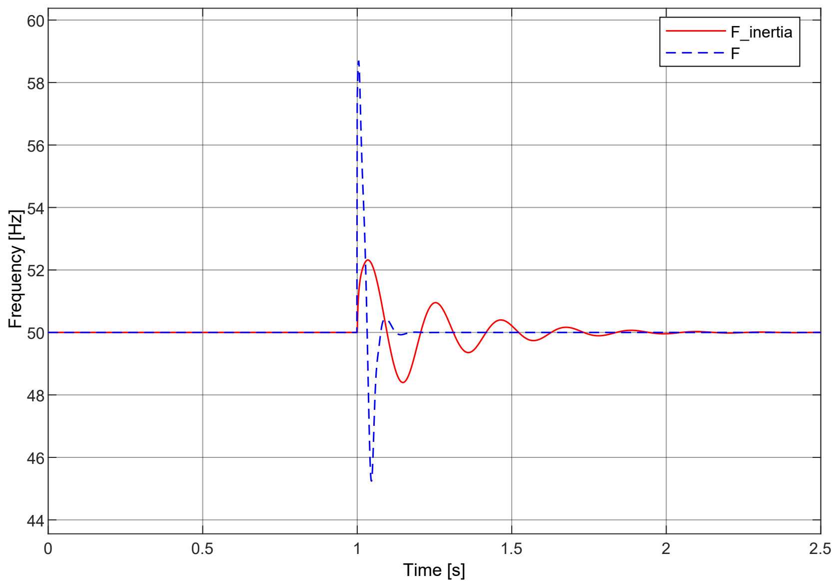


**Figure 7.23:** The frequency response tested with DC-link controller using a virtual inertia setup ($F_{inertia}$) and using the previously tested setup ($F$) for a step in the reference power to the DC-link ($P_{set}$) from 0 to 1 $p.u$ (at t=1s).

The results seen in Figure 7.22 and 7.23, presents the behaviour with virtual inertia when the DC-link controller is used. Now the power response is worse with virtual inertia implemented (even for a very small inertia constant of H=0.1), a lot of oscillations are present and the magnitude of the initial transient is not decreased in magnitude. The same behaviour is seen for the frequency response but with a much lower transient peak at the initial step in power compared to when not having virtual inertia, but still arguably higher when compared to the case without DC-link control. This response is not desired since it could lead to system instability problems.

# 8

# System study results

## 8.1 Black start

For black start operation two different methods were used for energisation, the soft- and hard energisation, in this Chapter the results from these tests are presented.

### 8.1.1 Hard energisation

The obtained currents from the hard energisation method are presented in Figure 8.1.

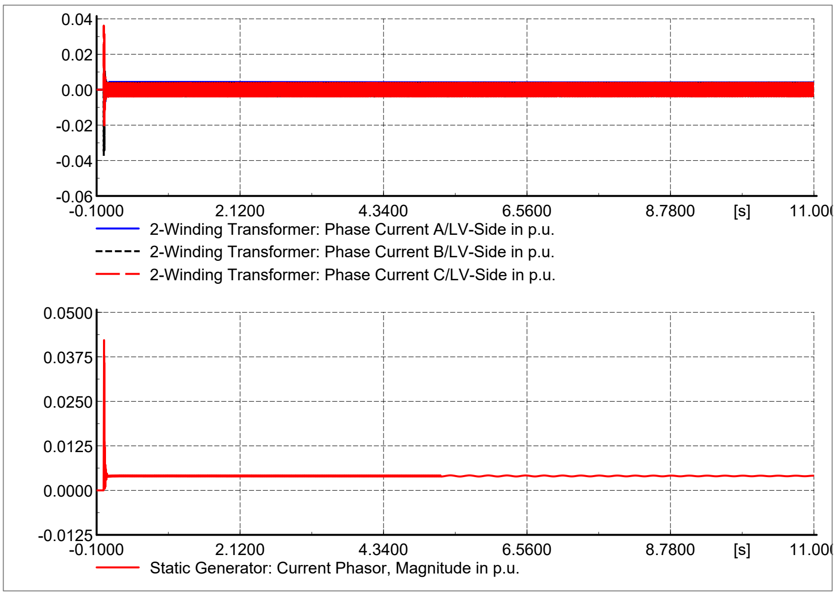


**Figure 8.1:** Currents during black start with hard energisation protocol. At t=0.015 s the switches to $T_1$ and cable are closed, while $V_{ref}$ is stepped to 1 $p.u.$

In Figure 8.2, the same plots are shown but with a zoomed view to display the waveforms and events during the first moments of energisation.

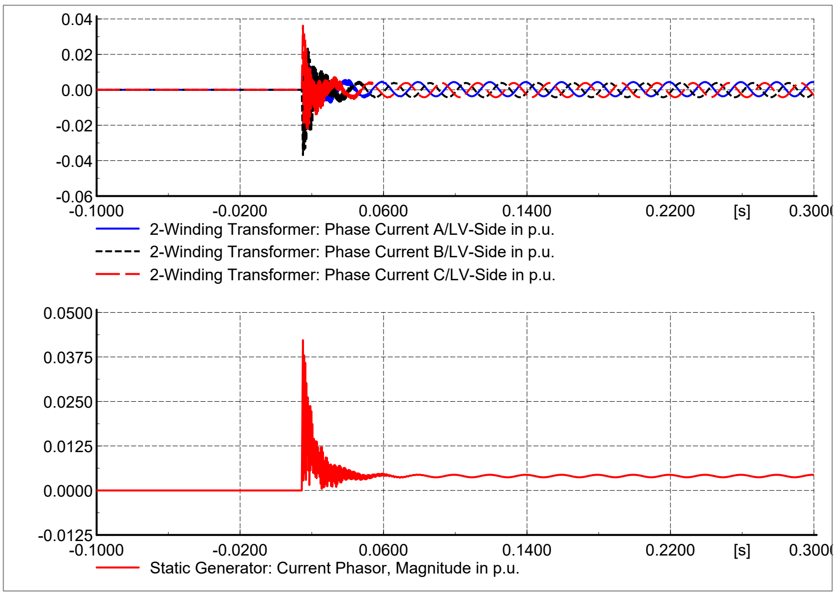


**Figure 8.2:** Zoomed in view of the currents during black start with hard energisation protocol. At t=0.015 s the switches to $T_1$ and cable are closed, while $V_{ref}$ is stepped to 1 $p.u.$

In Figure 8.3, the obtained voltage profile from the LV-side of $T_1$ is shown as well as the voltage profile at the $Tm_{wt}$.

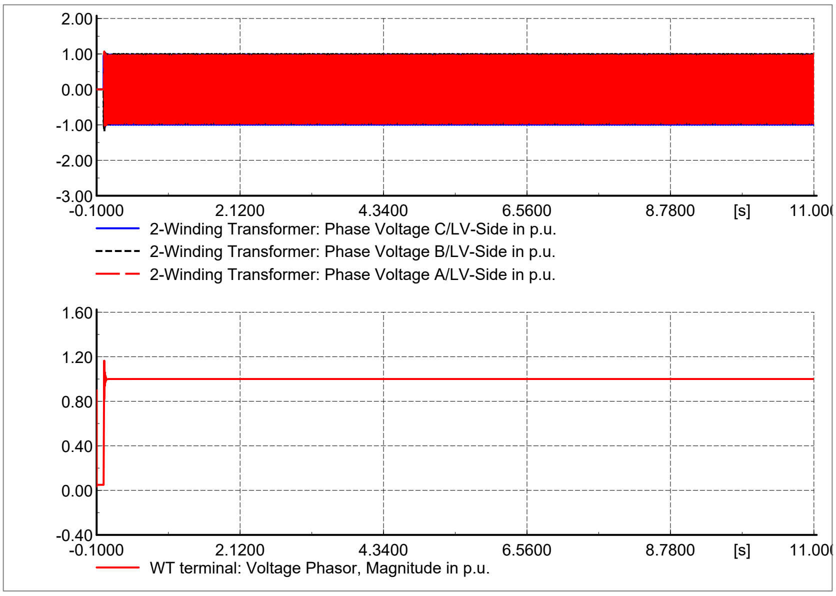


**Figure 8.3:** Voltages during blackstart with hard energisation protocol. At t=0.015 s the switches to $T_1$ and cable are closed, while $V_{ref}$ is stepped to 1.0 $p.u$

In Figure 8.4, the same plots are shown but with a zoomed view to better display the waveforms and events during the first moments of energisation.

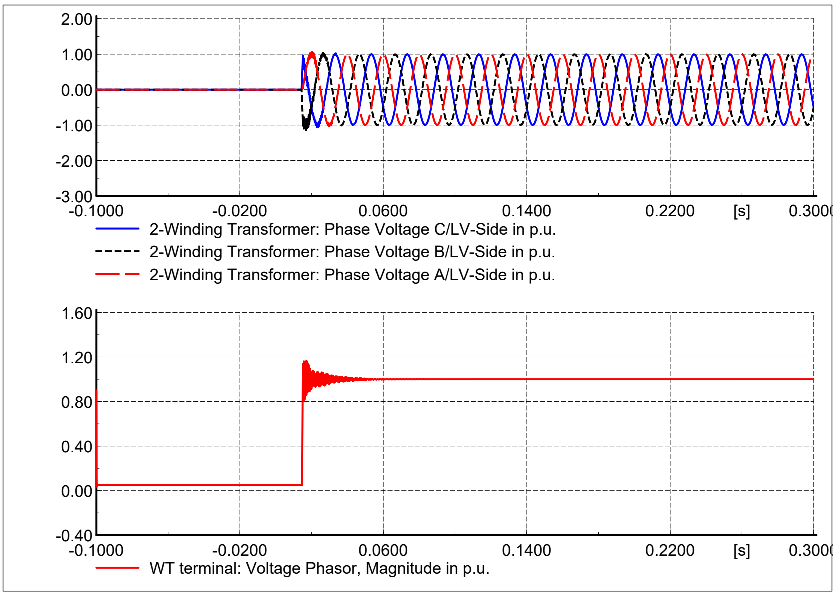


**Figure 8.4:** Zoomed in view of the voltages during black start with hard energisation protocol. At t=0.015 s the switches to $T_1$ and cable are closed, while $V_{ref}$ is stepped to 1 $p.u$

From Figures 8.1 and 8.1, it is seen that there are fast transients at the beginning of the energisation process for the inrush current flowing into the transformers located at $T_1$, as well as for the current that is sent out from each wind turbine. The steady-state is reached in a short amount of time. However, the fast transients can be a problem for the converters and transformers, since they can damage the equipment, if not rated properly. The magnitude of the transients may not be the danger in this specific case, but rather the speed of them.

From Figures 8.3 and 8.4, it is seen that there is a slight overshoot in voltage at the WT terminal and transformers $T_1$ during the beginning of the energisation process. The overshoot reaches almost 1.2 p.u, which can cause problems if the converters and transformers are not rated to handle these kinds of magnitudes. Once again, the steady-state is reached in a short amount of time.

### 8.1.2 Soft energisation

The obtained currents from the soft energisation method are presented in Figure 8.5.

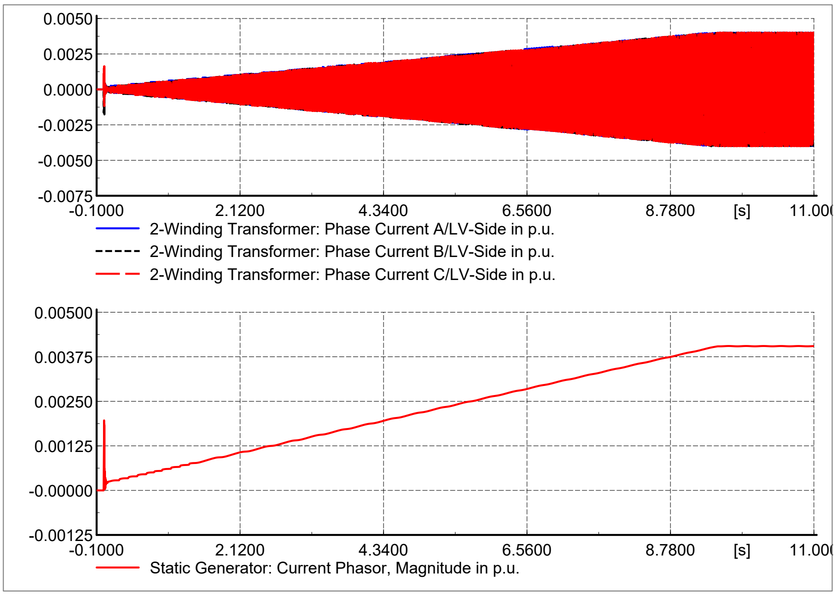


**Figure 8.5:** Currents during blackstart with soft energisation protocol. At t=0.015 s the switches to $T_1$ and cable are closed, while $V_{ref}$ is stepped to 1 $p.u.$

In Figure 8.6, the same plots are shown but with a zoomed view to display the wave-forms and events during the first moments of energisation.

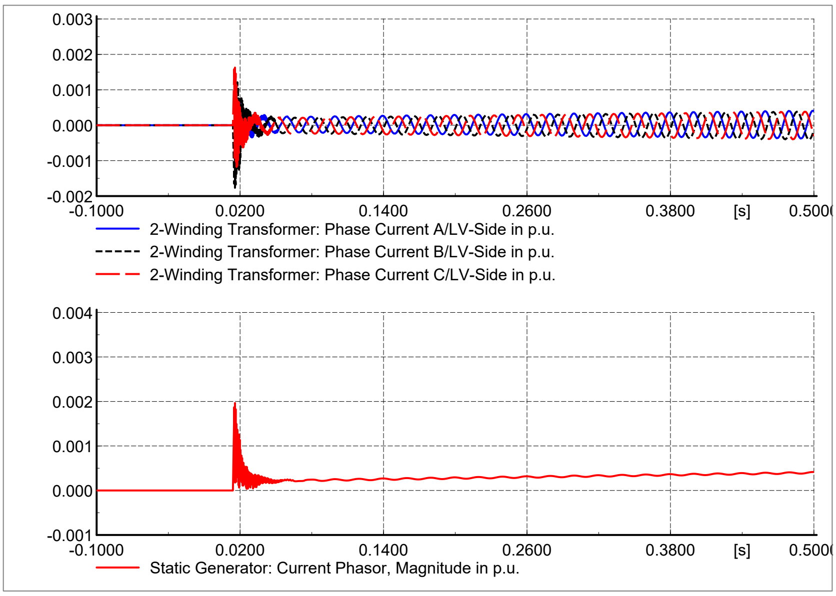


**Figure 8.6:** Zoomed in view of the currents during black start with soft energisation protocol. At t=0.015 s the switches to $T_1$ and cable are closed, while $V_{ref}$ is stepped to 1 $p.u.$

In Figure 8.7, the obtained voltage profile from the LV-side of $T_1$ is shows as well as the voltage profile at the $Tm_{wt}$.

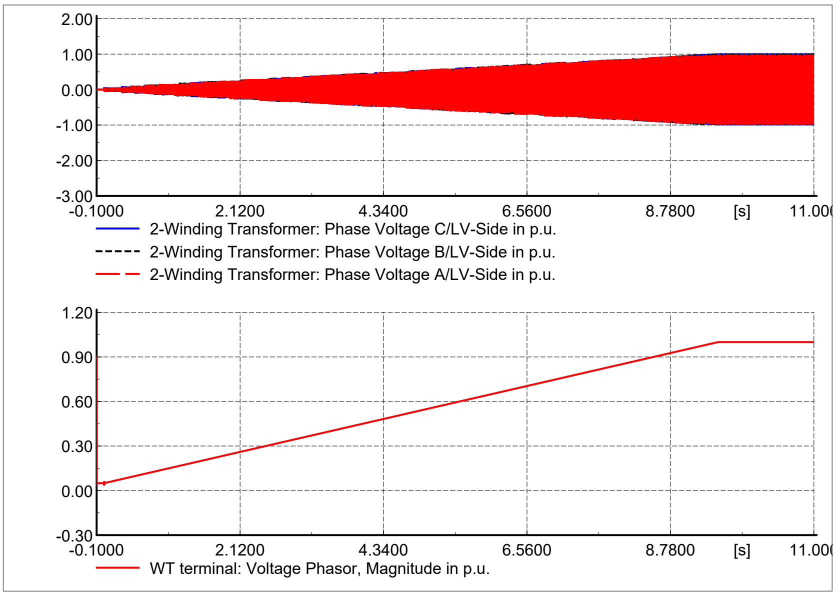


**Figure 8.7:** Voltages during black start with soft energisation protocol. At t=0.015 s the switches to $T_1$ and cable are closed, while $V_{ref}$ is stepped to 1 $p.u.$

In Figure 8.8, the same plots are shown but with a zoomed in view to display the wave-forms and events during the first moments of energisation.

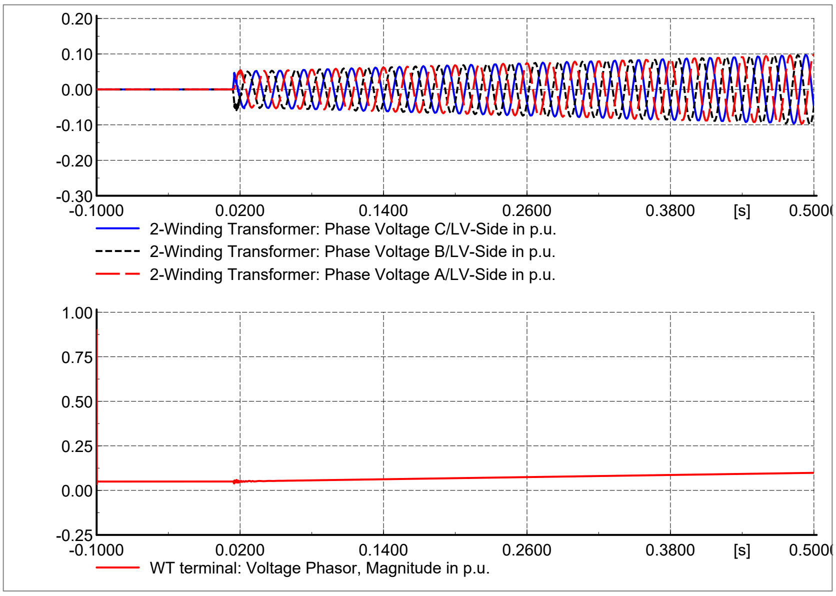


**Figure 8.8:** Zoomed in view of the voltages during black start with soft energisation protocol. At t=0.015 s the switches to $T_1$ and cable are closed, while $V_{ref}$ is stepped to 1 $p.u.$

From Figures 8.5 and 8.6, it is seen that there are fast transients in current at the beginning of the energisation process, just like in the case with hard energisation, but with a noticeable lower magnitude. The steady-state is reached slower in this case, due to the ramping of voltage. The real gain from this process is the lower risk for damaging the equipment during the energisation process, due to high and fast transients.

From Figures 8.7 and 8.8, no overshoot in voltage is seen during the energisation process, which is the desired behaviour. The voltage is slowly ramped until it reaches steady-state levels of 1 p.u.

## 8.2 Off-grid operation

In Figure 8.9 the obtained result for active power response is shown when a change in loading demand happens.

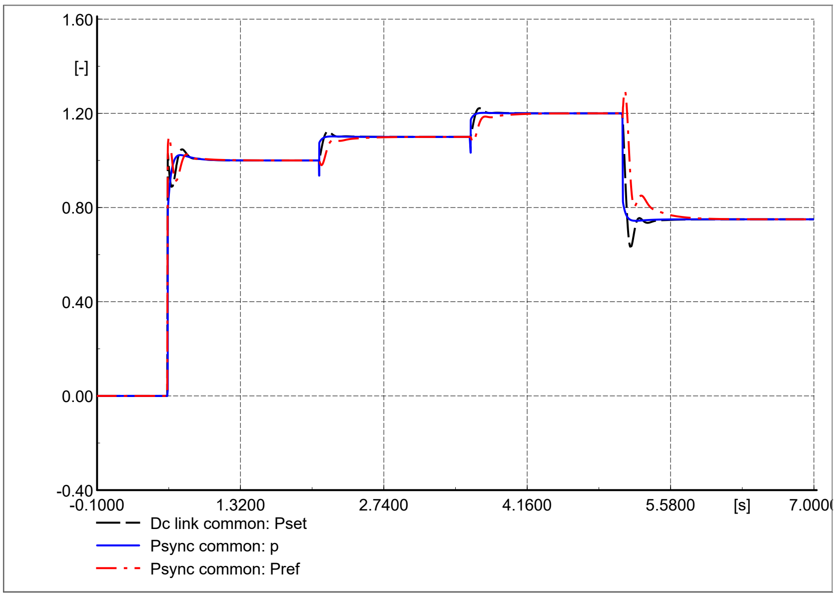


**Figure 8.9:** Power response from the converter when the breaker between $Tm_{WT}$ and $Tm_{Load}$ is closed at 0.3 s, $P_{inref}$ is increased from 0 to 1 $p.u$ as well as load $L1$ and $L2$ (0.75 + 0.25 $p.u$) are connected at 0.6 s. At 2.1 s $L3$ of 0.1 $p.u$ is connected. At 3.6 s $L4$ of 0.1 $p.u$ is connected so the total load demand is 1.2 $p.u$. At 5.1 s load shedding occurs, disconnecting loads $L2$, $L3$ and $L4$ so the total load demand is 0.75 $p.u$. $P_{set}$ (black dashed line) is the power outputted from the DC-link, $p$ (blue solid line) is the output power of the converter, $p_{ref}$ (red dashed line with dots) is the reference power for the converter.

In Figure 8.10 the obtained result for frequency response at $Tm_{WT}$ when changing loading demand is seen. In Figure 8.11 the obtained result for voltage response at $Tm_{WT}$ when changing loading demand is seen.

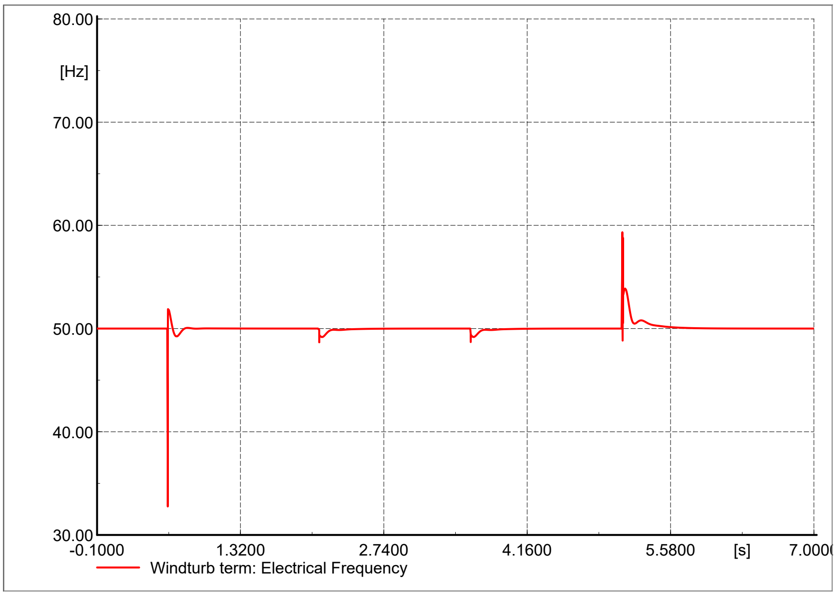


**Figure 8.10:** Frequency response at terminal $Tm_{WT}$, when the breaker between $Tm_{WT}$ and $Tm_{Load}$ is closed at 0.3 s, $P_{inref}$ is increased from 0 to 1 $p.u$ as well as load $L1$ and $L2$ ($0.75 + 0.25$ $p.u$) are connected at 0.6 s. At 2.1 s $L3$ of 0.1 $p.u$ is connected. At 3.6 s $L4$ of 0.1 $p.u$ is connected so the total load demand is 1.2 $p.u$. At 5.1 s load shedding occurs, disconnecting loads $L2$, $L3$ and $L4$ so the total load demand is 0.75 $p.u$.

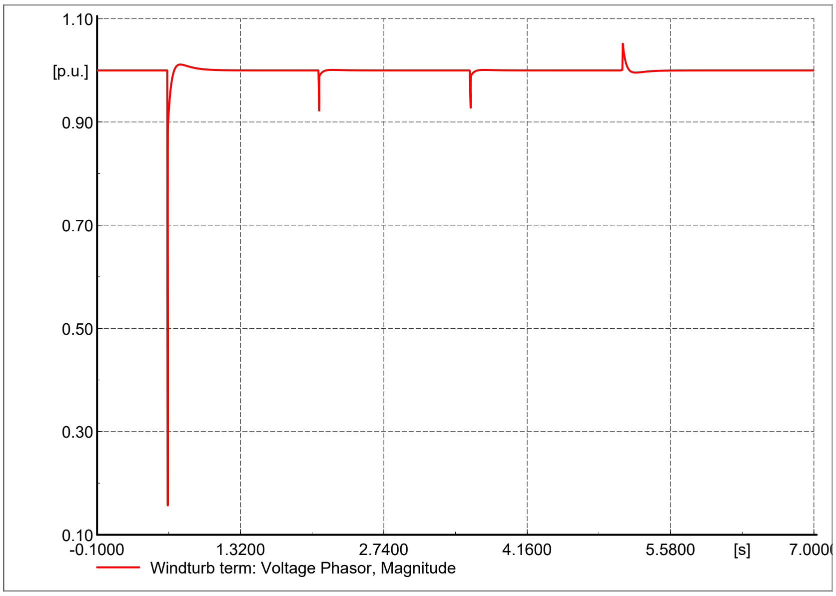


**Figure 8.11:** Voltage response at terminal $Tm_{WT}$, when the breaker between $Tm_{WT}$ and $Tm_{Load}$ is closed at 0.3 s, $P_{inref}$ is increased from 0 to 1 $p.u$ as well as load $L1$ and $L2$ ($0.75 + 0.25$ $p.u$) are connected at 0.6 s. At 2.1 s $L3$ of 0.1 $p.u$ is connected. At 3.6 s $L4$ of 0.1 $p.u$ is connected so the total load demand is 1.2 $p.u$. At 5.1 s load shedding occurs, disconnecting loads $L2$, $L3$ and $L4$ so the total load demand is 0.75 $p.u$.

The result in Figures 8.9, 8.10 and 8.11, shows that the controller has good dynamic response when changing the load demand in small steps, that occurs at 2.1 s and 3.6 s. There is hardly any overshoot in power response, frequency response and voltage response. However, when the load shedding event occurs at 5.1 s, problems in frequency response is seen where a large frequency spike is obtained that almost reaches 60 Hz. This may lead to problems in power quality or even worse, lead to a cascading effect of having loads and generation being disconnected from the grid in the attempt of stabilising the grid to avoid a system collapse. There is a slight overshoot in power and voltage response as well, but the magnitudes of these are at an acceptable level compared to the frequency.

# 9

# Discussion of results

## 9.1 Discussion of testing and verification results

### 9.1.1 Overall discussion

The testing approach that has been used has provided good information regarding the behaviour of the controller. The controller as implemented has large overshoots and frequency variations that occur during steps in power, but these should be limited if a current controller is added preventing operation outside limitations. Since the voltage is controlled to 1 p.u if the current is limited then the power should be able to be limited as well. However, this has not been investigated. A potential problem when limiting the current is that it will affect the power and might create problems with the synchronisation process. With knowledge of what steps that can be expected in power one could design the converter to have headroom for the overshoots and the controller as implemented can be a viable option for implementation.

The DC-link is as presented integrating the power difference between $P_{set}$ and $P_{meas}$ which is then representing the energy in the DC-link. However, this approach is assuming that the energy can change instantaneously, independent of the characteristics of the capacitor. This approach has been deemed sufficient for the scope of this thesis since the energy in the DC-link is obtained and can be analysed. However, because of how this is implemented there is no way to add time-constants to the behaviour of the capacitor and therefore studies involving how large capacitor that is needed for a fixed amount of inertia is not possible to perform. This is because if the power is made to change slower and $P_{set}$ is changing instantly then as it has been implemented the controller would be unstable.

### 9.1.2 Grid strengths and speed of controller

The overshoots of the power step-response increase with higher SCR (as seen in Figure 7.4-7.7). Leading to the PSC not being a suitable option for very strong grids. However, in very strong grids the need for WTs to implement new control methods are not as important and therefore a controller can be designed to work as a conventional grid following unit during these situations and grid forming in weaker grids. The reason why it works better for weaker grids is most likely due to the basic principle of the PSC being aimed towards controlling the angle of the converter terminal. If the grid is strong the angle is stiff and therefore harder to control leading to a longer time before entering stability.

The value of $K_p/R_a$ has been proven to be tightly connected to the speed of the controller (as seen in Figure 7.8-7.11). Which is reasonable because $K_p$ is the proportional gain of the power error. However, it also leads to higher overshoots, which is also expected since this is the usual behaviour of a proportional controller. In the theory about PSC (in section 4.4) it also stated that $R_a$ is proportional to the speed of the controller which is proven since higher $R_a$ increases the speed. Even though the gains could be increased in some cases without entering instability the overshoot increased as well with higher $K_p/R_a$, which is not wanted in a real setup since this will probably trip the converter. The gain has to be chosen based on the availability in power-exchange between the grid and the converter so the converter can handle the overshoots.

### 9.1.3 Resistive ratio

It has been shown that with a higher resistive ratio the oscillation of the step-response in power increases both in magnitude and time (as seen in Figure 7.12-7.15). Normally more resistive components act as a damping factor which should lead to a decrease in oscillations. This behaviour can most likely be explained by the decreased angle stability that is correlated with an increase of losses in the system (which is correlating to higher resistive ratio), as can be seen by the larger deviation from the nominal angle during the transient event (Figure 7.17). This decrease in angle stability at the PCC will cause a problem since the PSC assumes it to be constant.

When the PSC calculates the angle corresponding to a power step it is assuming that this change will not lead to a large change in PCC angle. However, with a decreased angular stability the angle changes as a result of the change in power transmitted, leading to the PSC to change again, causing larger oscillations in the power output as well as the angle at the PCC.

The voltage magnitude at the PCC during steady-state is increased with a higher ratio (as seen in Figure 7.16). This is most likely due to the fact that with more resistive components the active losses are increasing and in order to push the wanted active power into the system (in this case 1 $p.u$) the voltage at the PCC has to be increased.

### 9.1.4 Voltage controller

A different approach of a voltage controller, a gain-time droop controller has been tested in Simulink instead of the PI-controller and works as intended. The reason for the small variation of voltage from the nominal is most likely referred to the operational point of the controller is close to 0 in reactive power which is seen in

Figure 7.19. The droop controller allows for a smaller reactive current to be drawn if compared to the PI controller in Figure 7.3 (almost 6.7 % smaller), which is preferred since the converter can be designed to be smaller. It should also allow for an easier connection to other generating units.

### 9.1.5 Virtual inertia

The implementation of virtual inertia has been proven to work as intended for the simplified setup of no DC-link controller where the power change has been made slower leading to much lower deviation in frequency (as can be seen in Figure 7.20 and Figure 7.21). However, a more robust way of choosing the parameters of the low-pass filter is suggested. When the DC-link controller is added the virtual inertia is not working properly. Even for a very small inertia constant of $H = 0.1$, large oscillations occur (as seen in Figure 7.22) which is also present in the frequency response seen in Figure 7.23. This is related to the implementation of the DC-link where $P_{set}$ is changing instantly but the measured power is made slower leading to instability. Therefore it would be preferred to add the inertial characteristics at the MSC instead which would make $P_{set}$ change slower leading to $P_{ref}$ and consequently the output power changing slower, i.e an inertial response would be obtained. Another contributing factor to this behaviour is how the capacitor was chosen to be modelled with no time constant that represented the charging and discharging of it. The result will be that if there is a difference between $P_{meas}$ and $P_{set}$, an instantaneous change in energy stored in the capacitor takes place that will affect the output power of the WT directly. Furthermore, there is a problem with the contradicting behaviour between the DC-link controller and low-pass filter. The DC-link controller tries to maintain the energy stored inside the capacitor, meanwhile, the low-pass filter wants to borrow energy from it, hence oscillations in power and frequency response occurs.

## 9.2 Discussion of system study results

### 9.2.1 Black start

In figures 8.1 and 8.2, it is seen that the inrush currents (named phase current in plot) into the LV-side of $T_1$ has a magnitude of roughly 0.036 $p.u$ at 0.015 s (starting from 0 $p.u$) during early stages of energisation, this decreases quickly to reach steady state levels of 0.005 $p.u$ at 0.08 s. Roughly the same behaviour is seen for the phase currents that are outputted from the static generator.

Figures 8.3 and 8.4, shows that initially the voltage is increased from 0 to 1.06 $p.u$ at the LV-side of $T_1$ and for $Tm_{wt}$ it is increased from 0 to 1.163 $p.u$, that is followed by a decrease before reaching steady state levels at 1 $p.u$ for $T_{WT}$ at 0.06 s and for $T_1$ at 0.06 s. However, the high values of current and voltage that is needed to black start with this method, sets high requirements on the WT to what it should be able to output.

When using the other method of soft energisation, it is seen that there is a noticeable difference in comparison to hard energisation. For soft energisation (figures 8.5 and 8.6), it is seen that the inrush currents (named phase current in plot) into the LV-side of $T_1$ has a magnitude of roughly 0.016 $p.u$ at 0.016 s (starting from 0 $p.u$) during early stages of soft energisation and then decreasing to under 0.0002 $p.u$ at 0.05 s, before increasing the amplitude in a linear manner until reaching steady-state levels of 0.004 $p.u$ at 9.5 s. Roughly the same behaviour is seen in the same figures for the phase currents that are outputted from the static generator, the difference is slightly greater magnitude at 0.026 s (increases to 0.002 $p.u$) and slightly lower(decreases close to 0.0002 $p.u$) at 0.07 s.

The voltage profile (figures 8.7 and 8.8) at both the $Tm_{WT}$ and LV-side of $T_1$ increases slowly with a linear fashion. The results show that hardly any transients occur at the beginning of the energisation process, instead, the voltages increase with linear fashion to steady-state levels at 1 $p.u$ for both measurement points, which is expected.

Between the two energisation methods, it is preferable to use soft energisation during black start to minimise inrush current and to avoid transients in voltage that might damage equipment or accidental tripping of protective relays which will lead to failed energisation. If the losses in the system were higher compared to the rating of the WTs, transients above 1 $p.u$ can occur. In such cases using hard energisation will require headroom in the converters and transformers ratings, or instead of having headroom in the converters, having additional energy storage to supply the additional energy needed during the transient event. For instance, if the ratings of the WTs were as in the verification part ($S_{base} = 0.0127MW$) and the transformers were scaled accordingly but the cable left as is, the inrush current using hard energisation would reach almost 2 $p.u$ and the voltage would rise to approximately 1.5 $p.u$.

### 9.2.2 Off-grid operation

During off-grid operation, the controller offers good dynamic performance for power and voltage response when the power demand changes in small steps. For power response, small changes in power demand, i.e 0.1 $p.u$ increase that happens at 2.1 s and 3.6 s, the overshoots are small. Of course, some bigger oscillations will occur for power, voltage and frequency at 0.6 s, but this is due to the start of the simulation and initialisation of the system model. It works relatively good for bigger changes, like when the load shedding occurs at 5.1 s, there are some overshoots in power response of the controller when it tries to cope with the changing demand, but these are hardly a big problem. The same goes for the voltage response, transients appear during connection and disconnection of the loads. The deviation of the transients from steady-state when the load demand is increased with 0.1 $p.u$ is roughly 0.07 $p.u$, and for the load shedding event the deviation is 0.05 $p.u$, but these transients are manageable. It seems that the connection of loads creates slightly bigger transients in voltage at $Tm_{WT}$ than disconnection. For frequency response, connection of loads (in this case representing 0.1 $p.u$ increase in demand) seems to create small transients, i.e the frequency decreases down to 48.0 Hz for about 0.2 s. The magnitude and time are still in range with the guidelines stated in [36], which means that the converter should be able to stay connected to the grid. Furthermore, if other generators were connected during the frequency deviation, they should also be able to stay connected for such steps in power. However, when the disconnection of loads occur or rather load shedding, the frequency is increased up to almost 59 Hz for a time duration of 0.7 s. This is not an acceptable response since users connected to the grid will experience problems in power quality and there is a high likelihood of having a grid collapse.

One solution to fix this problem with the vast increase in frequency response for load shedding would be to increase the speed of the controller, but this would be hard to do without making the power and voltage response unstable. The best way would be to introduce inertia in the controller to smoothen out the changes and act against the rapid change in frequency, i.e the RoCoF. This could be done by using Virtual inertia-control methods for the converters or by using energy storage in the form of batteries if the converter connected units were maintained at a penetration of 100% in the grid. If the grid consisted of some conventional generation as well, it would have been a good way to solve the problem, since synchronous generators naturally offer inertia to the grid. Except for this problem with frequency spikes that are introduced during load shedding, the converter acts as desired.

## 9.3 Future studies

In this section, interesting future studies that were not further investigated in the thesis will be presented.

### 9.3.1 Island detection and re-connecting to grid

It would be interesting to use the converter-controller in a setup where it is connected to a grid and suddenly disconnected. Having the controller detect that it is operating in islanding condition. It would also be interesting to add the option to the controller to reconnect to the grid by controlling the amplitude, angle and phase order of the voltage to be the same as for the grid. This would probably require an extra control block for the angle, were the angle calculated from the PS-loop is compared to the grid angle and then passed through a PI-controller before used. The voltage measurement point would also have to be changed to the grid.

### 9.3.2 Changes in converter controller scheme

Current control would be interesting to add, and even necessary to add if transient overshoots in the step-response are to be avoided since at this stage there is no current control to prevent high currents enter the converter during transients. An easy way would be to implement some limiter to avoid this event to happen. This is also an important control for fault-ride-through, i.e maintaining the connection of the WT to the grid for a short period during voltage dips, avoiding load shedding.

However, this might interfere with the synchronisation process and could lead to problems regarding system stability and should be analysed further.

In this project the DC-link has been modelled in a specific way, measuring the difference between input power ($P_{set}$) created from wind and the measured output power ($P_{meas}$) at the WT terminal. The DC-link capacitor is modelled to be a set value and the energy stored in it is described by equation 4.3.

The disadvantage of modelling the DC-link in this way is that it sets hard requirements for having no measurement error between the measured and $P_{set}$ and $P_{meas}$ otherwise the energy absorbed or injected from the DC-link will not be accurate and by so affecting the stability of the grid parameters. There is also a risk for making the converter unstable because the error is being integrated, making the reference power $P_{ref}$ go to infinity, hence never reaching a power equilibrium. It is also as stated previously not considering the capacitor time-dependency when calculating the energy in the DC-link.

One solution would be to model the MSC as a constant current source and calculating the voltage in the DC-link by measuring the current in to and out from the DC-link and the difference is the current going into the capacitor which could be used to calculate the voltage and consequently the energy.

### 9.3.3 Energy storage and offered virtual inertia

Energy storage is an alternative when wanting to offer virtual inertia for WTs, these can be in the form of large DC-link capacitor or batteries. Without any energy storage, the converter will have trouble injecting or absorbing power from the grid, making it more sensitive to transients, faults and voltage dips.

The interesting thing would be to investigate the size of the energy storage and how much inertia that needs to be contributed to the grid during certain events. As well as if it is reasonable that the energy storage fits into the nacelle or if it is forced to be installed next to the WT and will this become a problem for offshore wind farms. For it to work the DC-link has to be implemented in a way that enables the DC-link capacitor characteristics and test by increasing the capacitor until satisfactory virtual inertia can be implemented.

### 9.3.4 Changes in grid topology

As the grid was greatly simplified in size and complexity, future studies could be conducted to test how the converter behaves with a larger grid, that is more complex or phase together other interconnected grids.

Another system study would be to change the penetration of RES that is being used at a specific time to investigate how well or even if the converter can be implemented into the grid without making the grid prone to blackouts, despite not offering the inertia that is given by the conventional SGs. It would also be useful to see how the converters can handle faults in the grid, will they start to shed loads or can they maintain a stable operation during fault events.

### 9.3.5 Machine side modelling

In order to obtain an optimal power production, there need to be control systems that configure the setup of the WT, such as nacelle angle, rotor speed, operation time to obtain the most sufficient production. In the presented thesis the machine side properties were simplified to be seen as a constant power source. However, several improvements could have been done to model it more accurately. As of now, the wind was assumed to be present at all times, no highs or lows in wind speed or other variations like the angle of the nacelle, pitching of the blades and so on to take into account.

One of the most important control systems of a WT is the pitching control that prevents the rotors from gaining high speed during strong winds and by so avoiding failure of the wind turbine. But, except for protection reasons, the pitching control is useful when regulating the frequency. By changing the rotor blades angle, the energy absorbed by the wind can be varied, hence changing the amount of power outputted into the grid. This characteristic of changing output power with the goal of stabilising the frequency in the grid is an effective method as shown in [61] that is being used in type-3 WTs. This would then replace the "frequency to power difference" control-block that was added in the off-grid setup. A wind study would be beneficial in this aspect, especially when wanting to test the ability of the DC-link to maintain the voltage at the WT terminal or see the improvements in stability that is obtained when using pitching control.

## 9.4 Ethics and sustainability

### 9.4.1 Ethics

Every project will experience situations where ethical dilemmas may occur. Throughout this project, the IEEE code of Ethics has been used to ensure that the project in all parts has been conducted ethically.

All of the points (taken from [62]) are important and have been followed, but some parts could more easily be related to this project and those were the following; Point (3), providing valid data and make realistic and honest claims from that data has been of the utmost importance since most of the claims made in this thesis was based on the collected data. Point (9), since most of the facts stated in this report are gathered from other scientific papers we had a responsibility to ensure that the facts stated are actually what is stated in those reports to not injure others reputation. Point (7), in the same way crediting the work and contribution of others, has been a focus point. Point (5), we had a responsibility to not only present the possibilities with the findings in this thesis but also the potential consequences by implementing this both in large and small scale. Point (2), since DNV-GL is a consultant firm that is financed by their services, we had to remain unbiased to not make claims that certain technology is superior to an another, even though it might have been in DNV-GLs interest to implement more RES to increase their consultant opportunities.

### 9.4.2 Sustainability

From a sustainable standpoint, there are a lot of benefits that this research can provide.

#### 9.4.2.1 Ecological aspects

Higher penetration of RES is needed to reach climate goals. To succeed with this new control methods will have to be implemented. If control methods similar to what is presented in this report will be developed, the need for synchronous generators in the grid will not be as important or in future not needed at all. In a lot of countries, this will allow for the closing of energy productions based on non-renewable sources which will most likely contribute to ensure the fulfilment of the climate goals. The outcome of this thesis also proves the possibilities of black start and off-grid operation which, at present, is typically solved using diesel generators.

#### 9.4.2.2 Economic aspects

There is an argument that with less traditional generation job opportunities in many companies and industries working with these technologies could decrease. However, the change to higher penetration of RES will create a lot of work opportunities in several industries. Since this is an emerging market with a lot of demand there will be big opportunities for new companies and manufacturers and smaller companies to expand, creating jobs not only for themselves but also for suppliers of materials. Since the electrical grid will move from traditional generation with well-known behaviour into a new type of generation there will be a need for experts that can work together to ensure a future stable grid. This will most likely result not only in work opportunities System operators market but also for consultants. There will also be a need for new infrastructure with a lot of new installations of RES. This will also result in job opportunities.

As of all installations in the electric market if there are no subsidies from the government the cost will eventually be paid by the end customer which might lead to a higher electricity cost. However, if the government supports the change economically this will be less of a concern.

An argument could be made that the economical cost of this change is too high for replacing a technology that has been proven to work. However, the money can be seen as an investment as well that will create a lot of new work and therefore generate more taxpayers which in turn will generate income for the state.

#### 9.4.2.3 Social aspects

Many countries have realised that to prohibit the severe climate changes there will be a need for more environmental energy production. This means that even if there is an economic recession, investments still have to be made in this area. This will ensure future work for the industries related to this and thereby bring a sense of more security regarding work for the employees and the companies.

There is a risk that when moving towards higher penetration of RES instead of using the well known and reliable generation that exists today that there will be more blackouts. Though this research might assist for a faster black start procedure it is still an incident where industries and people will lack electricity. This can have severe outcomes in scenarios involving hospitals but also severe economic impact for companies and society as a whole. Higher penetration of RES will also mean that the energy supply will be more dependent on weather, i.e amount of wind and sunshine. There is a risk that the consumers of electricity will have to accept that some electrical equipment has to be controlled in time in the future to make sure that the demand does not exceed the supply. Maybe the car cannot be charged whenever you want but rather you have to choose a time when it is supposed to be fully charged and then the system operator can choose the time where sufficient electricity is available.

From a maintenance point of view, high penetration of RES with more distributed generation is beneficial since instead of losing a big generation unit during maintenance a smaller one is now lost instead.

One important social concern is that wind parks have to be built somewhere. People, in general, are not that keen on living next to a wind turbine and if built offshore it might interfere with the fishing industry leading to higher prices for locally caught fish. Another concern by more wind parks is the reduced flight zones for the military.

# 10

# Conclusion

The focus on this thesis has been to present a converter controller for a Type 4 WT that offers both black start and off-grid capabilities based on the power synchronisation method. The presented controller for black starts has been proven to work and it is concluded that soft energisation is the best approach when using RES for black start since this reduces the inrush current, voltage transients and allows for smaller momentary energy-need. The proposed controller for off-grid operations has been concluded to work and could be implemented in such situations. However, since no virtual inertia is implemented large frequency spikes occur if large steps in loading are conducted. Furthermore, for an increased loading condition of 0.1 $p.u$ it is concluded that the frequency spikes are within the range of acceptable limits according to Swedish grid-codes.

Additional testing of the power synchronisation controller has shown that the step-response in active power is more stable for weaker grids and that the resistive ratio of the Thevenin equivalent grid affects the stability of the step-response to be more unstable if increased. This is most likely referred to the decreased angular stability at the PCC, present as a result of increased losses in the system. The resistive ratio also affects the voltage magnitude at the PCC and consequently the operation of the voltage controller. For a resistive ratio of 10% and a SCR of 3, both a hard voltage controller and a gain-time droop controller has been successfully tested. Based on the testing of the controller, with the parameter-selection proposed in this thesis, it has been concluded that the converter should be designed with headroom for the transient overshoots in power that occurs, alternatively investigate how a current controller can be implemented without interfering with the synchronisation process. The addition of virtual inertia has been tested and could be an important addition to decrease frequency spikes during steps in active power by mimicking the response of a SG. However, it is also concluded that it would be better to implement the ability for virtual inertia on the machine side rather than after the DC-link.

# Bibliography


[1] A. Gustafsson and P.-J. Rigole, “IEA wind TCP annual report - sweden”, 2017.

[2] C. B. Wahlèn. (2019). IRENA report finds 5 percent increase in renewable energy compared to 2016, [Online]. Available: https://sdg.iisd.org/news/irena-report-finds-5-increase-in-renewable-energy-compared-to-2016/ (visited on 01/22/2020).

[3] World Nuclear Association. (2019). Nuclear power in sweden, [Online]. Available: https://www.world-nuclear.org/information-library/country-profiles/countries-o-s/sweden.aspx (visited on 01/22/2020).

[4] Vattenfall. (2019). Smarta elnat, [Online]. Available: https://www.vattenfalleldistribution.se/vart-arbete/smarta-elnat/ (visited on 01/22/2020).

[5] M. A. Tabrizi. (2015). Integration of renewable energy sources: Strong challenge for a weak grid, [Online]. Available: https://blogs.dnvgl.com/energy/integration-of-renewable-energy-sources-strong-challenge-for-a-weak-grid (visited on 01/21/2020).

[6] J. R. Gracia, L. C. Marke, D. T. Rizy, P. W. O’Connor, R. Shan, and A. Tarditi, “Hydropower plants as Black start resources”, Hydrowires U.S department of energy, 2019.

[7] A. El-Zonkoly, “Integration of wind power for optimal power system black-start restoration”, *Turkish Journal of Electrical Engineering & Computer Sciences*, vol. 23, pp. 1853–1866, 2015.

[8] National Grid ESO, “Black start from non-traditional generation technologies”, Network Innovation Allowance, Jun. 2019.

[9] European Comission. (2019). Transforming the EU power grid to realise climate goals, [Online]. Available: https://www.world-nuclear.org/information-library/country-profiles/countries-o-s/sweden.aspx (visited on 01/22/2020).

[10] ENTSO-E, “TYNDP 2018 Scenario Development Report”, ENTSO-E, 2018.

[11] ENTSO-E, “TYNDP 2016 Scenario Development Report”, ENTSO-E, 2016.

[12] Eurostat. (2019). Renewable energy statistics, [Online]. Available: https://ec.europa.eu/eurostat/statistics-explained/index.php?title=Renewable_energy_statistics (visited on 02/11/2020).

[13] ENTSO-E Technical Group on High Penetration of Power Electronic Interfaced Power Sources, “High penetration of power electronic interfaced power

sources and the potential contribution of grid forming converters", ENTSO-E, 2020.

[14] M. A. Tabrizi. (2015). Integration of renewable energy sources: Strong challenge for a weak grid, [Online]. Available: `https://blogs.dnvgl.com/energy/integration-of-renewable-energy-sources-strong-challenge-for-a-weak-grid` (visited on 02/11/2020).

[15] A. Robb. (2019). Grid inertia: Why it matters in a renewable world, [Online]. Available: `https://www.renewableenergyworld.com/2018/09/05/to-add-more-renewables-to-the-grid-we-need-energy-storage-with-a-critical-component-inertia/#gref` (visited on 05/26/2020).

[16] E. Ibrahim, "Experimental measurements of fault level for sceco west, kingdom of saudi arabia", *Journal of King Abdulaziz University-Engineering Sciences*, vol. 15, Jan. 2004. DOI: `10.4197/Eng.15-1.6`.

[17] ENTSO-E, "High penetration of power electronic interfaced power sources (hpopeips)", ENTSO-E, 2017.

[18] T. H. Mohamed, J. Morel, H. Bevrani, and T. Hiyama, "Model predictive based load frequency control$_{d}$*esignconcerningwindturbines*", *International Journal of Electrical Power  Energy Systems*, vol. 43, no. 1, pp. 859–867, 2012, ISSN: 0142-0615. DOI: `https://doi.org/10.1016/j.ijepes.2012.06.032`. [Online]. Available: `http://www.sciencedirect.com/science/article/pii/S0142061512002943`.

[19] F. Morales. (2018). To add more renewables to the grid, we need energy storage with a critical component: Inertia, [Online]. Available: `https://www.renewableenergyworld.com/2019/10/25/grid-inertia-why-it-matters-in-a-renewable-world/#gref` (visited on 02/11/2020).

[20] Western Power Distribution, "Low frequency demand disconnection", Western Power Distribution, 2018.

[21] H. Zhao and Q. Wu, *Status of Wind power Technologies*. Technical university of Denmark: Wiley-IEEE Press, 2018.

[22] S. K. Sahoo, A. K. Sinha, and N. K. Kishore, "Low voltage ride-through of a grid-connected doubly-fed induction generator with speed sensorless vector control", in *2016 National Power Systems Conference (NPSC)*, 2016, pp. 1–6.

[23] L. Harnefors, M. Hinkkanen, U. Riaz, F. M. M. Rahman, and L. Zhang, "Robust analytic design of power-synchronization control", *IEEE Transactions on Industrial Electronics*, vol. 66, pp. 5810–5819, Aug. 2019. DOI: `10.1109/TIE.2018.2874584`.

[24] National Grid ESO. (2020). Black start, [Online]. Available: `https://www.nationalgrideso.com/balancing-services/system-security-services/black-start?technical-requirements` (visited on 01/22/2020).

[25] Elia. (2018). Design note on restoration services, [Online]. Available: `https://www.elia.be/en/public-consultation/20181005-review-of-the-black-start-ancillary-service` (visited on 01/22/2020).

[26] Ying Jiang-Hafner, H. Duchen, M. Karlsson, L. Ronstrom, and B. Abrahamsson, "HVDC with voltage source converters - a powerful standby black start facility", in *2008 IEEE/PES Transmission and Distribution Conference and Exposition*, 2008, pp. 1–9.

[27] DNV GL-Energy, "Reducing the risks of network restoration", DNV GL, Jul. 2016.

[28] S. Li, M. Zhou, Z. Liu, J. Zhang, and Y. Li, "A study on VSC-HVDC based black start compared with traditional black start", in *2009 International Conference on Sustainable Power Generation and Supply*, 2009, pp. 1–6.

[29] K. S. Nielsen, *Method of start up at least a part of a wind power plant, wind power plant and use of the wind power plant.* U.S. Patent 8,000,840, issued August 16, 2011. [Online]. Available: https://patents.google.com/patent/US8000840B2/en (visited on 01/28/2020).

[30] P. Egedal, S. Kumar, and K. S. Nielsen, *Black start of wind turbine devices*, U.S. Patent 9,509,141, issued Nov. 2016. [Online]. Available: https://patents.google.com/patent/US9509141 (visited on 01/28/2020).

[31] J. Aho, A. Buckspan, J. Laks, P. Fleming, Y. Jeong, F. Dunne, M. Churchfield, L. Pao, and K. Johnson, "A tutorial of wind turbine control for supporting grid frequency through active power control", in *2012 American Control Conference (ACC)*, 2012, pp. 3120–3131.

[32] A. Jain, K. Das, O. Goksu, and N. Cutululis, "Control solutions for blackstart capability and islanding operation of offshore wind power plants", Jan. 2018. DOI: 10.5281/zenodo.3269542.

[33] J. Tan and Y. Zhang, "Coordinated Control Strategy of a Battery Energy Storage System to Support a Wind Power Plant Providing Multi-Timescale Frequency Ancillary Services", *IEEE Transactions on Sustainable energy*, vol. 8, pp. 1140–1153, Jul. 2017. DOI: 10.1109/TSTE.2017.2663334.

[34] J. Xi, H. Geng, G. Yang, and S. Ma, "Inertial response analysis of PMSG-based WECS with VSG control", *The journal of engineering*, vol. 13, pp. 897–901, Oct. 2017. DOI: 10.1049/joe.2017.0459.

[35] A. Khamis, H. Shareef, E. Bizkevelci, and T. Khatib, "A review of islanding detection techniques for renewable distributed generation systems", *Renewable and Sustainable Energy Reviews*, vol. 28, pp. 483–493, 2013, ISSN: 1364-0321. DOI: https://doi.org/10.1016/j.rser.2013.08.025. [Online]. Available: http://www.sciencedirect.com/science/article/pii/S1364032113005650.

[36] G. Morèn. (2018). Engergimarknadsinspektionens forfattningssamling, [Online]. Available: https://www.ei.se/Documents/Publikationer/foreskrifter/El/EIFS_2018_2.pdf.

[37] B.-Y. Bae, J.-K. Jeong, J.-H. Lee, and B.-M. Han, "Islanding detection method for inverter-based distributed generation systems using a signal cross-correlation scheme", *Journal of Power Electronics*, vol. 10, no. 6, pp. 762–768, Nov. 2010.

[38] S. Raza, H. Mokhlis, H. Arof, J. Laghari, and L. Wang, "Application of signal processing techniques for islanding detection of distributed generation in distribution network: A review", *Energy Conversion and Management*, vol. 96, pp. 613–624, 2015, ISSN: 0196-8904. DOI: https://doi.org/10.1016/j.enconman.2015.03.029. [Online]. Available: http://www.sciencedirect.com/science/article/pii/S0196890415002393.

[39] L. Fusheng, L. Ruisheng, and Z. Fengquan, "Chapter 11 - a practical case", in *Microgrid Technology and Engineering Application*, L. Fusheng, L. Ruisheng,

and Z. Fengquan, Eds., Oxford: Academic Press, 2016, pp. 155–172, ISBN: 978-0-12-803598-6. DOI: https://doi.org/10.1016/B978-0-12-803598-6.00011-5. [Online]. Available: http://www.sciencedirect.com/science/article/pii/B9780128035986000115.

[40] Q. Gao and R. Preece, "Improving frequency stability in low inertia power systems using synthetic inertia from wind turbines", in *2017 IEEE Manchester PowerTech*, 2017, pp. 1–6.

[41] L. Zhang, L.Harnefores, and H.Nee, "Power-synchronization control of grid-connected voltage-source converters", *IEEE Transactions on Power Systems*, vol. 25, pp. 809–820, May 2010. DOI: 10.1109/TPWRS.2009.2032231.

[42] E. Clarke, *CIRCUIT ANALYSIS OF A-C POWER SYSTEMS*. New York: JOHN WILEY & SONS Inc., 1950.

[43] L. Harnefors, M. Bongiorno, and S. Lundberg, "Input-admittance calculation and shaping for controlled voltage-source converters", *IEEE Transactions on Industrial Electronics*, vol. 54, no. 6, pp. 3323–3334, 2007.

[44] M. Bongiorno, J. Svensson, and A. Sannino, "Effect of sampling frequency and harmonics on delay-based phase-sequence estimation method", *IEEE Transactions on Power Delivery*, vol. 23, no. 3, pp. 1664–1672, 2008.

[45] D. Pattabiraman, R. H. Lasseter., and T. M. Jahns, "Comparison of Grid Following and Grid Forming Control for a High Inverter Penetration Power System", *2018 IEEE Power & Energy Society General Meeting (PESGM)*, pp. 1–5, 2018. DOI: 10.1109/PESGM.2018.8586162.

[46] T. Ackermann, T. Prevost, V. Vittal, A. J. Roscoe, J. Matevosyan, and N. Miller, "Paving the Way: A Future Without Inertia Is Closer Than You Think", *IEEE Power and Energy Magazine*, vol. 15, no. 6, pp. 61–69, 2017.

[47] M. Rouse and J. Burke. (2016). Phase-locked loop, [Online]. Available: https://searchnetworking.techtarget.com/definition/phase-locked-loop (visited on 02/18/2020).

[48] H. Urdal, R. Ierna, and A. Roscoe, "Stability challenges solutions for power systems operating close to 100% penetration of power electronic interfaced power sources: Exchange of experience between hybrid and major power systems", English, 3rd International Hybrid Power Systems Workshop ; Conference date: 08-05-2018 Through 09-05-2018, May 2018. [Online]. Available: http://hybridpowersystems.org/.

[49] M. Bongiorno, *Promotion lecture for full professor*, Challenges and opportunities in power electronics dominated grids, Gothenburg, Feb. 2020.

[50] SalvatoreD'Arco, J. A. Suul, and O. B.Fosso, "A virtual synchronous machine implementation for distributed control of power converters in smartgrids", *Electric Power Systems Research*, vol. 122, pp. 180–197, May 2015. DOI: 10.1016/j.epsr.2015.01.001.

[51] S. Pholboon, M. Sumner, and R. Ierna, "Virtual synchronous machine control for grid transmission compliance studies", in *2019 International Conference on Smart Energy Systems and Technologies (SEST)*, 2019, pp. 1–5.

[52] P. F. Frack, P. E. Mercado, and M. G. Molina, "Extending the visma concept to improve the frequency stability in microgrids", in *2015 18th International*

*Conference on Intelligent System Application to Power Systems (ISAP)*, 2015, pp. 1–6.

[53] Q. Zhong, P. Nguyen, Z. Ma, and W. Sheng, "Self-synchronized synchronverters: Inverters without a dedicated synchronization unit", *IEEE Transactions on Power Electronics*, vol. 29, no. 2, pp. 617–630, 2014.

[54] Q.-C. Zhong and G. Weiss, "Synchronverters: Inverters that mimic synchronous generators", *IEEE Transactions on Industrial Electronics*, vol. 58, pp. 1259–1267, Apr. 2010. DOI: `10.1109/TIE.2010.2048839`.

[55] F. Díaz-González, A. Sumper, O. Gomis-Bellmunt, and R. Villafáfila-Robles, "A review of energy storage technologies for wind power applications", *Renewable and Sustainable Energy Reviews*, vol. 16, no. 4, pp. 2154–2171, 2012, ISSN: 1364-0321. DOI: `https://doi.org/10.1016/j.rser.2012.01.029`. [Online]. Available: `http://www.sciencedirect.com/science/article/pii/S1364032112000305`.

[56] K. Bullis. (2013). Wind turbines, battery included, can keep power supplies stable, [Online]. Available: `https://www.technologyreview.com/2013/05/07/113573/wind-turbines-battery-included-can-keep-power-supplies-stable/` (visited on 05/30/2020).

[57] I. Erlich, A. Korai, T. Neumann, M. Koochack Zadeh, S. Vogt, C. Buchhagen, C. Rauscher, A. Menze, and J. Jung, "New control of wind turbines ensuring stable and secure operation following islanding of wind farms", *IEEE Transactions on Energy Conversion*, vol. 32, no. 3, pp. 1263–1271, 2017.

[58] R. M. Mathur and R. K. Varma, "SVC Control Components and Models", in *Thyristor-Based FACTS Controllers for Electrical Transmission Systems*. 2002, pp. 93–141.

[59] P. M. Anderson and A. A. Fouad, "The elementary mathematical model", in *Power System Control and Stability*. 2003, pp. 13–52.

[60] B. Gao, C. Xia, N. Chen, K. Cheema, L. Yang, and C. Li, "Virtual synchronous generator based auxiliary damping control design for the power system with renewable generation", *Energies*, vol. 10, p. 1146, Aug. 2017. DOI: `10.3390/en10081146`.

[61] H. Xu, Ed., *Frequency control of wind turbine in power system*, North China Electric Power University, Baoding, Hebei Province, China: AIP Publishing, 2018.

[62] IEEE. (2020). Code of Ethics, [Online]. Available: `https://www.ieee.org/about/corporate/governance/p7-8.html`.

# A

# Appendix A - Verification of converter controller

The converter has been tested and verified based on [23] in four steps, as can be seen in the following sections, which for each step a new control loop has been added to the controller to increase the system functionality. All the fixed values used in the simulation can be seen in Table A.1 and the single-line representation of the test-grid used for verification is seen in Figure A.1.

**Table A.1:** Fixed values used in the simulation model as stated in [23].

| Parameter | Value | Unit |
|---|---|---|
| $S_{base}$ | 0.0127 | $[MVA]$ |
| $V_{base}$ | $\sqrt{\frac{2}{3}}\ 0.4$ | $[kV]$ |
| $\omega_{base}$ | $2\pi 50$ | $[rad/s]$ |
| $V_{DC}$ | 0.650 | $[kV]$ |
| $C_{DC}$ | 2.1 | $[mF]$ |

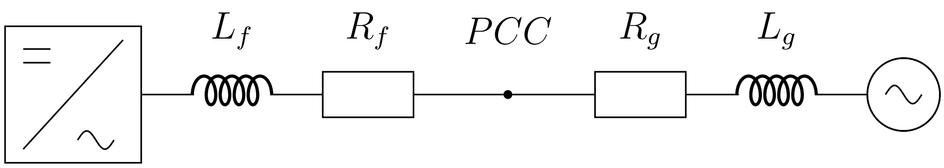


**Figure A.1:** The single-line representation of the grid setup used during testing. $L_f/R_f$ is the filter impedances, PCC is the point of common coupling i.e the wind-turbine terminal and $L_g/R_g$ is the Thevenin equivalent grid impedances.

### A.0.1 Test-setup 1: Power synchronisation loop

The first step was to verify the power synchronisation-loop without the damping circuit, voltage control block and DC-link control loop, as seen in Figure A.2. The reference power of the controller, $P_{ref}$, was stepped from 0 $p.u$ to 1 $p.u$ and then increased/decreased to 1.1 $p.u$, 1.2 $p.u$ and 0.75 $p.u$ to show the obtained response.

The reason for having both small and big steps in reference power was to observe how the controller reacts and if it could offer stable operation during these steps.

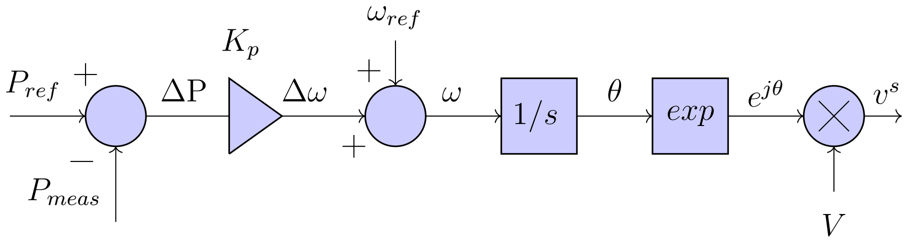


**Figure A.2:** Block diagram representing the first step in the testing protocol. $P_{ref}$ is the reference power for the controller, $P_{meas}$ is the measured power at the PCC, $K_p$ is the proportional gain of the controller, $\omega_{ref}$ is the nominal angular frequency, $V$ is a constant of 1 $p.u$ and $v^s$ is the voltage represented in $\alpha\beta$-frame.

The input $V$ that, in test-setup 4, is calculated from the voltage control block was set to 1 $p.u$ in this test and $P_{meas}$ was the measuring point at the WT's terminal (PCC). The goal was to verify if the Power synchronisation-loop (PS-loop) seen in Figure A.2 followed the change in $P_{ref}$ and that the frequency stabilises at 50 Hz. The output voltage was not investigated at this stage since no voltage controller was implemented in the controller, meaning that the voltage will not be controlled to 1 $p.u$. In Table A.2, the values used in DIgSILENT PowerFactory and Simulink for the active-power control gain, $K_p$, are listed.

**Table A.2:** Parameter values used for the active-power control gain, $K_p$ in the controller model during test-setup 1.

| Parameter | DIgSILENT PowerFactory | Simulink |
|---|---|---|
| $K_p$ | 0.2 | 0.1 |

### A.0.2 Test-setup 2: Damping circuit

The second part of the testing was done with the PS-loop and the current damping circuit with its high-pass filter included. $P_{ref}$ and $V$ were set to the same values as in step 1 including the stepping of $P_{ref}$ to make it easier to compare the results. The output of the converter was then observed to verify that the damping circuit had the effect of minimising variations in the output signal of the converter. The control configuration is seen in Figure A.3 and in Table A.3, where the used values in DIgSILENT PowerFactory and Simulink for $K_p$ and active resistance, $R_a$, are listed.

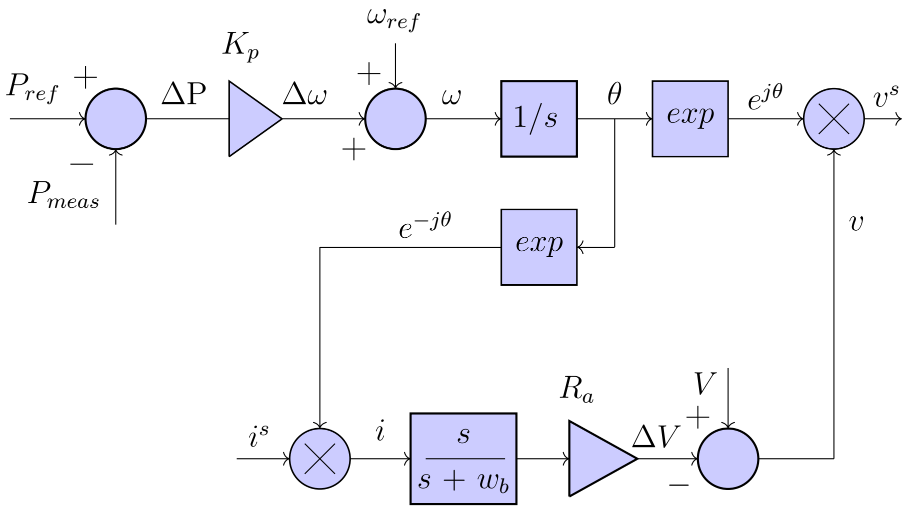


**Figure A.3:** Block diagram representing the second step in the testing protocol. $P_{ref}$ is the reference power for the controller, $P_{meas}$ is the measured power at the PCC, $\omega_{ref}$ is the nominal angular frequency, $K_p$ is the proportional gain of the controller, $R_a$ is the active resistance, $\omega_b$ is the bandwidth of the high-pass filter, $V$ is a constant of 1 $p.u$ and $v^s$ is the voltage represented in $\alpha\beta$-frame.

**Table A.3:** Parameter values used for $K_p$ and active resistance, $R_a$, in the controller model during test-setup 2.

| Parameter | DIgSILENT PowerFactory | Simulink |
|---|---|---|
| $K_p/R_a$ | 0.2 | 0.2 |

### A.0.3 Test-setup 3: DC-link implementation

The third part consisted of adding the DC-link control loop (seen in Figure A.4) to the PS-loop with the damping circuit, i.e adding the dynamics when the DC-link capacitor either absorbs or injects reactive current into the system to withhold the converter voltage. In previous test-setups, since no controller is added to analyse the behaviour of the energy stored in the capacitor and consequently the voltage magnitude present at the DC-link, it is assumed that the DC-link has constant energy.

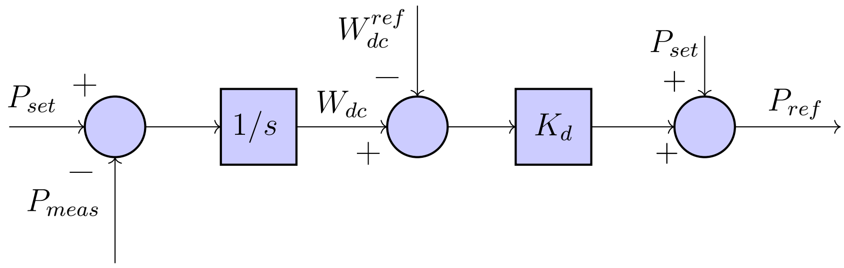


**Figure A.4:** Block diagram representing the third step in the testing protocol, i.e the dc-link control. $P_{set}$ is the power in to the DC-link, $P_{meas}$ is the power measured at the PCC, $W_{DC}$ is the energy stored in the DC-link, $W_{DC}^{ref}$ is the reference energy of the DC-link, $K_d$ is the DC-link proportional gain and $P_{ref}$ is the reference power for the PS-loop.

The proportional gain, $K_d$, was selected to be $K_d$= $0.18\omega_1$ based on the recommendations specified in [23]. The power flowing into the DC-link, $P_{set}$, was stepped with the same steps as $P_{ref}$ in the previous test-setups. The output power reference of the PS-loop ($P_{ref}$ in Figure A.3) depends on the available energy in the DC-link, meaning that if there is a change in DC-link energy, $P_{ref}$ will be affected accordingly. The output power and the energy stored in the DC-link capacitor were measured and analysed to verify the added dynamics, as well as the voltage magnitude of the WT. In Table A.4, the values used in DIgSILENT PowerFactory and Simulink for $K_p$, $R_a$ and the ideal control-loop bandwidth, $K_d$, are listed.

**Table A.4:** Parameter values used for $K_p$, $R_a$ and the ideal control-loop bandwidth, $K_d$, in the controller model during test-setup 3.

| Parameter | DIgSILENT PowerFactory | Simulink |
|---|---|---|
| $K_p/R_a$ | 0.15 | 0.15 |
| $K_d$ | 0.18 | 0.18 |

### A.0.4 Test-setup 4: Voltage controller

The fourth and last step of testing was focused on implementing the AC voltage controller (seen in Figure A.5). This was implemented to control the voltage error at the PCC. Instead of having $V$ set to 1 $p.u$, $V_{ref}$ was set to 1 $p.u$ and $V_{meas}$ was the measured voltage at the WT terminal (PCC), transformed into the rotational frame ($dq$) by using the angle $\theta$ calculated in the PS-loop. The reason why the angle $\theta$ was used, was because this is the angle used in the PS-loop to transform the current in the stationary frame ($\alpha\beta$) to the rotational frame. The error between $V_{ref}$ and $V_{meas}$ was then integrated with a PI-controller so the output voltage, $V$, was acquired. This was then forwarded to the PS-loop and used as the voltage input $V$ instead of the previously used 1 $p.u.$ The PI-controller's parameters ($K_p^{PI}$ and $K_i^{PI}$) were chosen based on trial and error. In Table A.5, the values used in DIgSILENT PowerFactory and Simulink for $K_p$, $R_a$, $K_d$, $K_p^{PI}$ and $K_i^{PI}$ are listed.

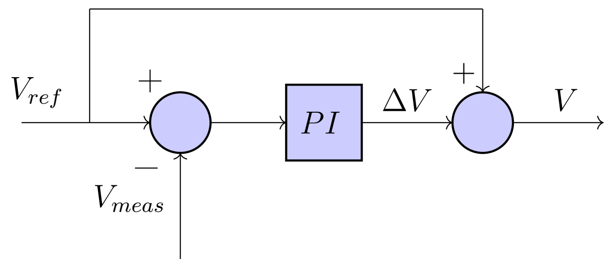


**Figure A.5:** Block diagram representing the fourth step in the testing protocol, i.e the voltage control. $V_{ref}$ is the reference voltage magnitude represented in $dq$-frame, $V_{meas}$ is the measured voltage at the PCC represented in $dq$-frame, the PI controller is built using a proportional and integral gain and $V$ is the voltage magnitude used for the converter reference.

**Table A.5:** Parameter values used $K_p$, $R_a$, $K_d$, $K_p^{PI}$ and $K_i^{PI}$ in the controller model during test-setup 4.

| Parameter | DIgSILENT PowerFactory | Simulink |
|---|---|---|
| $K_p/R_a$ | 0.15 | 0.15 |
| $K_d$ | 0.18 | 0.18 |
| $K_p^{PI}$ | 0.2 | 0.2 |
| $K_i^{PI}$ | 10 | 10 |

In Simulink, this step was simplified to only step the active power into the DC-link from 0 to 1 $p.u$ to avoid creating transients that would make it harder to see the difference between using the voltage controller and not using it. However, in DIgSILENT PowerFactory the energy in the DC-link was stepped from 0 to 1 $p.u$, 1.1 $p.u$, 1.2 $p.u$ and lastly down to 0.75 $p.u$ to see the behaviour of the DC-link when the same steps as in previous test-setups were used. Additionally, the reactive power measured at the PCC has been analysed for both scenarios when having the voltage controller connected and disconnected.

## A.1 Modelling differences

The two software, PowerFactory and Simulink, used for the simulations have some differences in how the converter controller and the test setup were modelled. In this section, the modelling differences will be highlighted and presented.

### A.1.1 DIgSILENT PowerFactory model

The test-grid setup seen in Figure A.6 has been implemented in DIgSILENT PowerFactory. The modelled test-grid consisted of a static generator, two terminals, an RLC-filter (with the capacitance neglected) and an AC voltage source. The reason for using an RLC-filter instead of a cable/transformer was to more easily change the impedance.

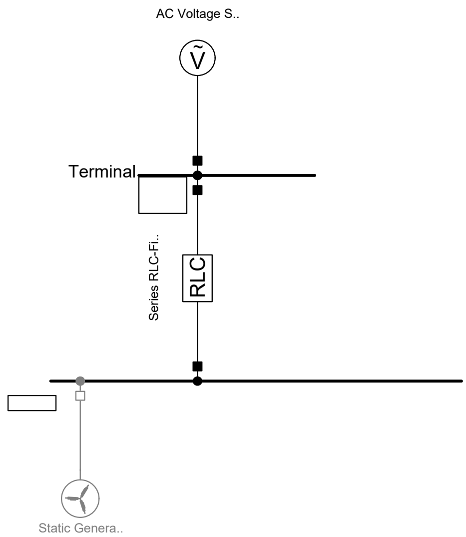


**Figure A.6:** The test-grid used for verification that consisted of a static generator with rated power of 0.0127 MVA and series reactance of 0.1 *p.u*, the two terminals, the RLC-filter and the AC voltage source. All components in the test-grid had a rated voltage of 0.4 kV. The switch that is closed after 2 s is seen located between the static generator and its terminal.

Grid parameters used for the RLC filter and AC source in these tests are presented in Table A.6.

**Table A.6:** Grid parameters used for the simplified grid during verification steps in DIgSILENT PowerFactory with the capacitance neglected in the RLC-filter.

| Type: | Step 1 | Step 2 | Step 3 | Step 4 |
|---|---|---|---|---|
| AC source [X/R] | 0.5 Ω/0.5 Ω | 0.5 Ω /0.5 Ω | 0.5 Ω/0.5 Ω | 0.5 Ω /0.5 Ω |
| RLC filter [L/R] | 10 mH/1.1 Ω | 10 mH/0.6 Ω | 10 mH/0.5 Ω | 10 mH/0.5 Ω |

Modelling of a controllable AC-source can be done in DIgSILENT PowerFactory through the predefined Genstat model (static generator). The static generator requires the real and imaginary part ($\alpha\beta$) of the voltage as input and transforms this into 3-phase quantities which is the output. The proposed converter is graphically represented as a single-phase system and then shifted to acquire the three-phase system.

In DIgSILENT PowerFactory all Clarke transformations are done by amplitude invariant scaling, therefore it has been converted into power invariant scaling through the multiplication of the obtained $\alpha$ and $\beta$ quantities in following way

$$\alpha\beta_{Pow} = \sqrt{\frac{3}{2}}\alpha\beta_{Amp} \tag{A.1}$$

that needs to be conducted before the Park transformation and then inverted back again after the inverse Park transformation in this way

$$\alpha\beta_{Amp} = \sqrt{\frac{2}{3}}\alpha\beta_{Pow} \tag{A.2}$$

so that the input to the static generator has the right scaling. The control block diagrams for this conversion are shown in Appendix B.

Compared to what was done in Simulink, the impedance of the grid and its ratio between $R_g$ and $X_g$ ($\omega_{nom} \cdot L_g$) were not fixed to be 10:1, instead, fine-tuning was conducted to obtain stable operations. All simulations were conducted in the electromagnetic transients simulation mode (EMT) since this offers better analysis for transient events compared to the root mean square method (RMS). RMS calculations are usually simplified and thus faster in computational time, EMT has a slower computational time but offer more detailed models. For the measurements of current, voltage, frequency and power, different predefined models were used in DIgSILENT PowerFactory. In Table A.7 each model used to measure a specific parameter are presented.

**Table A.7:** Predefined models for measurements of current, voltage, frequency and power in DIgSILENT PowerFactory. All measurement tools have been set to " rated to connected element/terminal".

| Parameter | Model | Unit |
|---|---|---|
| I | StaImea | $p.u$ |
| V | StaVmea | $p.u$ |
| F | StaVmea | $p.u$ |
| P | StaPqmea | $p.u$ |

All measurement tools measured in quantities of three-phase and then transformed them into the stationary frame with the common unit of $p.u$.

### A.1.2 Simulink model

The converter and test-grid have been modelled as in DIgSILENT PowerFactory based on Figure A.1 with the difference that in Simulink the three phases have been explicitly modelled using controlled voltage sources and series RLC branches, which has been implemented as RL branch types (all found in the Simscape library). The complete Simulink model can be found in Appendix E.2. The grid impedances, $L_g$ and $R_g$, has been defined as,

$$L_g = \frac{\frac{3}{2} \cdot V_{base}^2}{S_{base} \cdot SCR \cdot \omega_{nom}} \tag{A.3}$$

and

$$R_g = x \cdot \omega_{nom} \cdot L_g, \tag{A.4}$$

where the $x$ is the resistive ratio, SCR is the short circuit ratio and can be varied to simulate different grid-strengths, $V_{base}$, $S_{base}$ and $\omega_{nom}$ can be found in Table A.1. During the normal testing the resistive ratio has been set to 0.1. This differs from the DIgSILENT PowerFactory approach since in Simulink a fixed ratio between $L_g$ and $R_g$ is applied and the total grid impedance is changed according to the SCR. The SCR used in the different test-setups is shown in Table A.8 along with the corresponding grid impedances. The filter impedance seen in Figure A.1 has been set to $L_f = 0.15\%$ and $R_f = 0.015\%$.

**Table A.8:** SCR used during the different test-setups in Simulink as well as the corresponding resistive and inductive grid components ($R_g$ and $L_g$).

| Parameter: | Test-setup 1 | Test-setup 2 | Test-setup 3 | Test-setup 4 |
|---|---|---|---|---|
| SCR | 2 | 3 | 3 | 3 |
| $R_g$ [$\Omega$ ] | 0.6299 | 0.4199 | 0.4199 | 0.4199 |
| $L_g$ [$H$] | 0.0201 | 0.0134 | 0.0134 | 0.0134 |

For the measurements to be comparable to the DIgSILENT PowerFactory model where a power measurement device is used to measure the active power at the PCC (i.e. it measures the active power using the angle at the PCC), the Simulink model measures the angle in the PCC used for the Park transformations (of the voltage and current), using the approach described in section 3.6.3. The bandwidth has been selected as $\omega_{band} = 2\pi 5$ [rad/s] which is below the point where it should affect the output. Since this approach will make the measured angle lock the $q$-component of the voltage to zero the active power can be described as the product of the $d$-components of the current and voltage.

sectionVerification of converter control model in DIgSILENT PowerFactory The results obtained from the testing and verification in DIgSILENT PowerFactory is presented in this section.

### A.1.3 Power synchronization loop

The result of the first verification step is shown in Figure A.7. In this step $P_{ref}$ was set to 0 and $V$ to 1 initially, the switch between the static generator and its terminal was closed after 0.3 s and at the same time $P_{ref}$ was stepped from 0 to 1 $p.u.$ At 0.5 s and 0.7 s, $P_{ref}$ was increased with 0.1 $p.u$ before decreasing it to 0.75 $p.u$ at 0.9 s.

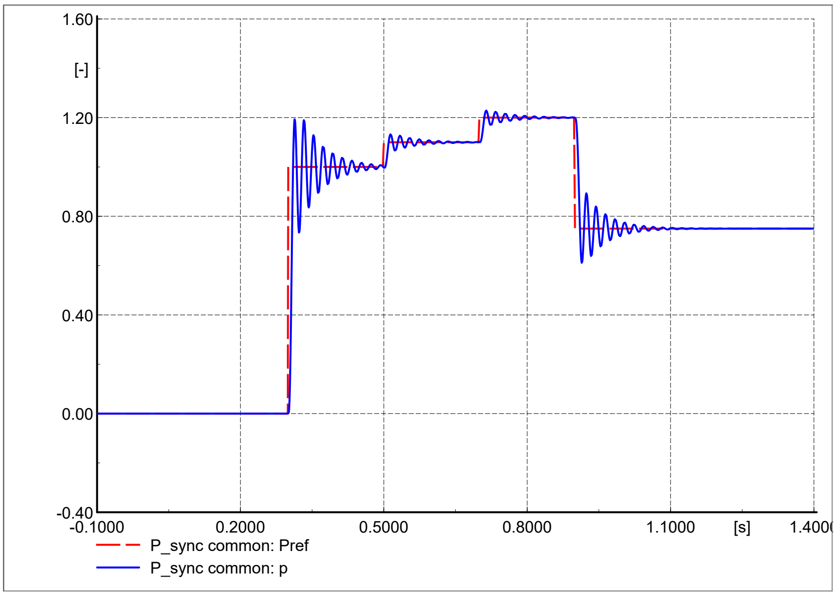


**Figure A.7:** The PS-loop controls the output power, $p$ (blue line), to follow the reference power, $P_{ref}$(red dashed), with a $K_p$ value set to 62.83 rad/s. At t=0.3 s the switch between the wind turbine and connection point to it terminal is closed, and $P_{ref}$ is increased from 0 to 1 $p.u.$ At t=0.5 s and t=0.7 s $P_{ref}$ is increased with 1.1 $p.u$ and 1.2 $p.u$ respectively, while at t=0.9s it is decreased to 0.75 $p.u.$

In Figure A.8 the electrical frequency at the static generator is seen, the goal is to maintain stable operation at 50 Hz.

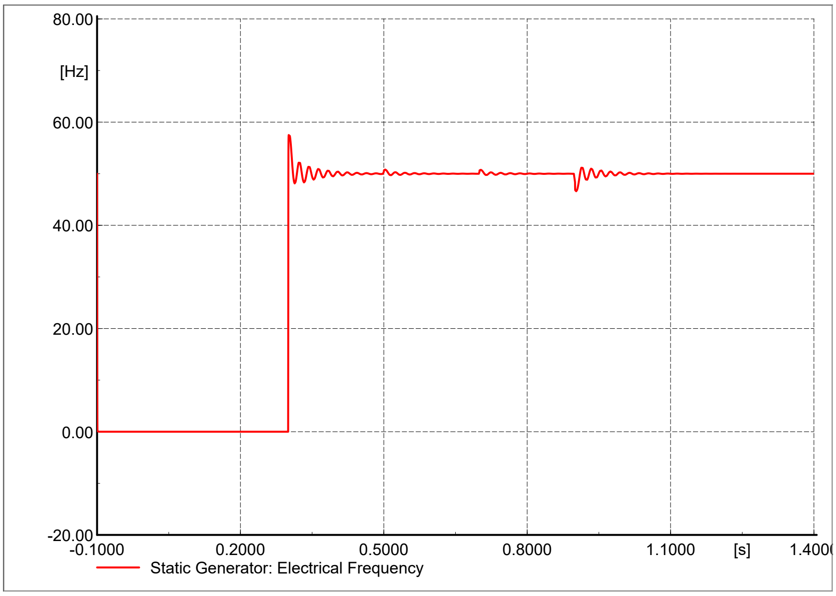


**Figure A.8:** The electrical frequency response in the static generator when $P_{ref}$ was stepped. The steps in $P_{ref}$ were done in the following order of magnitude 1 $p.u$, 1.1 $p.u$, 1.2 $p.u$ and 0.75 $p.u$ at time instances 0.3 s, 0.5 s, 0.7 s and 0.9 s. Note that the step from 0-50 $Hz$ in frequency is only present due to the implementation of the measurement in DIgSILENT PowerFactory.

### A.1.4 Damping circuit

In this part the damping circuit was added which was the second step in verification of the converter control model, the obtained result is shown in Figure A.9.

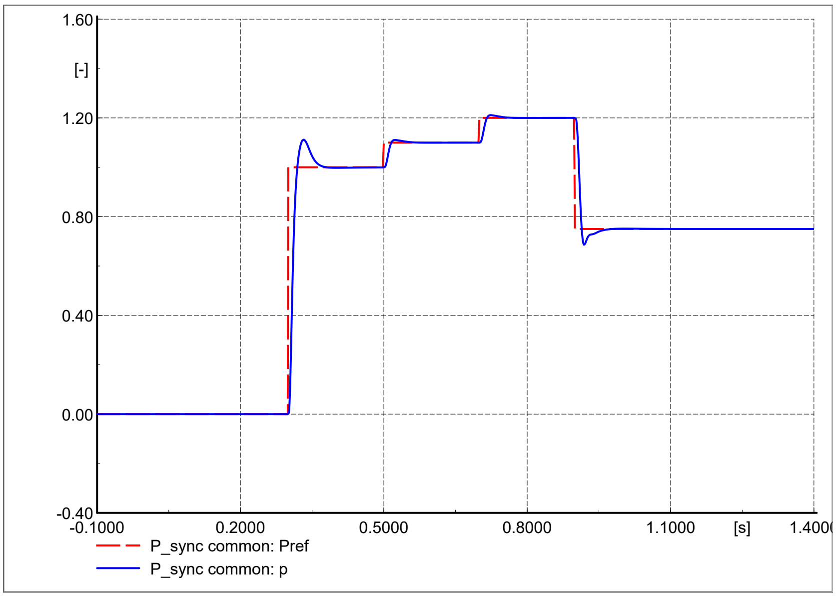


**Figure A.9:** The power characteristics of the controller when the damping circuit is added. Now the output power, $p$ (blue line), follows the reference power, $p$ (red dashed), with less oscillations and less time before reaching steady state. $K_p$ is still set to 62.83 rad/s. At t=0.3 s the switch between the Wind turbine and connection point to it terminal is closed, and $P_{ref}$ is increased from 0 $p.u$ to 1 $p.u$. At t=0.5 s and t=0.7 s $P_{ref}$ is increased to 1.1 $p.u$ and 1.2 $p.u$ respectively, while at t=0.9s it is decreased to 0.75 $p.u$.

The new response in electrical frequency is seen in Figure A.10.

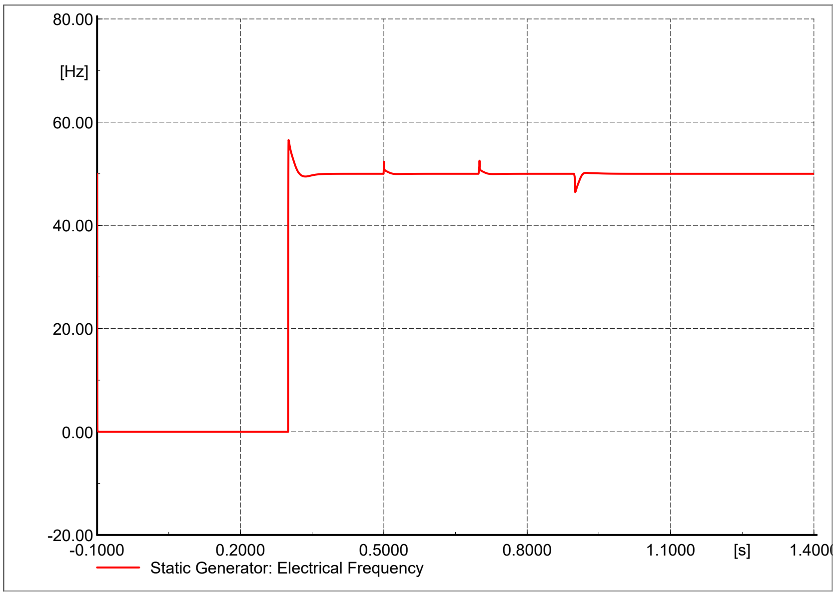


**Figure A.10:** The electrical frequency response in the static generator with the added damping circuit. $P_{ref}$ was stepped with the following magnitudes 1 $p.u$, 1.1 $p.u$, 1.2 $p.u$ and 0.75 $p.u$ at time instances 0.3 s, 0.5 s, 0.7 s and 0.9 s.

### A.1.5 DC-link implementation

The next step in the verification process was to include the DC-link that models the DC-source power, $P_{set}$, and the energy stored in the DC-link capacitance, $C_{DC}$, so its dynamics could be analysed when added into the model. The resulting response of power can be seen in Figure A.11.

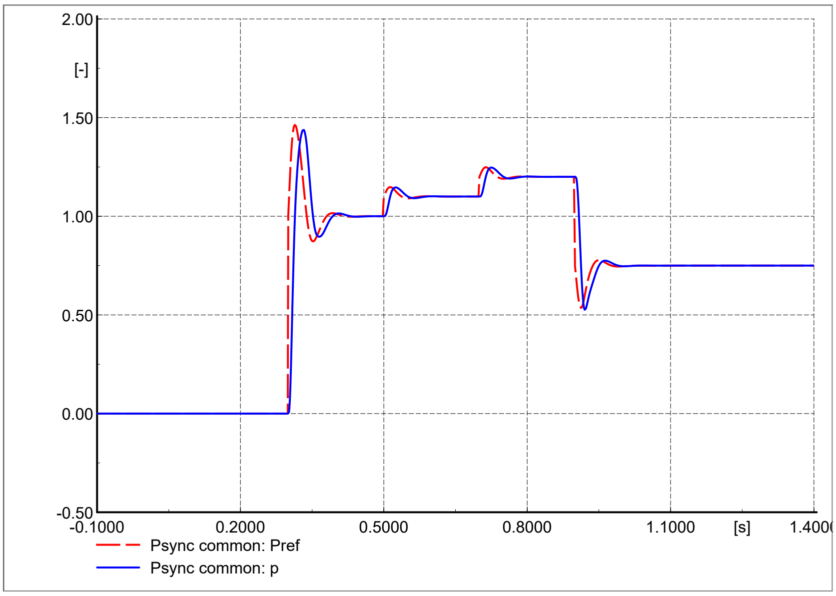


**Figure A.11:** The PS-loop controls the output power, $p$ (blue line), to follow the reference power, $P_{ref}$(red dashed), with a $K_p$ value set to 62.83 rad/s and $R_a$ set to 0.2. At t=0.3 s the switch between the Wind turbine and connection point to it terminal is closed, and $P_{ref}$ is increased from 0 $p.u$ to 1 $p.u.$ At t=0.5 s and t=0.7 s $P_{ref}$ is increased to 1.1 $p.u$ and 1.2 $p.u$ respectively, while at t=0.9s it is decreased to 0.75 $p.u.$

Further, the differences in reference and current DC-link voltage are shown in Figure A.12.

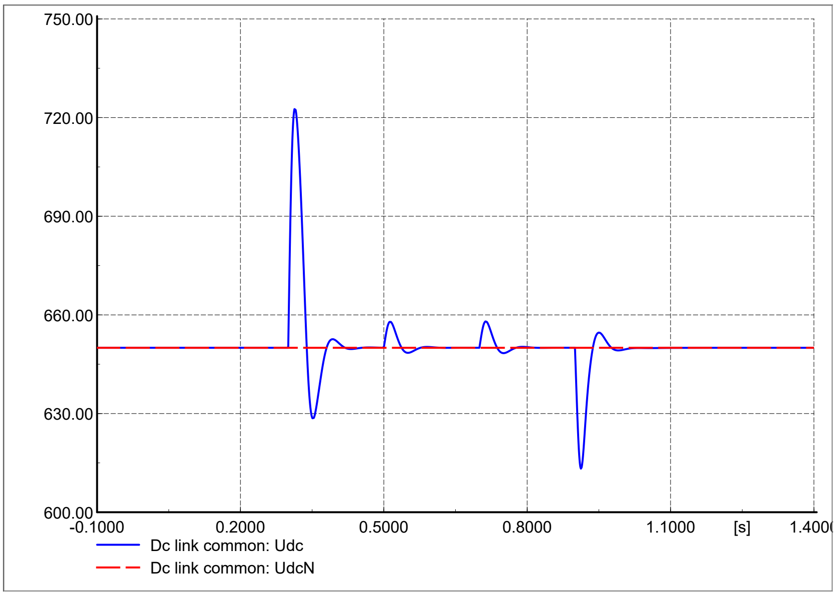


**Figure A.12:** The response in DC-link voltage when the input power $P_{set}$ was stepped with the following magnitudes 1 $p.u$, 1.1 $p.u$, 1.2 $p.u$ and 0.75 $p.u$ at time instances 0.3 s, 0.5 s, 0.7 s and 0.9 s.

Due to initialisation errors the DC-link was stepped from 0 to 1 at 0.3 s (if it would have been done earlier problems in in the DC-link controllers integral block would have occured) shortly after the actual DC-link voltage, $u_{DC}$, increases to the reference voltage, $U_{DCN}$, which is 650 V. Both the voltage and the frequency that is withhold at the terminal of the Wt are seen in figures A.13 and A.14.

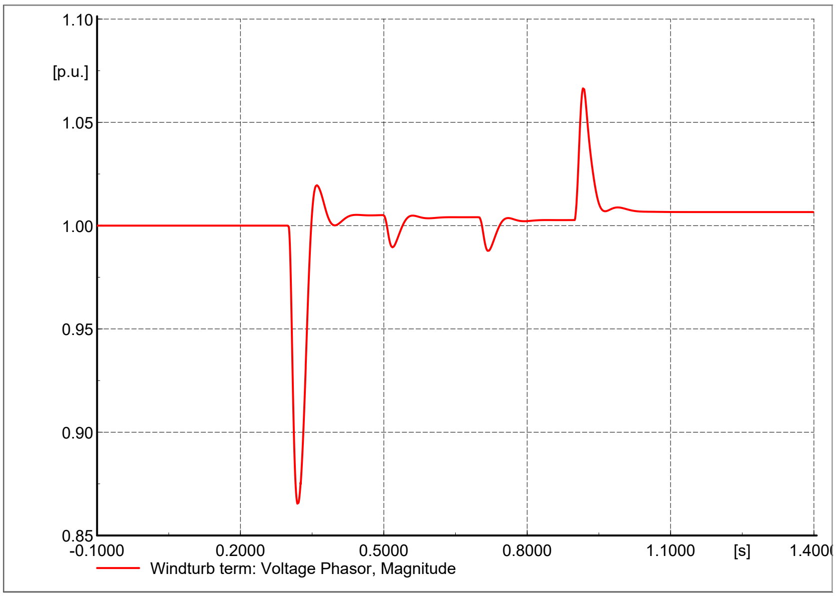


**Figure A.13:** Fluctuations in terminal voltage as a result of steps in input power, $P_{set}$. $P_{set}$ was stepped with the following magnitudes 1 $p.u$, 1.1 $p.u$, 1.2 $p.u$ and 0.75 $p.u$ at time instances 0.3 s, 0.5 s, 0.7 s and 0.9 s.

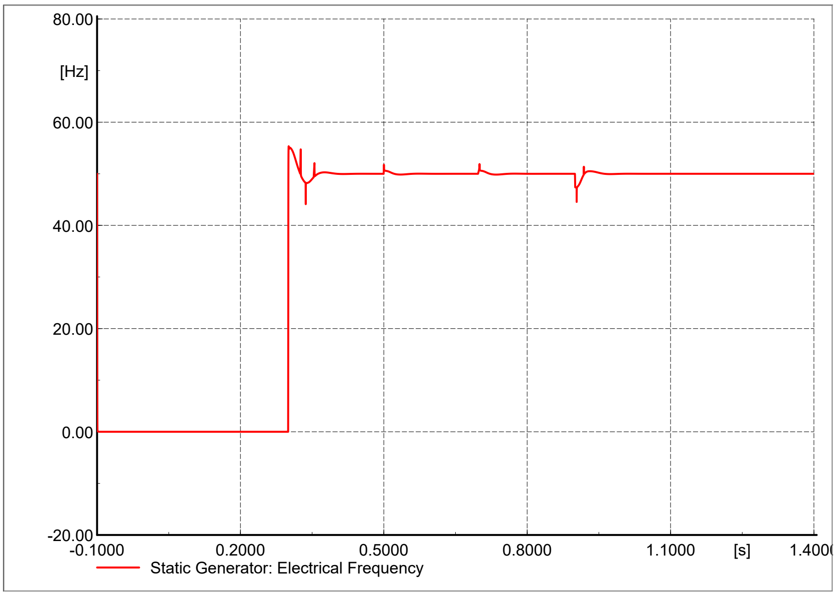


**Figure A.14:** Fluctuations in frequency of the WT as a result of steps in input power, $P_{set}$. $P_{set}$ was stepped with the following magnitudes 1 $p.u$, 1.1 $p.u$, 1.2 $p.u$ and 0.75 $p.u$ at time instances 0.3 s, 0.5 s, 0.7 s and 0.9 s.

### A.1.6 Voltage controller

In the earlier steps, the control of frequency, power output and DC-link energy worked as desired. The last thing that needed verification was the voltage control of the WT since the voltage measured at the WT terminal was not maintained to 1 $p.u.$ Result with the implemented voltage controller can be seen in Figure A.15.

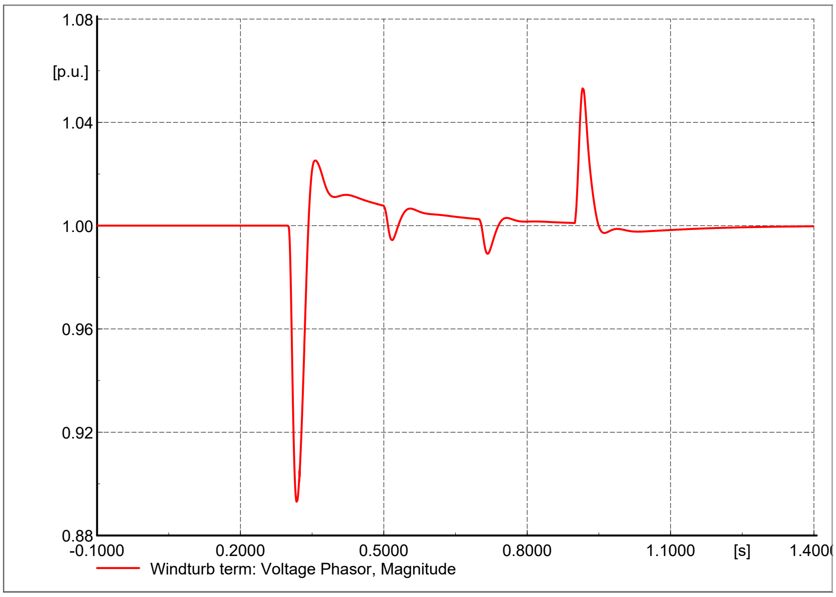


**Figure A.15:** Response on terminal voltage with the addition of a voltage controller when $P_{set}$ was stepped with the following magnitudes 1 $p.u$, 1.1 $p.u$, 1.2 $p.u$ and 0.75 $p.u$ at time instances 0.3 s, 0.5 s, 0.7 s and 0.9 s.

Compared to Figure A.13, it is now seen that the voltage is controlled to 1 $p.u$ with the addition of the voltage controller, which can be seen at 1.4 s.

## A.2 Verification of converter control model in Simulink

### A.2.1 Power synchronisation loop

Test-setup 1 proved to be unstable if the settings were not modified in the verification made in Simulink. Simulations showed that for an SCR of 2, $K_p$ needed to be below 0.13 for a stable response. For $K_p = 0.1$ and SCR =2 the step-response seen in Figure A.16 were obtained which in principle follows the step-response obtained in DIgSILENT PowerFactory.

The frequency measured at the PCC during the simulation of the test-setup 1 can be seen in Figure A.17.

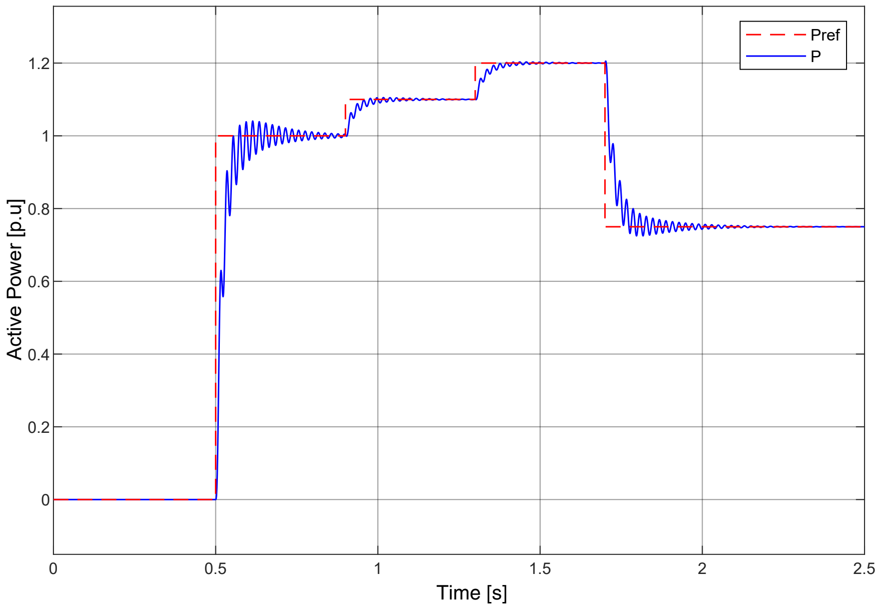


**Figure A.16:** The step-response of the measured power ($P$), when the reference power ($P_{ref}$) were stepped as seen in figure, was obtained using test-setup 1, for $K_p$ = 0.1 and SCR =2

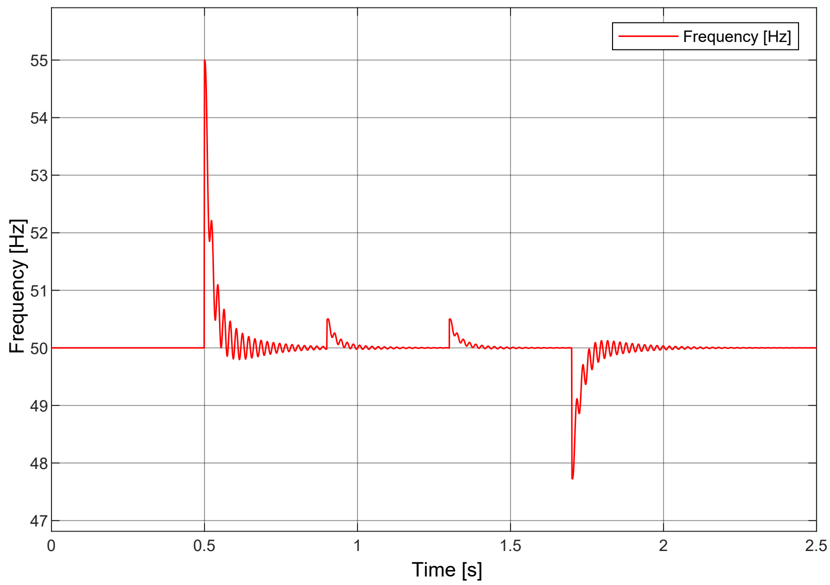


**Figure A.17:** The frequency measured at the PCC, using test-setup 1 for $K_p$ = 0.1 and SCR =2

## A.2.2 Damping circuit

With the inclusion of the active resistance damping circuit the stability of the controller were improved. For an SCR of 3, $K_p/R_a$ could be increased to 0.29 without entering unstable operations. For SCR =3 and $K_p/\ R_a$ = 0.2 the step-response in Figure A.18 were obtained.

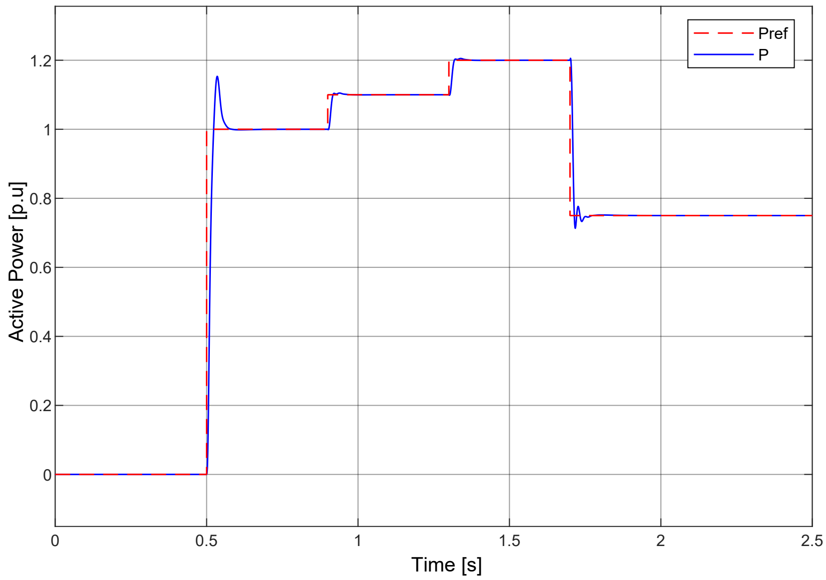


**Figure A.18:** The step-response of the measured power ($P$), when $P_{ref}$ was stepped as seen in figure, was obtained using test-setup 2 for $K_p/R_a = 0.2$ and SCR =3

The frequency measured at the PCC during the simulation of the test-setup 2 can be seen in Figure A.19.

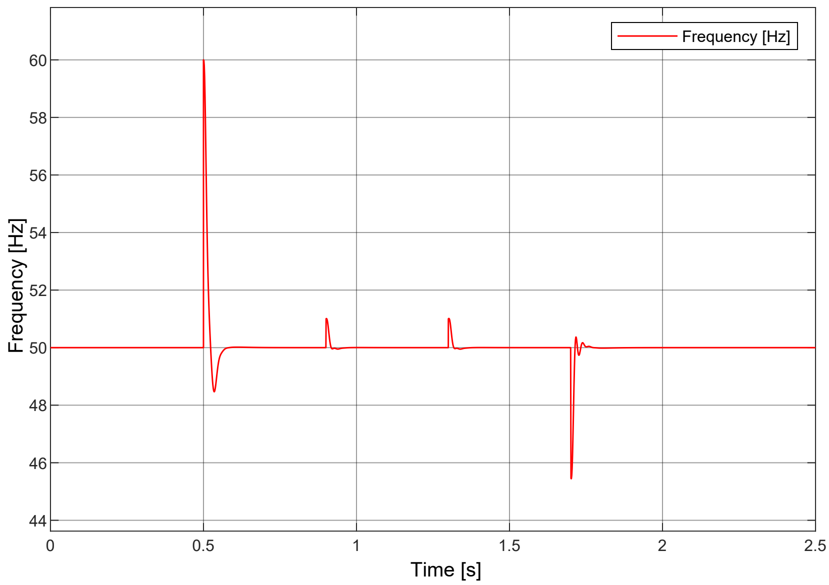


**Figure A.19:** The frequency measured at the PCC, using test-setup 2 for $K_p/R_a = 0.2$ and SCR =3

### A.2.3 DC-link implementation

With the addition of the DC-link dynamics, the controller became more unstable. For a SCR of 3, $K_p/R_a$ had to be set to 0.18 or lower. For SCR =3 and $K_p/\ R_a =$ 0.15 the step-response in Figure A.20 were obtained.

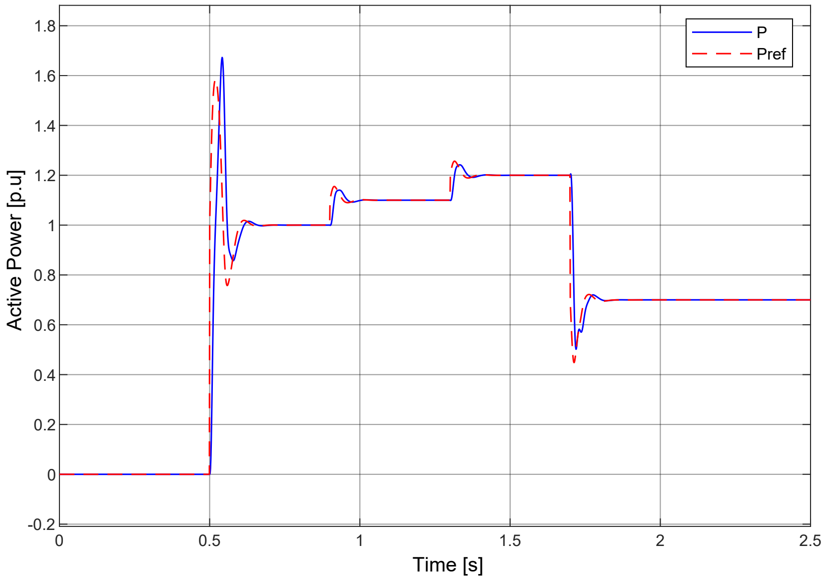


**Figure A.20:** The step-response of the measured power ($P$) and $P_{ref}$, when the power in to the DC-link ($P_{set}$) was stepped from 0 to 1 $p.u$, from 1 to 1.1 $p.u$, from 1.1 to 1.2 $p.u$ and 1.2 to 0.75 $p.u$, was obtained using test-setup 3 for $K_p/R_a = 0.15$ and SCR =3

The frequency measured at the PCC during the simulation of the test-setup 3 can be seen in Figure A.21.

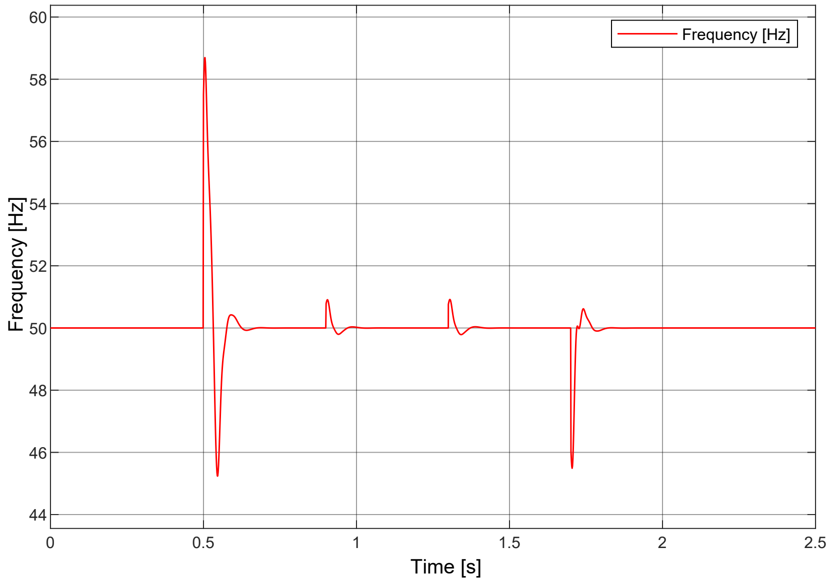


**Figure A.21:** The frequency measured at the PCC, using test-setup 3 for $K_p/R_a$ = 0.15 and SCR =3

The energy in the DC-link (the energy stored in the capacitor) during the simulation of test-setup 3 can be seen in Figure A.22.

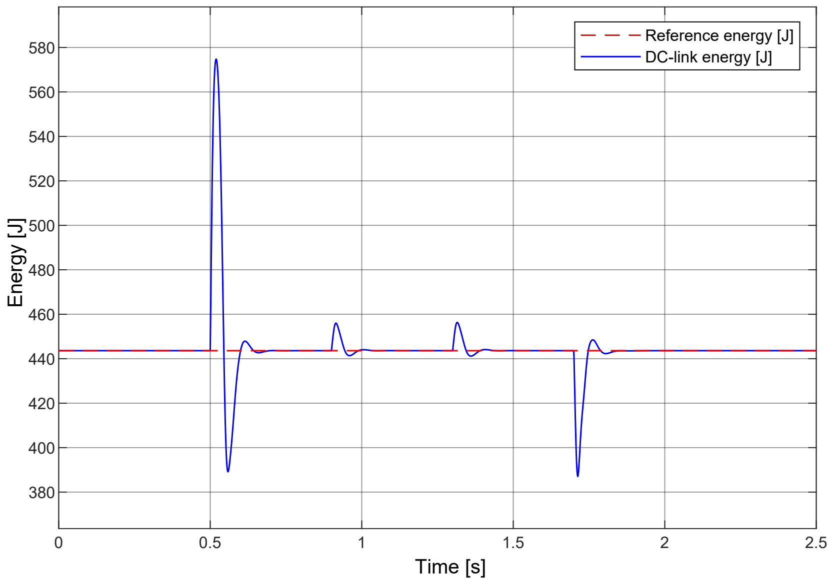


**Figure A.22:** The DC-link energy during the simulation, using test-setup 3 for $K_p/R_a$ = 0.15 and SCR =3

### A.2.4 Voltage controller

In the previous test-setups, no voltage controller were added. This leads to the voltage in the PCC not being equal to 1 $p.u$. Without using the voltage controller, if a step in $P_{set}$ from 0 to 1 $p.u$ were applied at $t = 1s$, using $K_p/R_a$=0.15 and SCR=3 (the same settings as in test-setup 3), the voltage magnitude in $dq$-frame measured at the PCC can be seen in Figure A.23.

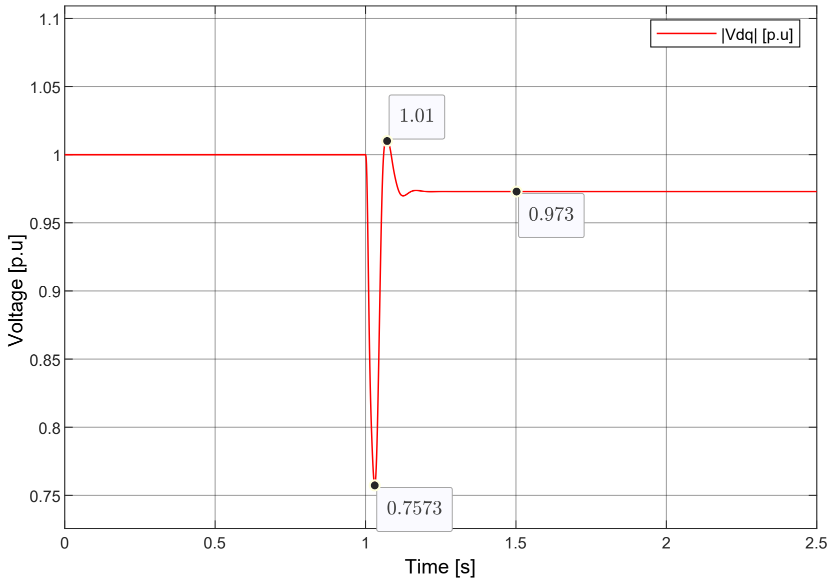


**Figure A.23:** The voltage magnitude in $dq$-frame measured at the PCC. Obtained using test-setup 3 when a step in $P_{set}$ (energy in to the DC-link) from 0 to 1 $p.u$ were applied. $K_p/R_a$=0.15 and SCR=3 were used. The data tips shows the voltage magnitudes measured at the PCC during different times.

Without the voltage controller, the magnitude obtained was 0.973 p.u (as seen in Figure A.23), in this scenario there may not be a need to add a voltage controller. However, as seen in Section 7.2.3 the voltage magnitude can be altered when changing grid-parameters which may lead to the need for a voltage controller. The reactive power measured at the PCC during this setup without the voltage controller can be seen in Figure A.24.

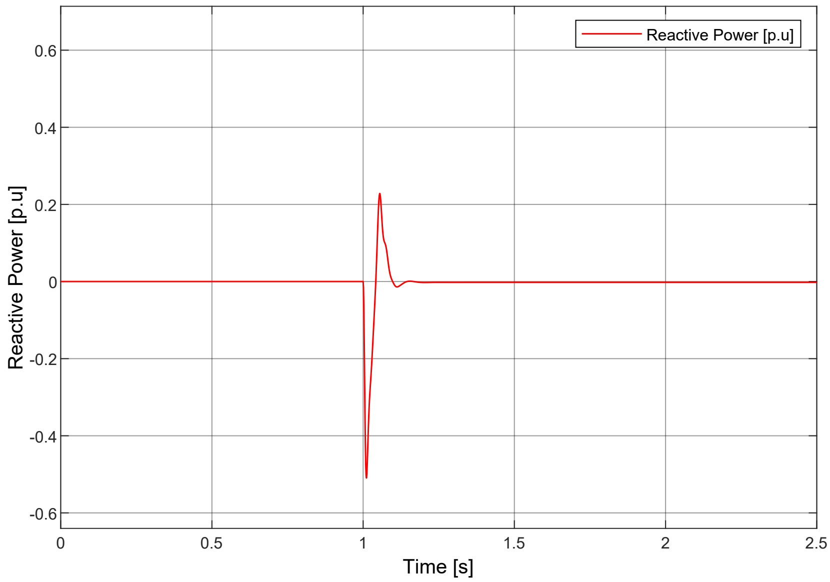


**Figure A.24:** The reactive power measured at the PCC. Obtained using test-setup 3 when a step in $P_{set}$ (energy in to the DC-link) from 0 to 1 $p.u$ were applied. $K_p/R_a$=0.15 and SCR=3 were used.

If the same setup is used with the addition of the voltage controller, with a proportional gain of 0.2 and an integral gain of 10, the voltage magnitude in $dq$-frame measured at the PCC is altered as can be seen in Figure A.25.

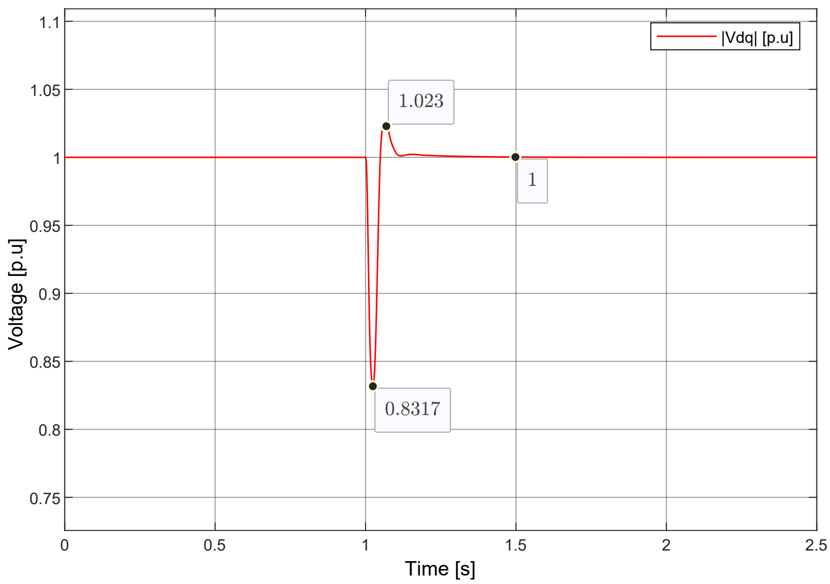


**Figure A.25:** The voltage magnitude in $dq$-frame measured at the PCC. Obtained using test-setup 4 (including the voltage controller) when a step in $P_{set}$ (energy in to the DC-link) from 0 to 1 $p.u$ were applied. $K_p/R_a$=0.15 and SCR=3 were used. The data tips shows the voltage magnitudes measured at the PCC during different times.

Similarly, this change affects the reactive power measured at the PCC as shown in Figure A.26.

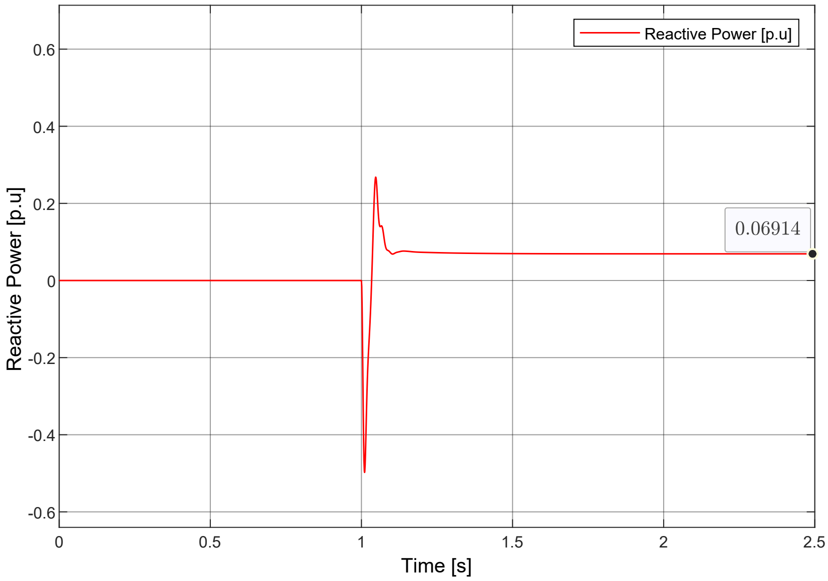


**Figure A.26:** The reactive power measured at the PCC. Obtained using test-setup 4 (including the voltage controller) when a step in $P_{set}$ (energy in to the DC-link) from 0 to 1 were applied. $K_p/R_a$=0.15 and SCR=3 were used. The data tips shows the reactive power measured at the PCC during different times.

## A.3 Discussion of verification

Because of the difference in implementation between the two software the result differs slightly in the testing steps. This can most likely be referred to the difference in grid-strengths, resistive ratio and the fact that in DIgSILENT PowerFactory we have been using a predefined power measurement device which could interfere by filter some transients. However, the results show the same principal behaviour, and we are confident that the results are reliable.

### A.3.1 Test-setup 1: Power synchronisation loop

As assumed based on the theory the control system is not as stable without the addition of the damping circuit. This can be seen in both DIgSILENT PowerFactory where a lot of oscillations occur in the output power and the frequency, but most of all in Simulink where the proportional gain had to be decreased to obtain stable operations (with similar amounts of oscillations). In both software, the grid impedances had to be altered for stable output. This further proves that it is not recommended to implement this controller without the damping circuit.

### A.3.2 Test-setup 2: Damping circuit

The damping circuit modifies the output voltage to decrease the oscillations which have been seen in both software. The obtained step-response for the active power consists of a small overshoot and the oscillations have been successfully removed (both for the power and the frequency) with this addition. It has been proven to be much more stable since the proportional gain could be increased further in Simulink. This controller could be a viable option for implementation since it has successfully been further tested in Simulink. This setup is, however, assuming that there is unlimited energy in the DC-link, or at least enough energy available since the input is always the reference power. This could be true if the machine side converter has enough headroom or if energy storage is used.

### A.3.3 Test-setup 3: DC-link implementation

By adding the DC-link the reference power is not assumed to be constant but rather depending on the DC-link. This is seen in both software since for a change in $P_{set}$ (change of power from the MSC, representing changes in the wind) the reference power $P_{ref}$ is changing depending on the energy available in the DC-link capacitor. This implementation is affecting the stability (as concluded by the larger overshoot and having to decrease $K_p/R_a$ to obtain stable response) of the system which can most likely be referred to that the step in $P_{set}$ is instant, however, the step in $P_{ref}$ and consequently output power is not, leading to the integration block in the DC-link controller to integrate an error which, if too large will create instability. In reality, this might not be as much of a problem since the power from the machine side is not changing as instant but rather in a more low-pass filtered way. It could be interesting to add this behaviour as well to see how this setup would respond. As it is presented in this thesis it is assumed that the MSC is a constant power source, which assumes that either headroom in MSC exists or energy storage is used which is why it is added in this way.

### A.3.4 Test-setup 4: Voltage controller

In the previous test-setups, the steady-state voltage-output at the PCC has not been at the nominal value. In DIgSILENT PowerFactory it has been slightly above 1 $p.u$ and in Simulink slightly below. The difference can be referred to the resistive ratio being higher in DIgSILENT PowerFactory which has been proved to increase the terminal steady-state voltage. The addition of the voltage controller has proven to work together with the PSC and for the presented values of the PI-controller, a stable response was obtained that controlled the terminal voltage to 1 $p.u.$ During the testing in DIgSILENT PowerFactory, it has been proven to work for several active power steps, although acting too slow before the next step in power, and in the testing conducted in Simulink, it is shown that the increase of voltage is done by the increase of reactive power. This is as expected since reactive power is tightly connected to the voltage magnitude.

# B

# Appendix B - DIgSILENT PowerFactory model Testing and verification

In this section an overview of the model (Test-setup 4) used in DIgSILENT PowerFactory are presented.

## B.1 The composite models

The composite model used is shown in Figure D.1.

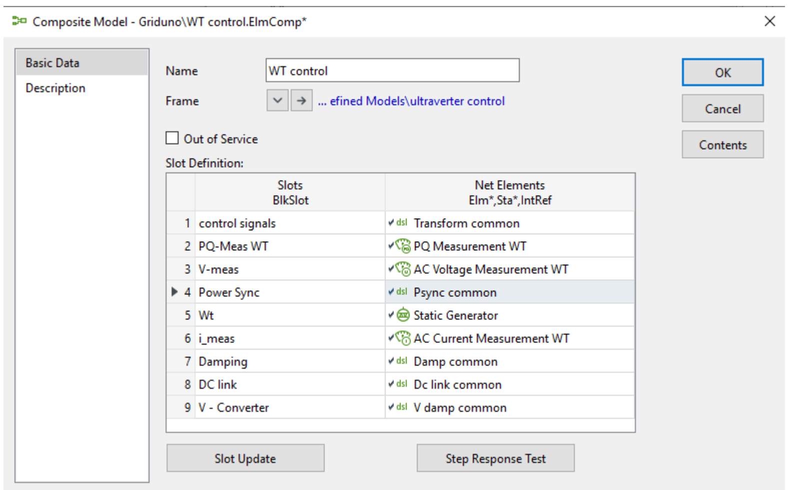


**Figure B.1:** The composite model used during simulation for testing and verification.

As seen the composite model contains five common models, in the following list a short explanation of what each common model does is seen;

- Transform common - this model transforms the voltages in the $dq$-frame to $\alpha\beta$-frame.
- Psync common - the power synchronisation loop of the controller
- Damp common - damping circuit that uses the converter output current and a high pass filter to subtract a term with gain, $R_a$, to dampen the converter voltage and avoid oscillations.
- Dc link common - represents the DC-link and its capacitor that exchanges energy with the grid.
- V damp common - voltage controller to maintain a certain voltage level.

The other slots are measurements.

## B.2 The composite frame and composite block definition

In the following section the composite frame and all composite block definitions are presented.

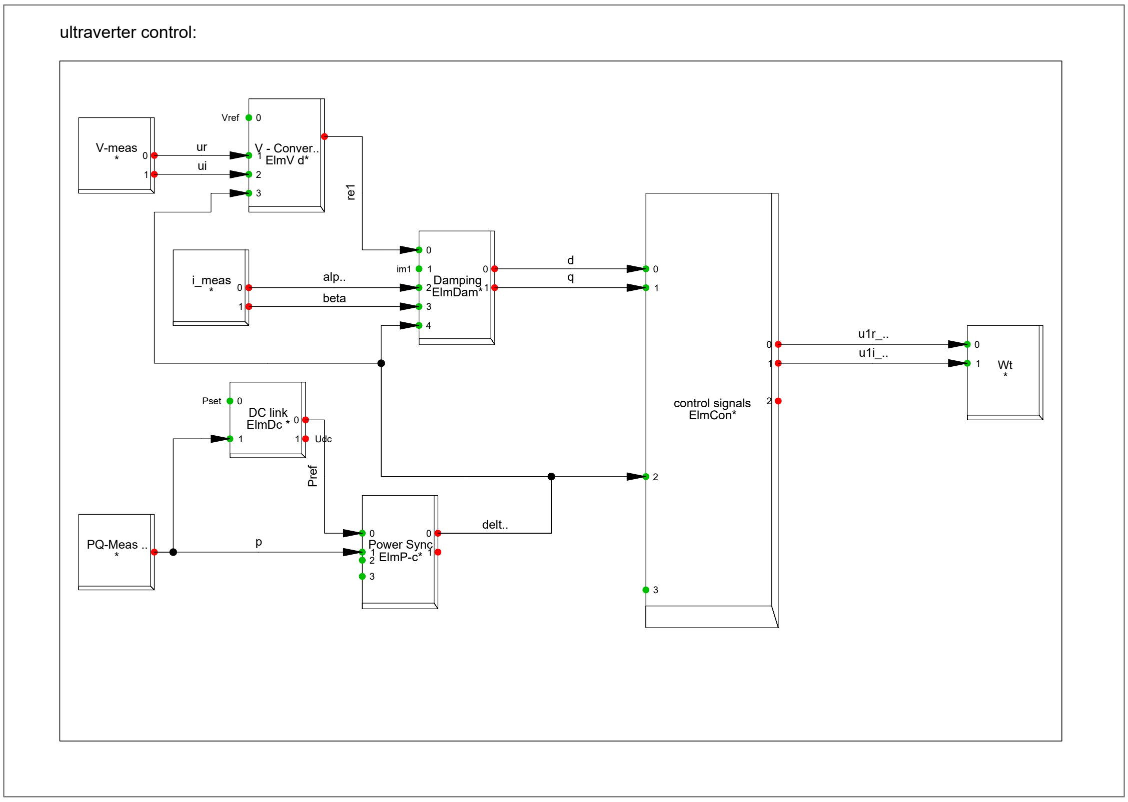


**Figure B.2:** The complete composite frame containing all common models.

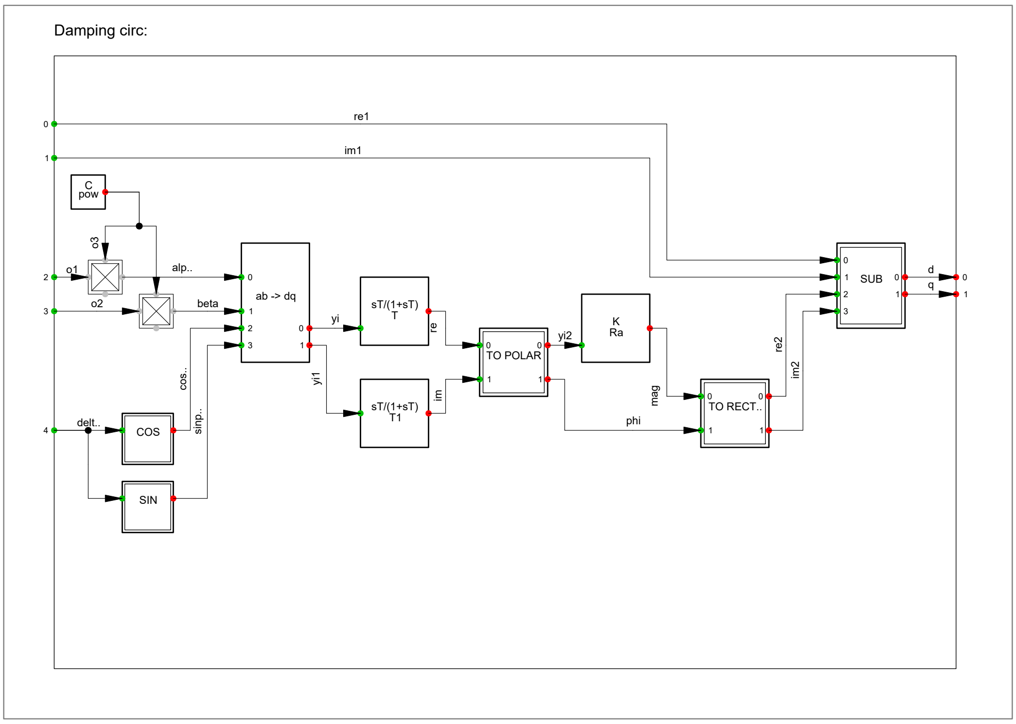


**Figure B.3:** The damping circuit to dampen oscillations in converter voltage. The block named "C pow" was a constant used to get power-invariant scaling instead for magnitude-invariant. $R_a$ is the reactive resistance.

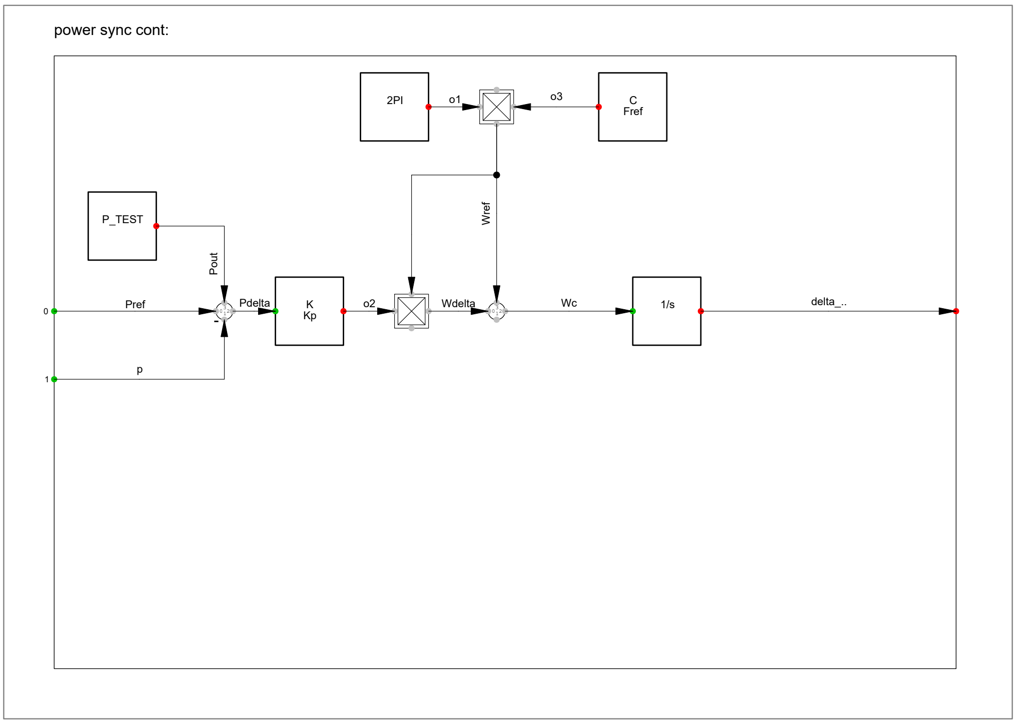


**Figure B.4:** The power synchronisation block definition with the gain $K_p$ shown. $P_{test}$ was used for debugging but not used in the final simulation.

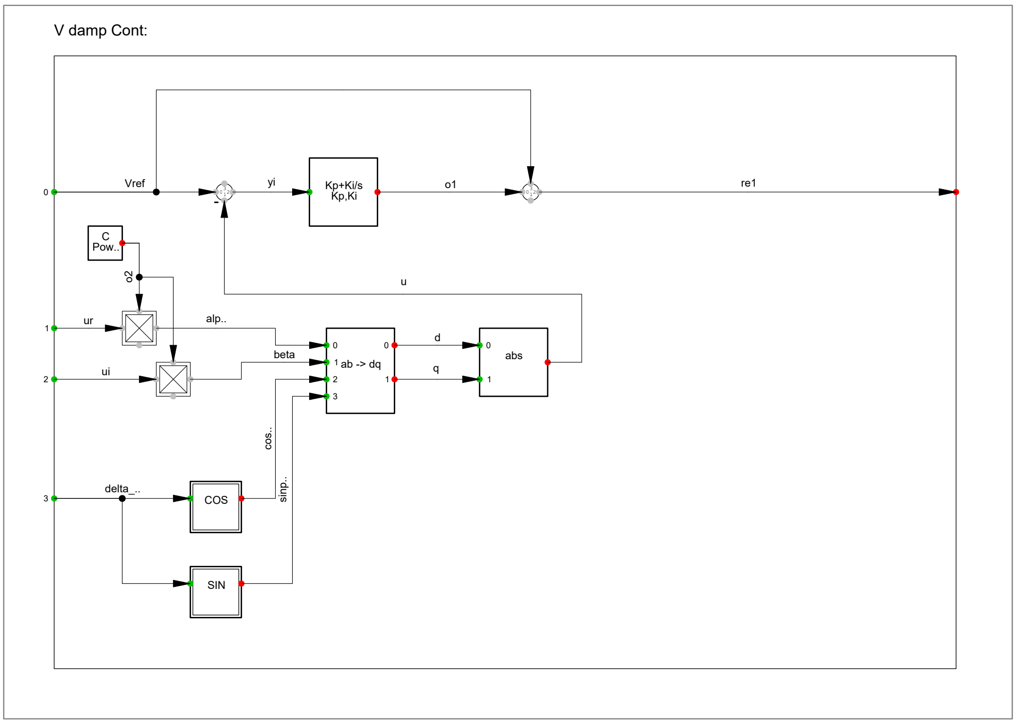


**Figure B.5:** The voltage controll block. To obtain power-invariant scaling the constant "C pow" was used.

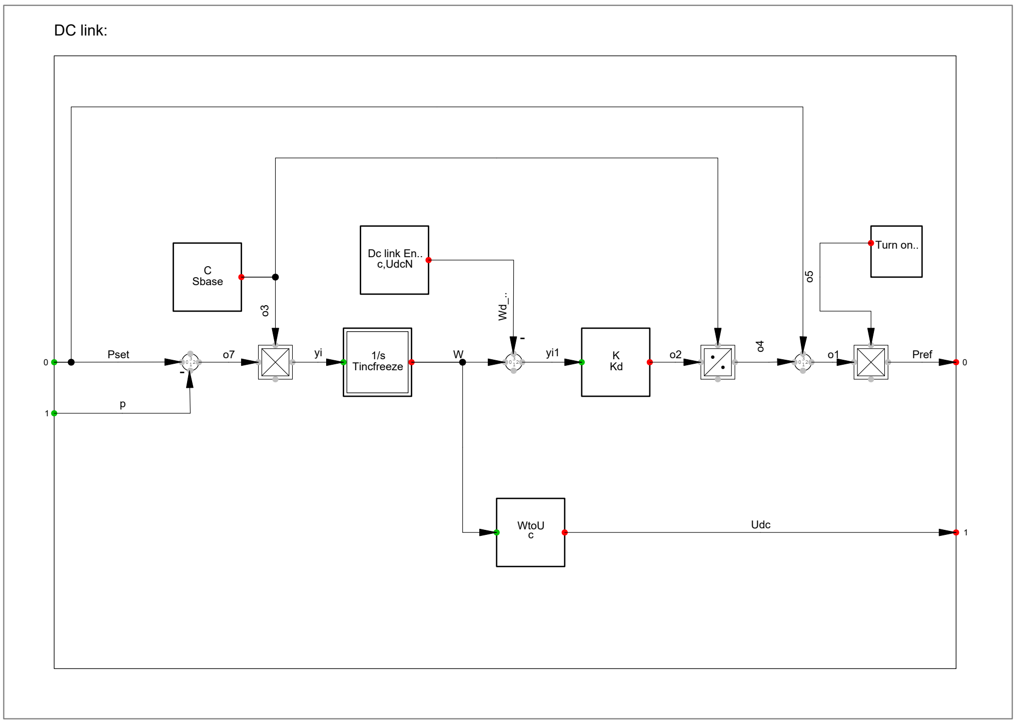


**Figure B.6:** The DC-link block definition. The block name "turn on" was set to 1 during the whole simulation. The reason why it was included was for debugging purposes.

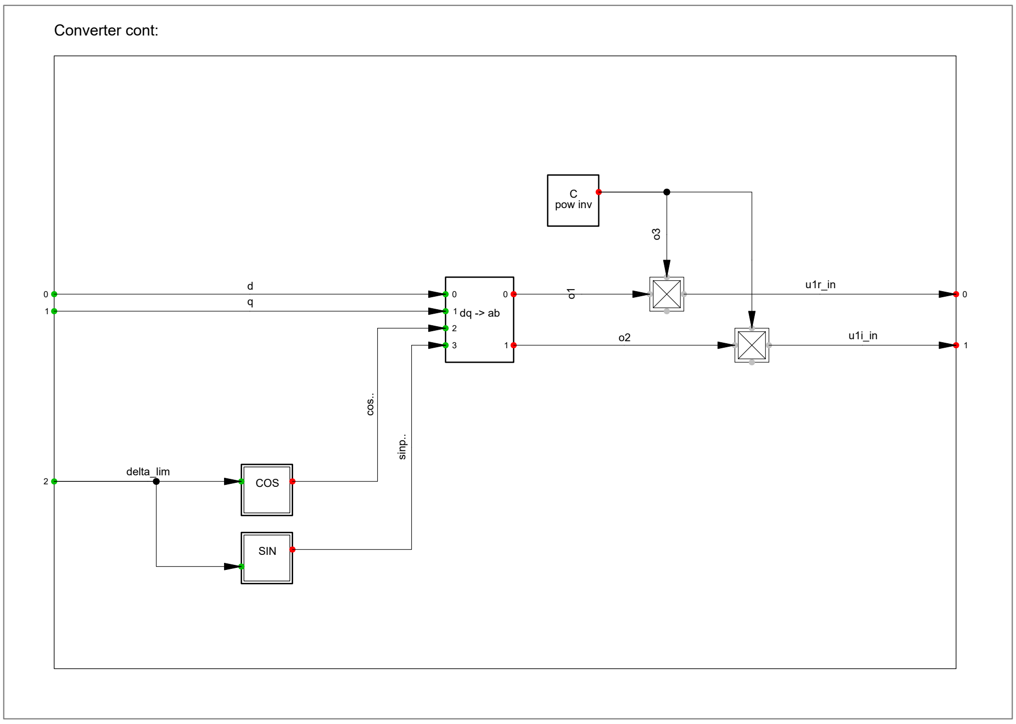


**Figure B.7:** This block is the one that converts voltage represented in the $dq$-frame to $\alpha\beta$-frame, that is sent in to the genstat.

# C

# Appendix C - DIgSILENT PowerFactory model, Black start

In this Chapter the model used when simulating black start is presented. Much of the model is similar to what is shown in Appendix B, so only the differences are mentioned in this Chapter.

## C.1 Composite models

The composite model used is shown in Figure D.1.

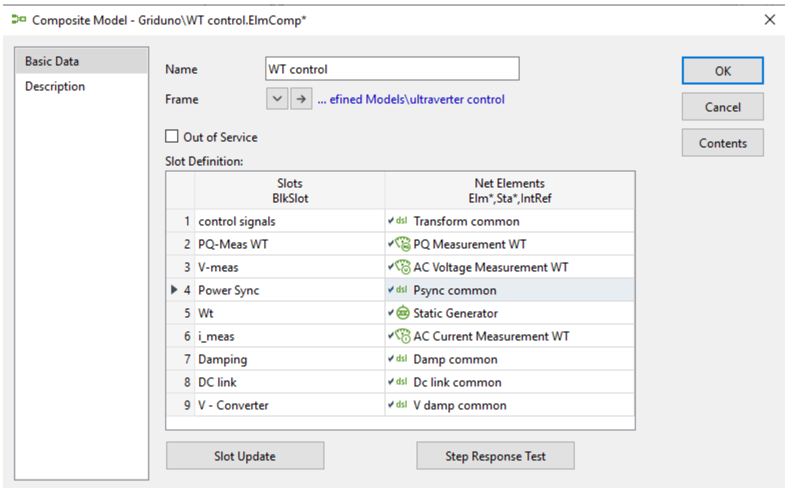


**Figure C.1:** The composite model used during simulation for testing and verification.

## C.2 The composite frame and composite block definition

In the following section the composite frame and all composite block definitions are presented.

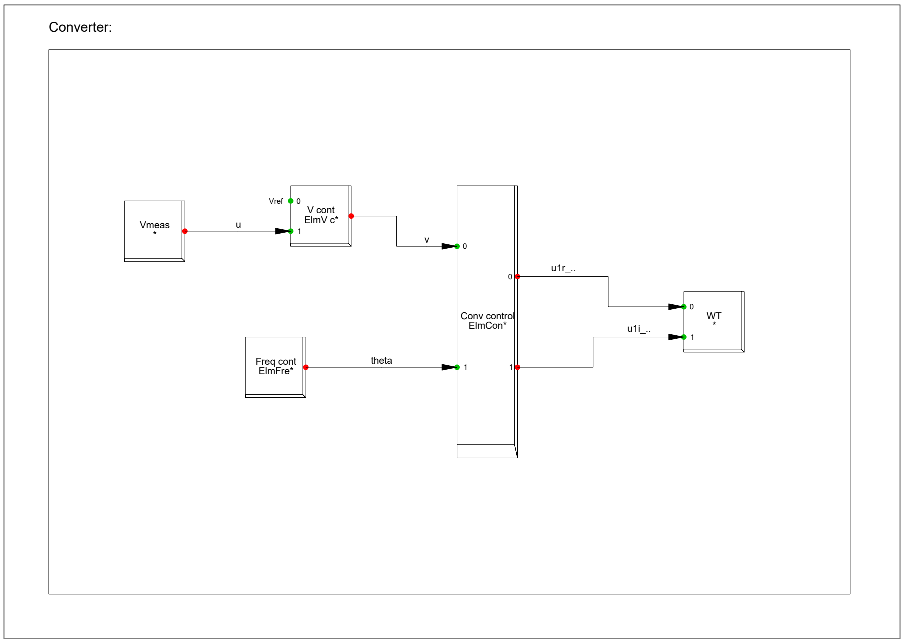


**Figure C.2:** The complete composite frame containing all common models.

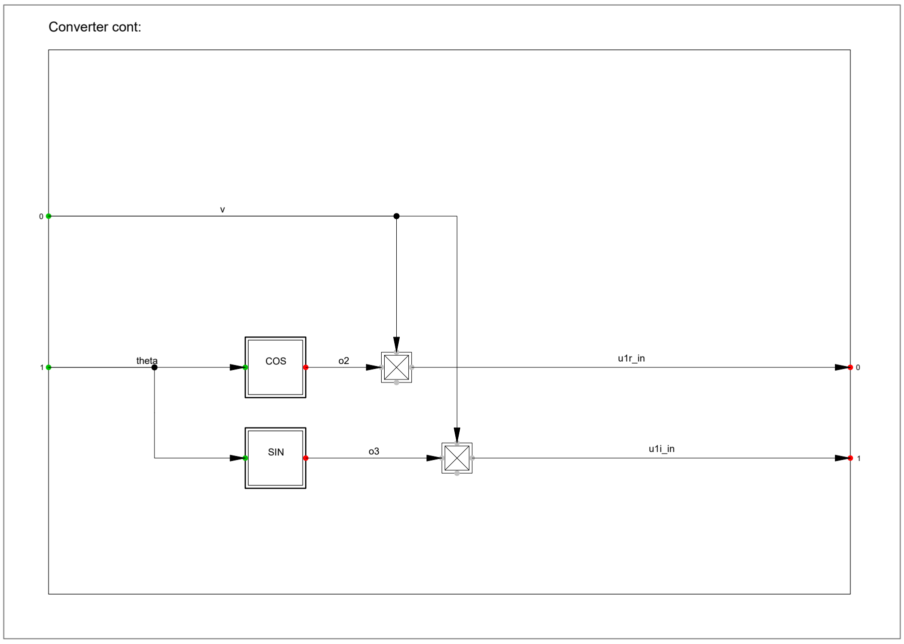


**Figure C.3:** The control block for transforming voltages from $dq$-frame to $\alpha\beta$-frame.

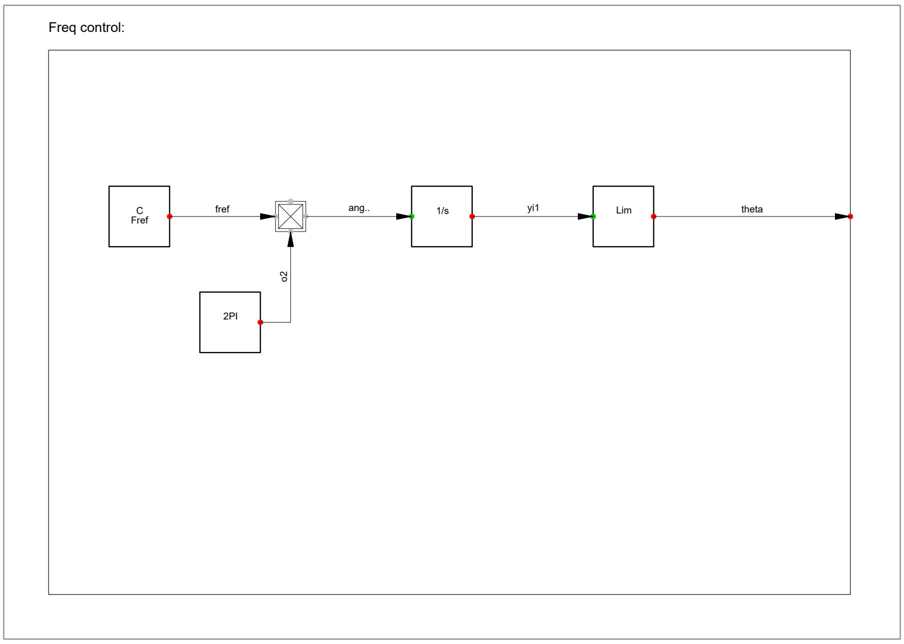


**Figure C.4:** The frequency control block definition. Where the reference of frequency $(fref)$ is set to 50 Hz.

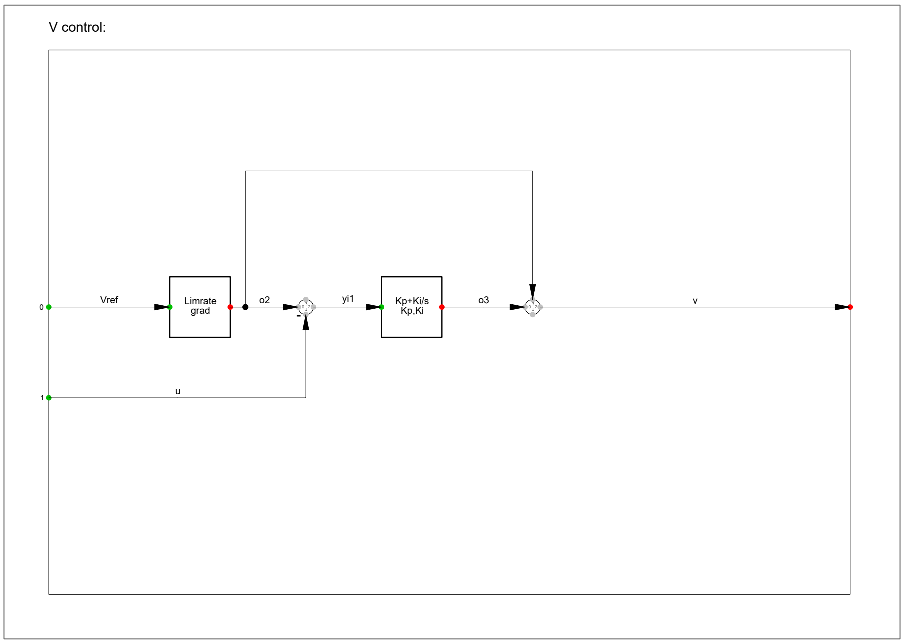


**Figure C.5:** The voltage control block definition. Where the voltage reference $(Vref)$ is set to 1 p.u.

# D

# Appendix C - DIgSILENT PowerFactory model, Off-grid operation

In this Chapter the model used when simulating off-grid operation is presented. Much of the model is similar to what is shown in Appendix B, so only the differences are mentioned in this Chapter.

## D.1 Composite models

The composite model used is shown in Figure D.1.

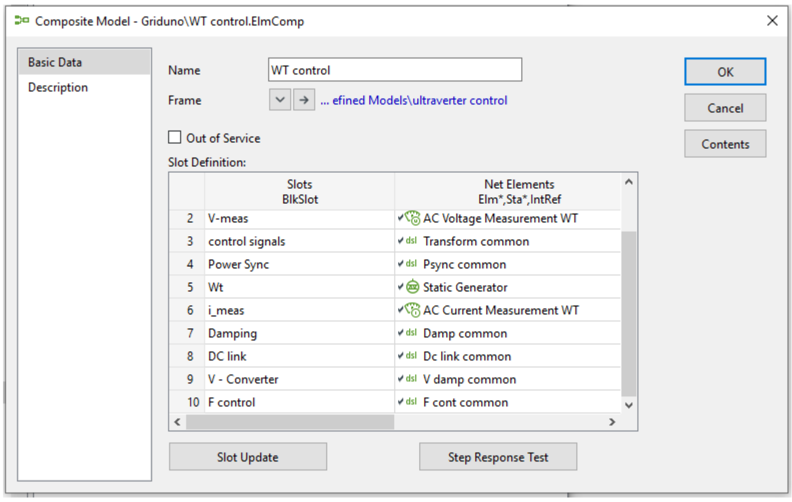


**Figure D.1:** The composite model used during simulation for off-grid operation.

## D.2 The composite frame and composite block definition

In the following section the composite frame and all composite block definitions are presented.

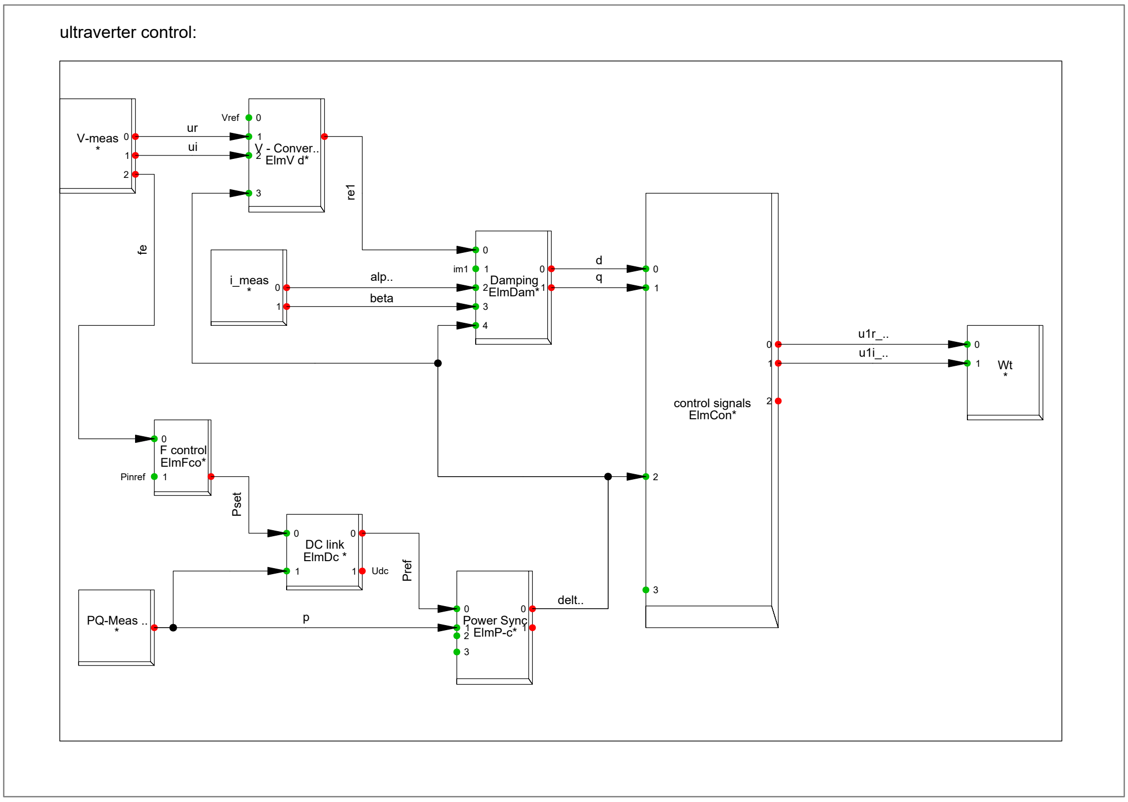


**Figure D.2:** The complete composite frame containing all common models.

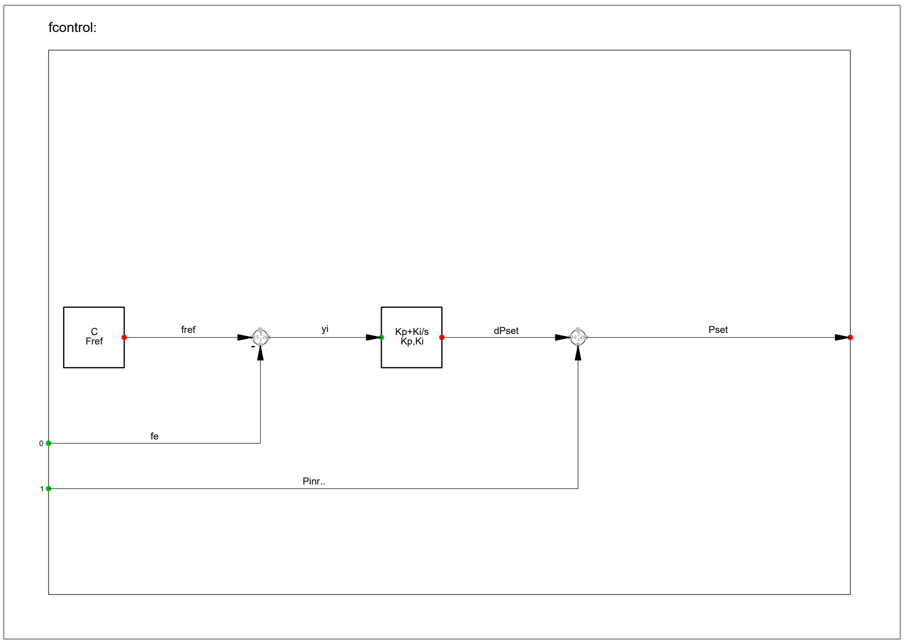


**Figure D.3:** The control block for frequency control that adjust according to load demand. Can be seen as a hugely simplified pitching control.

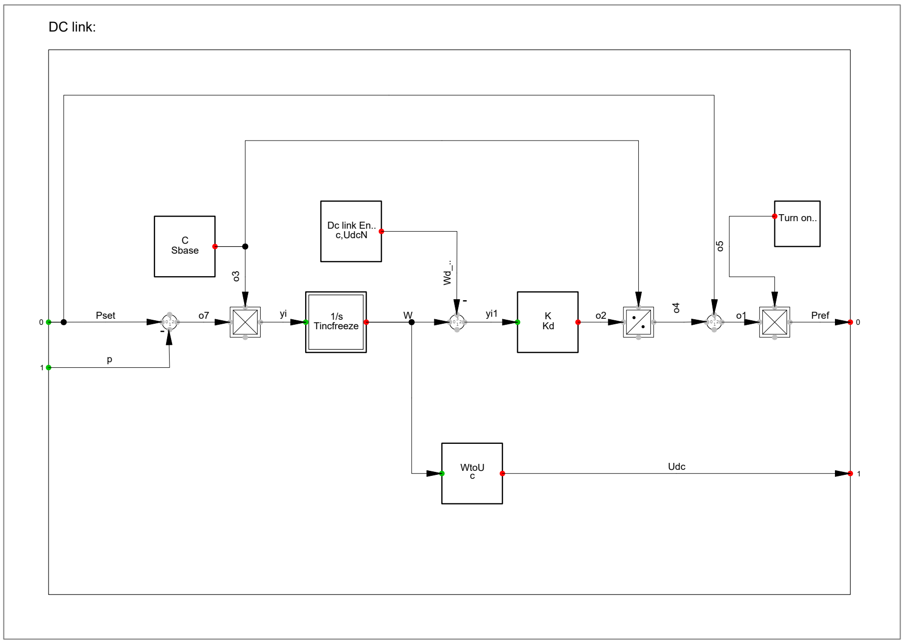


**Figure D.4:** The control block for the DC-link.

# E

# Appendix E - Simulink model

## E.1 Matlab code

```
%%
 clear all
 clc
SCR = 3; %can be change
%base values
f_nom= 50; %Hz
w_nom= 2*pi*f_nom; %rad/s
 V_rated= 400; % Volts
 V_phasepeak = V_rated*sqrt(2/3); %volts
 V_base= V_rated/(sqrt(3)*1000); %in kV
 S_base = 12.7/1000; % in MVA
S_base_SCR = SCR*S_base; % in MVA
Z_base= (3*V_base^2)/S_base; %in ohms
Z_base_SCR = (3*V_base^2)/S_base_SCR; %in ohms
 I_base=V_base/Z_base; %in kiloamps not used


Ra=0.15; % active resistance , can be changed
Kp=Ra ; % proportional gain

%high pass filter in damping circuit
 alpha_hpf=0.1*w_nom; %0.1-0.2

%filter impedance
 Lf=0.15*Z_base/w_nom; %in H
 Rf=w_nom*0.1*Lf; %in ohms

%grid impedence
Lg=1*Z_base_SCR/w_nom; %in H
x=0.1; %change for different resistive ratios
Rg=w_nom*x*Lg; %in ohms
%calculate real SCR used for resistive ratio change
```

```
SCR=(3*V_base^2)/(S_base*sqrt((Lg*w_nom)^2+Rg^2));

%Dc-link
C_dc = 2.1e-3; % in F
Pd= 1;% p.u
Cby2=0.5*C_dc;
Kd=0.18*w_nom;
E_dc_ref = 0.5*C_dc*650*650; % 0.5*((1/(wN*C_dc))/Zbase)*4;
Kp_dc = 0.18*w_nom;


%PLL Theta measurement
freq_PLL = 5; % in Hz
band_PLL = 2*pi*freq_PLL; % in rad/s
Kp_PLL = (2*band_PLL)/V_rated;
Ki_PLL = band_PLL^2/V_rated;

%voltage controller
Kp_vc=0.2;
Ki_vc=10;

%droop replaces the PI-controller during additional testing
slope=0.05;% 5 percent=0.05
Kr=1/slope;
Tr=0.4;


%VSM part used during additional testing
D= 39.48;
H=0.1; %If dc link change Kp/Ra =0.15
%H=2; % If no DC-link Kp/Ra=0.2
```

## E.2 Control-blocks

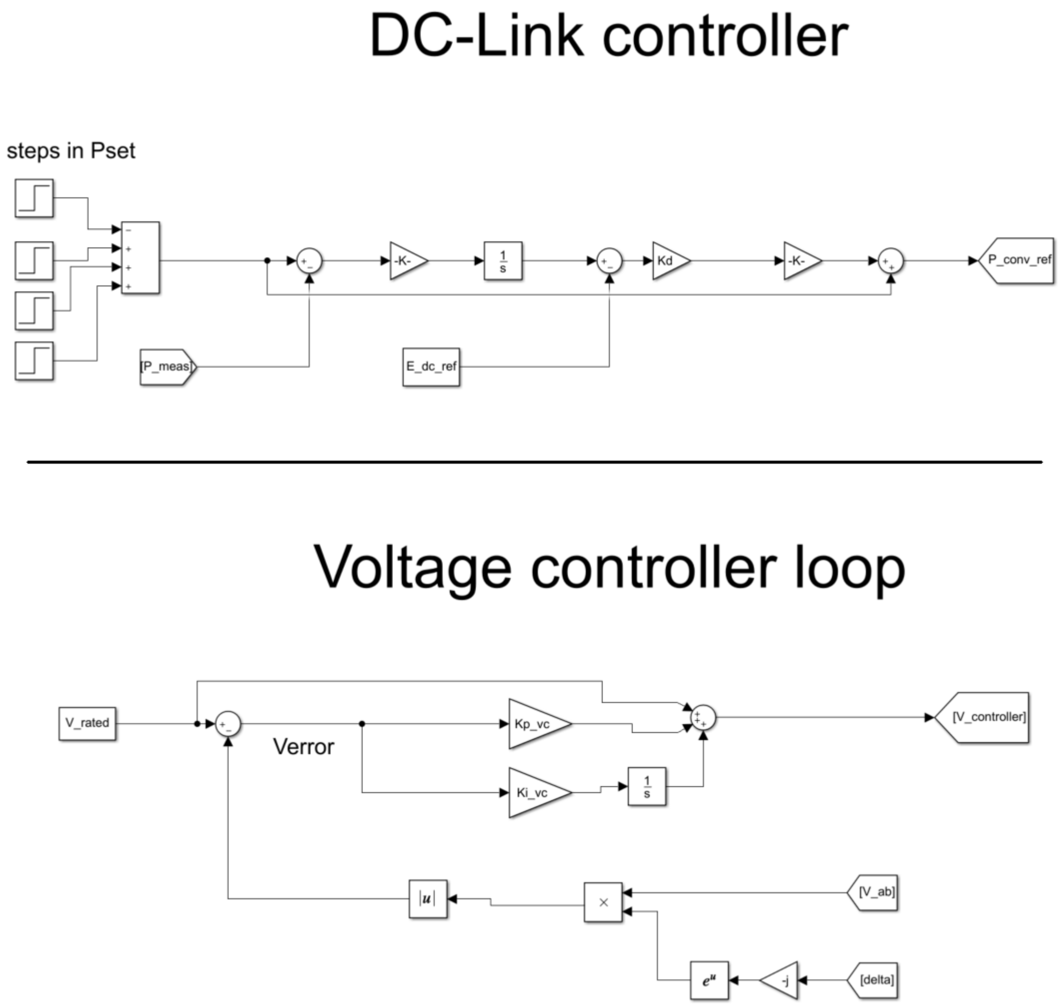


**Figure E.1:** DC-link and voltage controller, the outputs are sent to power synchronisation block. Delta is calculated in the power synchronisation block, V_ab is calculated in Clarke transformation part, Pmeas can be seen in power calculation part.

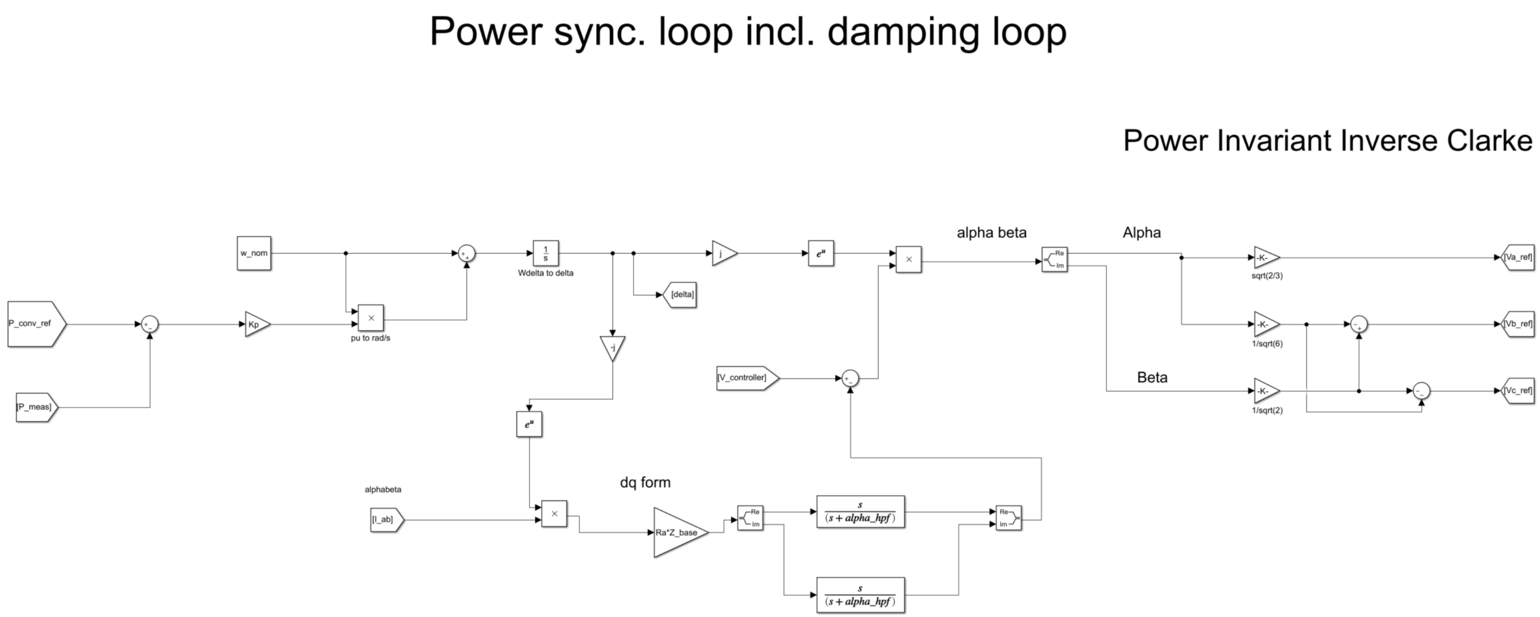


**Figure E.2:** Power synchronisation loop with damping circuit, The voltage signal output are sent to the controllable AC-sources in the grid setup

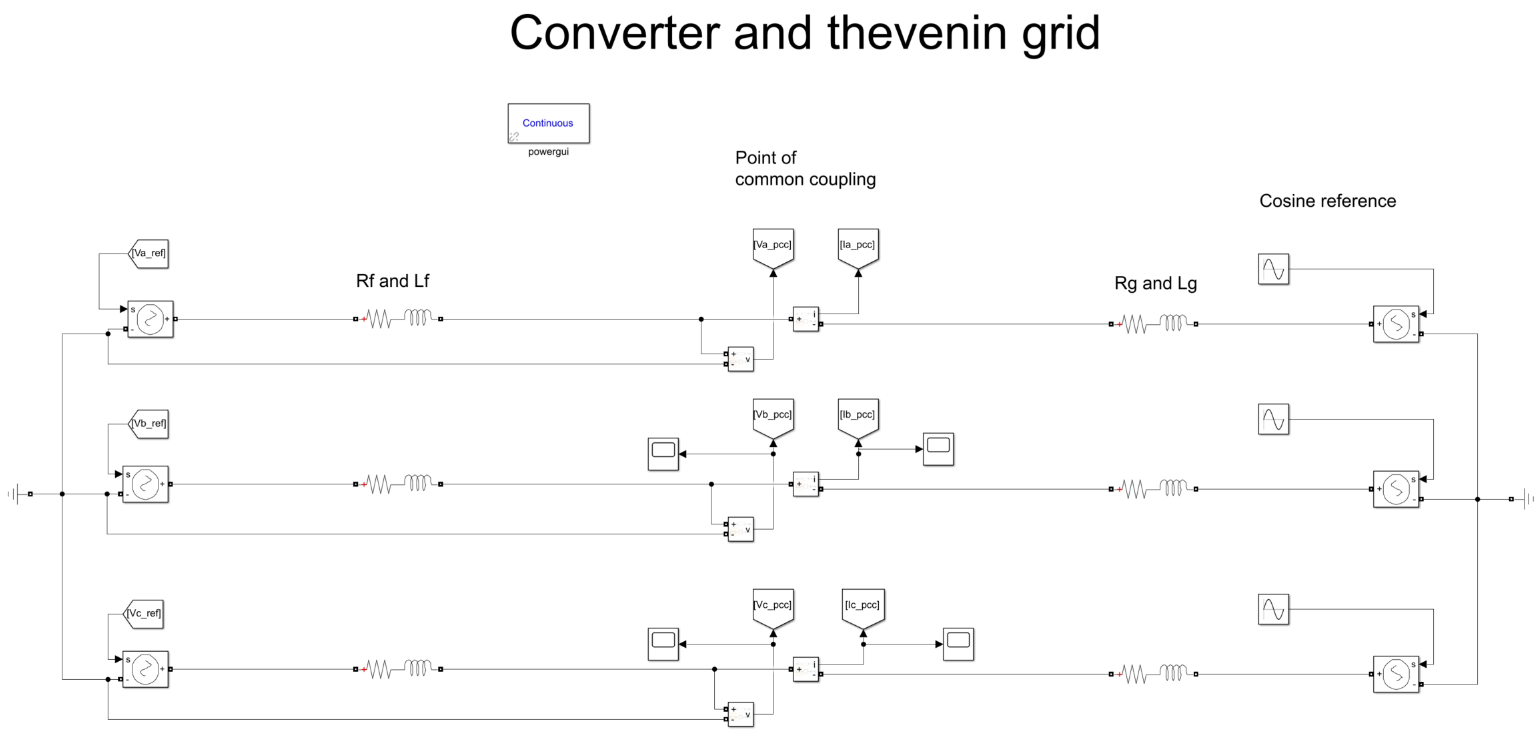


**Figure E.3:** Test-grid setup, Va_ref, Vb_ref and Vc_ref is calculated in the power synchronisation part, the measurements at the point of common coupling are sent to the transformation part.

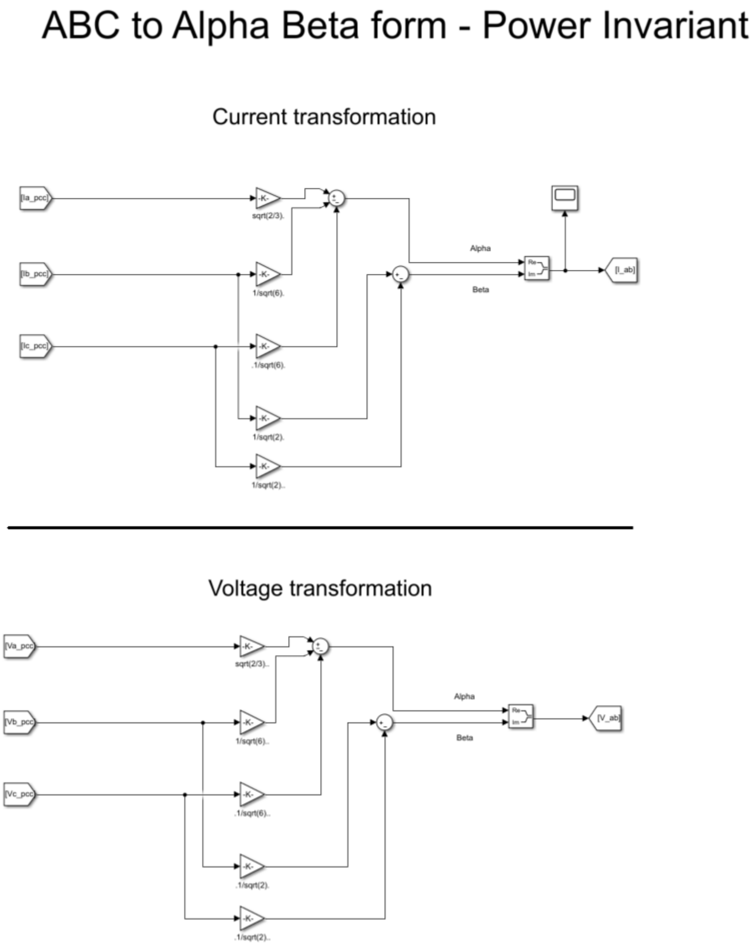


**Figure E.4:** Clarke transformation of measured signals at the point of common coupling.

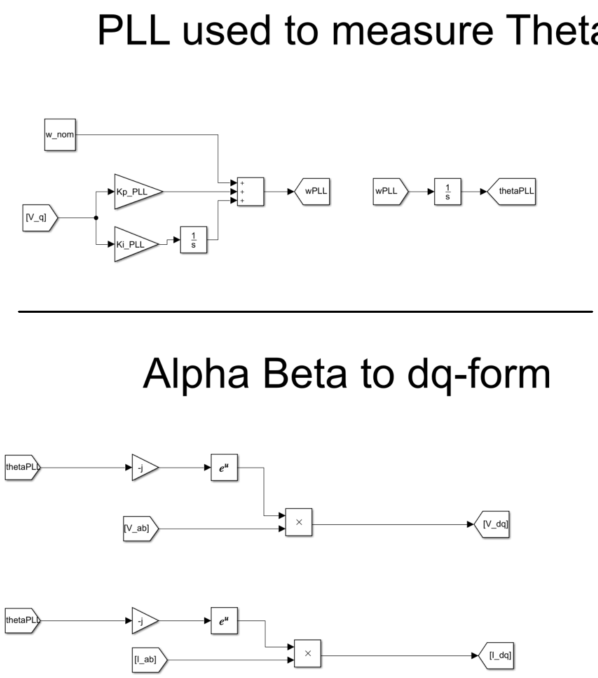


**Figure E.5:** Park transformation of measured signals at the point of common coupling, the inputs comes from the Clarke transformations, Theta comes from the phase estimator (PLL) shown in figure.

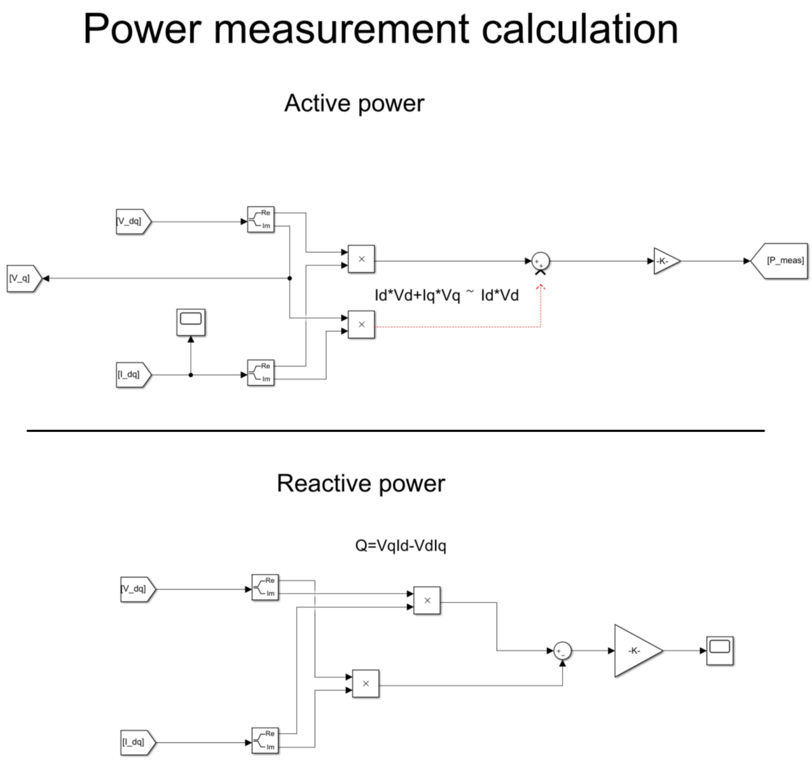


**Figure E.6:** Active and reactive power calculation, The inputs comes from the Park transformation and the output P_meas is sent to the power synchronisation part.

**CHALMERS UNIVERSITY OF TECHNOLOGY**
Gothenburg, Sweden
**www.chalmers.se**